Elastodynamics and Control of Fast Pick-and-place Robots

Zuyu Yin

Department of Mechanical Engineering
McGill University
Montreal, Canada

July 2019

A thesis submitted to McGill University in partial fulfillment of the requirements for the degree of master of engineering.

© 2019 Zuyu Yin

2019/07/04

Abstract

Fast pick-and-place robots are widely used in industry, e.g., in food-packaging and microelectronics. A parallel architecture, composed of one moving platform and one base platform, connected by two serial limbs, was designed and prototyped at McGill University's Centre for Intelligent Machines. The prototype is dubbed the Peppermill Carrier (PMC). The objective of the work reported in this thesis is to improve the speed of this parallel-kinematics machine (PKM), intended for high-speed operations, while considering its elastodynamics, via modelling, and control. The generalized spring, supported with the finite element method, are used to obtain the elastodynamics model of the robot. The natural frequencies of the robot are obtained along a test trajectory, the Adept test cycle, which serves to identify the poor-stiffness postures; the natural frequencies are further applied to build an enhanced mathematical model of the robot. Along the way, stiffness indices are defined, to help both the designer and the control engineer meet performance requirements. The mathematical model of the robot, which takes into account the flexible nature of the limbs, is formulated. Moreover, a gain-scheduling linear quadratic regulator combined with an extended Kalman filter is designed and applied to control fast pick-and-place operations. Based on the gain-scheduling controller, a constant-gain linear quadratic regulator, combined with a constant-gain extended Kalman filter, is found to be effective at controlling the robot during fast operations, while tracking a prescribed, representative trajectory. Inspired by the simulation results obtained by this regulator, a feed-forward proportional-derivative (PD) controller based on the sliding-mode scheme is also proposed. The use of these linear controllers helps decrease the computational complexity. The feasibility of a linear controller for a nonlinear system such as the PMC is also discussed. Finally, a comparison between four control schemes is conducted to analyze their pros and cons.

Abrégé

Les robots manipulateurs rapides sont largement utilisés dans l'industrie, par exemple dans l'emballage alimentaire et la microélectronique. Une architecture parallèle composée d'une plate-forme mobile et d'une plate-forme de base, reliées par deux membres en série, a été conçue et prototypée au Centre for Intelligent Machines de l'Université McGill. Le prototype est surnommé le Peppermill Carrier (PMC). L'objectif du travail présenté dans cette thèse est d'améliorer la vitesse de ce robot, destinée aux opérations à grande vitesse, tout en tenant compte de son élastodynamique, via la modélisation et la commande. Le concept de ressort généralisé, renforcé par la méthode des éléments finis, est utilisé pour obtenir le modèle élastodynamique du robot. Les fréquences propres du robot sont obtenues le long du cycle Adept de test, qui sert à identifier les postures de faible rigidité ; les fréquences naturelles sont ensuite appliquées pour construire un modèle mathématique amélioré du robot. En cours de route, des indices de rigidité sont définis afin d'aider le concepteur et l'ingénieur automaticien à répondre aux exigences de performance. Le modèle mathématique du robot, qui tient compte de la nature flexible des membrures, est formulé. De plus, un régulateur quadratique linéaire à programmation du gain, associé à un filtre de Kalman étendu, est conçu et appliqué pour commander les opérations rapides. Sur la base du contrôleur d'ordonnancement du gain, un régulateur quadratique linéaire à gain constant, associé à un filtre de Kalman étendu à gain constant, s'avère efficace pour commander le robot lors d'opérations rapides, tout en suivant une trajectoire représentative prescrite. Inspiré des résultats de simulation obtenus par ce régulateur, un asservissement odométrique-tachymétrique à propagation avant, basé sur le schéma en mode glissant est également proposé. L'utilisation de ces asservissements linéaires permet de réduire la complexité des calculs. La faisabilité d'un asservissement linéaire pour un système non linéaire tel que le PMC est également discutée. Enfin, une comparaison entre quatre systèmes de commande est effectuée pour analyser leurs avantages et leurs inconvénients.

Contributions

Pick-and-place robots have attracted attention in recent years. How to improve the speed has been the focus of many a research work. The contribution of the author targets the speed of pick-and-place robots through elastodynamics analysis, modelling, and control.

The elastostatic and elastodynamics analyses of a pick-and-place robot are conducted based on the concept of generalized spring. The first natural frequency is obtained through elastodynamics analysis, to evaluate the elastodynamics performance of the robot along the trajectory and used to build the dynamics model of the robot. Furthermore, the natural frequency can also be used in the structural optimum design of the robot in the future. Our analysis should help improve the modelling accuracy, especially for flexible-links with complex shapes or made of special materials. This method can be applied to other serial and parallel architectures.

The dynamics model of the PMC is built based on the concept of the natural orthogonal complement. The link flexibility is not ignorable under high-speed conditions. Therefore, a virtual-flexible-motor-shaft model is built by taking the link flexibility into consideration. This research work takes process noise, measurement noise, and parameter uncertainties into the dynamics model as well, to make it closer to reality, which will be further applied to test the robustness of the controllers.

Several control schemes are designed to control the PMC tracking the desired trajectories. A gain-scheduling linear quadratic regulator combined with an extended Kalman filter is first designed to control the robot. From the design of gain-scheduling control schemes, a constant-gain linear quadratic regulator combined with a constant-gain extended Kalman filter, a linear controller is found to be effective to control the robot under a fast operation speed, three times faster than the record. Inspired by that, another linear controller, a feed-forward PD controller based on the sliding-mode scheme, is designed. The simulation results show that the tracking performance of these linear controllers is promising, which means that these controllers can control the nonlinear system even at a high speed. This contribution should decrease the computational complexity sharply and improve the real-time performance in practice.

Acknowledgments

Firstly, I would like to express my most sincere gratitude to my supervisors, Professors Jorge Angeles and James Richard Forbes. They gave me unreserved guidance, which helped me overcome the difficulties found throughout my research work. I am very proud to be their student. I really appreciate their supervision, not only in academic research, but also in choosing a direction in life.

Furthermore, I would like to express my sincere gratitude to Bruno Belzile, Ting Zou, Peyman Karimi-Eskandary, Qi Sun and Wei Li for their unreserved support on academic research, and the unforgettable memories in life.

More importantly, I would like to express my deepest gratitude to my parents, Ming Yin and Shufeng Zhang, who gave me life, the best possible education, and endless love. I am here because they carried me on their backs.

Contents

1 Introduction **1**
1.1 Background and Motivation 1
1.2 Thesis Organization 7

2 Elastostatic Analysis **10**
2.1 Introduction 10
2.2 Research Methodology 10
2.2.1 The Small-amplitude Rotation Matrix 10
2.2.2 Generalized Spring 12
2.2.3 The Small-amplitude Displacements of Two Articulated Generalized Springs 13
2.3 Case Study: Peppermill Carrier 14
2.3.1 Elastostatics Model 14
2.3.2 Elastostatic Analysis 16
2.3.3 Stiffness Indices 20
2.3.4 Numerical Results 21

3 Elastodynamics Analysis **24**
3.1 Introduction 24
3.2 Calculation of the Mass Matrix 24
3.3 Fourier Analysis 29
3.3.1 Methodology 29
3.3.2 Numerical Results 30
3.4 Modal Analysis 30
3.4.1 Methodology 32

3.4.2 Numerical Results 32

4 Dynamics Modelling 34
4.1 Introduction 34
4.2 Rigid-link Conservative Dynamics Model 34
4.3 Model Enhancement 39
4.4 Dynamics Model of the Virtual Flexible Motor Shaft 40

5 Control Schemes 42
5.1 Introduction 42
5.2 Gain-scheduling: Linear Quadratic Regulator and Kalman Filter 42
5.2.1 Introduction of the Gain-scheduling Controller 42
5.2.2 Operation Points 43
5.2.3 Linearization 44
5.2.4 State-space Form 46
5.2.5 Linear Quadratic Regulator and Kalman Filter 46
5.2.6 Gain-scheduling Method 48
5.2.7 Combination 48
5.3 Linear Quadratic Regulator and Extended Kalman Filter 49
5.3.1 Extended Kalman Filter 49
5.4 Constant-gain Controller 49
5.5 Feed-forward PD Controller Based on the Sliding Mode Scheme 50
5.6 Simulation 52
5.6.1 1 Cycle Per Second 52
5.6.2 10 Cycles Per Second 54
5.6.3 Sine-wave Trajectory 59
5.7 Discussion 61

6 Conclusions and Recommendations for Future Work 66
6.1 Conclusions 66
6.2 Future Work 67

References 68

List of Figures

2.1 The concept of generalized spring: (a) two rigid plates coupled by a generalized spring; (b) the coupling of two generalized springs via a R joint . . 14
2.2 The models of the PMC: (a) kinematics chain (b) elastostatic model . . . 15
2.3 Cartesian coordinate and body-fixed coordinates 19
2.4 The rotational and translational square root eigenvalues along the Adept test cycle trajectory 22
2.5 The rotational and translational stiffness indices along the Adept test cycle trajectory 23

3.1 Side view of limb J 25
3.2 The test trajectory plots: (a) the translation along the x-axis, (b) the translation along the y-axis, (c) the translation along the z-axis , and (d) the rotation about the z-axis 30
3.3 Amplitudes of the harmonics of the four independent motions vs. frequency (1 cycle/s): (a) translation along the x-axis; (b) translation along the y-axis; (c) translation along the z-axis; (d) rotation about the z-axis 31
3.4 Amplitudes of the harmonics of the four independent motions vs. frequency (2 cycles/s): (a) translation along the x-axis; (b) translation along the y-axis; (c) translation along the z-axis; (d) rotation about the z-axis 31
3.5 The evolution of the first natural frequency of the PMC along the test trajectory 33

4.1 Current versoin of the PMC 35
4.2 Side view of limb J 38
4.3 PMC total energy and the actuators work 38

4.4 VFMS model 40

5.1 Control scheme diagram 43
5.2 Operation points of the path 44
5.3 The tracking errors of a 1-cycle/s operation in Cartesian space of the gain-scheduling LQR combined with the KF controller: (a) translational tracking errors; (b) rotational tracking error 53
5.4 The tracking errors of a 1-cycle/s operation in Cartesian space of the gain-scheduling LQR combined with the SEKF controller: (a) translational tracking errors; (b) rotational tracking error 54
5.5 The tracking errors of a 1-cycle/s operation in Cartesian space of the gain-scheduling LQR combined with the REKF controller: (a) translational tracking errors; (b) rotational tracking error 54
5.6 The tracking errors of a 1-cycle/s operation in Cartesian space of the constant-gain LQR combined with the constant-gain EKF controller: (a) translational tracking errors; (b) rotational tracking error 55
5.7 The tracking errors of a 1-cycle/s operation in Cartesian space of the feed-forward PD controller, based on the sliding-mode scheme: (a) translational tracking errors; (b) rotational tracking error 55
5.8 Estimation errors of angular positions of the KF: (a) $\delta\psi_1$; (b) $\delta\psi_2$; (c) $\delta\psi_3$; and (d) $\delta\psi_4$ 56
5.9 Estimation errors of angular positions of the SEKF: (a) $\delta\psi_1$; (b) $\delta\psi_2$; (c) $\delta\psi_3$; and (d) $\delta\psi_4$ 57
5.10 Estimation errors of angular positions of the REKF: (a) $\delta\psi_1$; (b) $\delta\psi_2$; (c) $\delta\psi_3$; and (d) $\delta\psi_4$ 58
5.11 The tracking errors at 10 cycles/s in Cartesian space of the constant-gain LQR combined with the constant-gain EKF controller: (a) translational tracking errors; (b) rotational tracking error 59
5.12 The tracking errors at 10 cycles/s in Cartesian space of the feed-forward PD controller, based on the sliding-mode scheme: (a) translational tracking errors; (b) rotational tracking error 60

5.13 The sine-wave trajectory plots: (a) the translation along the x-axis, (b) the translation along the y-axis, (c) the translation along the z-axis , and (d) the rotation about the z-axis 60
5.14 The tracking errors of the sine-wave trajectory in Cartesian space of the constant-gain controller: (a) translational tracking errors; (b) rotational tracking error 61
5.15 The tracking errors of the sine-wave trajectory in Cartesian space of the feed-forward PD controller, based on the sliding-mode scheme: (a) translational tracking errors; (b) rotational tracking error 61
5.16 The tracking errors at 10 cycles/s in Cartesian space of the constant-gain LQR combined with the constant-gain EKF controller and no feed-forward signal: (a) translational tracking errors; (b) rotational tracking error 62
5.17 The Frobenius norms of (a) $\mathbf{K}_1$ and (b) $\mathbf{K}_2$ along the 1 cycle/s Adept trajectory 64
5.18 The Frobenius norms of (a) $\mathbf{A}_1$ and (b) $\mathbf{A}_2$ along the 1 cycle/s Adept trajectory 64
5.19 The Frobenius norm of $\mathbf{B}_1$ along the 1 cycle/s Adept trajectory 65

List of Acronyms

BP	base platform
C	cylindrical joint
C-drive	cylindrical drive
CIM	Centre for Intelligent Machines
COM	centre of mass
CPM	cross-product matrix
dof	degree of freedom
EKF	extended Kalman filter
F	planar joint
FEA	finite element analysis
H	helical joint
HOT	higher-order terms
KF	Kalman filter
LKP	lower kinematic pair
LQR	linear quadratic regulator
MP	moving platform
P	prismatic joint
PD	proportional-derivative
PID	proportional-integral-derivative
PKM	parallel-kinematics machine
PMC	Peppermill Carrier
PPO	pick-and-place operation
R	revolute joint
REKF	real-time extended Kalman filter

S	spherical joint
SAD	small-amplitude displacement
SCARA	Selective Compliance Assembly Robot Arm
SEKF	semi-real-time extended Kalman filter
SMG	Schönflies-motion generator
VFMS	virtual-flexible-motor-shaft

Chapter 1

Introduction

1.1 Background and Motivation

Robots can be broadly classified as serial and parallel. Serial robots are well developed; they are known to offer a large workspace with respect to their footprint, dexterous capabilities and ease of control. However, compared to serial robots, parallel robots offer many advantages in terms of speed, accuracy, dynamic response, load-carrying capacity, and stiffness, as required by industry.

Early work on the kinematics of parallel robots was reported by Hunt [1]. In 2000, many properties of parallel robots, including architecture, kinematics, singular configurations, workspace, velocity, acceleration, static analysis, dynamics and design were systematically discussed by Merlet [2].

Selective Compliance Assembly Robot Arm (SCARA) systems make an important class of parallel robots. The set of motions produced by such systems is known to form a Lie subgroup [3], the Schönflies subgroup, of the group of rigid-body motions [4, 5]. These systems are designed with four degrees of freedom (dof), namely three independent translations and one rotation about one axis of fixed orientation. The first SCARA system, of the serial type, was proposed by Makino [6] in the early eighties. Such systems were developed in the late 20th century [7]. SCARA systems targeted fast pick-and-place operations (PPO), as those found in the assembly of electronic devices with a flat geometry [8]. In order to satisfy the market demand, namely, faster robots and robots with higher load-carrying capacity, ABB Robotics came up with a novel architecture, the ABB IRB series, dubbed "a transfer robot", which features a kinematic chain that carries a Π-joint, namely, a planar parallelo-

gram linkage. The Π-joint was introduced by Wohlhart in 1991 [9], then applied by Hervé and Sparacino [10] to design a three-dof parallel robot, the Y-Star, to produce translation of its moving platform (MP). Wohlhart [11] and Dietmaier [12] conducted further work on mechanical systems with the Π-joint later.

The Schönflies-motion subgroup, first identified by Schönflies [4, 5], includes four degrees of freedom, namely three independent translations and one rotation about a fixed-direction axis. Bottema and Roth [5] first named this kind of motion Schönflies. The relationship between the Schönflies subgroup and the four-dof motion SCARA was stated by Hervé [3]. The H4 robot [13], a parallel Schönflies motion generator (SMG), was first proposed by a French-Japanese team. It was patented as a four-degree-of-freedom parallel robot in 2001 [14]. The robot has one moving platform, one base platform and four identical limbs. A detailed review on the structural synthesis of SMG was published by Gogu [15], who claimed that there are three kinds of methods used for the structural synthesis of SMG, based on: displacement group theory [16, 17, 18, 19, 20]; screw algebra [21, 22, 23, 24, 25]; and the theory of linear transformations [26, 27]. Kim et al. [28] summarized the state of the art of SMGs based on their active joints and limb-joint types.

Closely related to SMGs, the Delta robot [29] has one base-platform (BP), one MP and three identical limbs. The original concept of this robot produces three-dof translations[1]. The architecture was enhanced in Clavel's patent [30] by adding a telescopic Cardan shaft. The enhanced version is a SMG; many four-limb parallel architectures are based on this design. This robot has four motors fixed on the BP; three of them are used to produce three-dof translations of the MP, the fourth one being used to control the rotation of the gripper on the MP. This design produces an unlimited rotation. Vischer et al. [31] improved the kinematic accuracy of the Delta robot, whose dynamics was studied by Staicu et al. [32]. More recently, ABB Robotics developed a robot on the basis of Delta, dubbed IRB 340 FlexPicker, whose architecture is a serial-parallel SCARA system.

There are two kinds of parallel SMG architectures, namely, four-limb and two-limb architectures. The former are plagued with limb interference. Limb interference results in insufficient rotation ability, limited to an angle smaller than 180°. From 1999 to 2015, many attractive four-limb parallel architectures were proposed, such as H4 [13], I4L [33], I4R [34], Heli4 [35] and PAR4 [36]. The improved version of PAR4 finally became the Quattro robot [37, 38], produced by Adept Technologies Inc., which is the fastest parallel

[1] Compared with its workspace

robot nowadays. Gosselin [39] pointed out that Delta has a bulky framework and a large footprint compared with its workspace volume, besides a low torsional stiffness.

Compared with four-limb SMGs, two-limb SMGs have smaller footprint and virtually unlimited rotational angular MP, but their stiffness is reduced [7]. There is a scarce literature on two-limb SMGs. Angeles et al. proposed an overconstrained two-limb SMG [40, 19, 41] and a two-limb isotropic SMG dubbed the McGill SMG [42, 43]. Isotropy, associated with the condition number of the robot Jacobian matrix [44], offers the maximum dexterity at a given robot posture. Angeles and his team studied the kinematics and dynamics [45], home posture [46], kinematic conditioning and the inertial conditioning [47] of the McGill SMG. Two-limb isoconstrained architectures have many advantages, such as more compact envelope, ease of control and low sensitivity to manufacturing errors [48]. Mechanical isotopy improves the robustness of kinetostatic, elastostatic and elastodynamic performance [49]. Friedlander, Harada and Angeles, based on an isoconstrained two-limb SMG, first disclosed by Lee and Lee [50, 51], designed a two-limb SMG, dubbed the PMC [52]. A prototype of this robot was built at the Centre for Intelligent Machines (CIM), McGill University. The PMC is driven by two identical drives, each drive, the *C-drive* [53], designed with a symmetric architecture, driven by two identical motors, and intended to produce cylindrical displacements—rotation about one axis and translation in a direction parallel to the axis. The C-drive design is based on a differential mechanism of the cylindrical subgroup; it produces rotational motion and independent translational motion in the direction of the axis of rotation. A translating Π-joint was later proposed to enhance the load-carrying capacity of the C-drive [54]. Moreover, a cable-driven architecture is proposed for SMGs, which reduces the design constraints brought about by screw joints [55].

In order to measure the performance and the speed of a pick-and-place robot, a standard industrial test cycle was introduced. This is known as the *Adept cycle*. This trajectory involves a vertical upward translation of 25 mm, a horizontal translation of 300 mm and a final vertical downward translation of 25 mm. The MP of the SCARA system has to move through this trajectory back and forth with a rotation of 180°, along the horizontal segment, in a given cycle time [56]. As the Adept cycle is non-smooth, for it involves corners, Nabat [57] introduced an improved cycle. The cycle consists in a smoothed path, along with its time-history, to make it suitable for fast Schönflies-motion generation. To this end, Nabat proposed a combination of clothoids and a schedule, all intended to reduce the motor torques required to traverse the path by 50%. The clothoid, also called spiral of

Cornu, is a curve whose curvature is equal to its arclength[2]. Garneau et al. [56] in turn, proposed a smooth blending of the non-smooth Adept curve using cubic Lamé curves and an optimum selection of the blending points on the vertical and horizontal segments, such that the kinetic energy of the robot with an archetypical payload undergoes a *minimum variation*, which means that the rms value of the time-derivative of the kinetic energy throughout the whole cycle is minimized. The minimum cycle time of the Quattro robot is three cycles per second, leading to higher than 15g accelerations and two kilograms of rated payload.

Paccot et al. [58] published a review on the dynamic control of PKM. The proportional-integral-derivative (PID) and the computed-torque control are the two most popular control schemes. These schemes have been developed in the joint and the Cartesian spaces, respectively.

The best known control method is PID control, also called linear single-axis control, which is widely applied in industry. However, PID control has one serious drawback. PID control is a linear control method, unable to provide nonlinear compensation, leading to insufficient accuracy when applied to fast serial [59] and parallel robots [60]. It is not ideal to use one set of PID gains in the whole workspace because robot dynamics changes from posture to posture [61]. Therefore, restricting the workspace of parallel robots is a solution, where the parallel robot has a low dynamic coupling and can operate at its maximum speed and acceleration [62]. Another solution is trajectory planning, using dynamic modelling [63, 64] and interpolation in the time domain that takes place at distinct, adapted time-intervals [65, 66]. The trajectory can be smoothed by such adapted time interpolation method and feedforward compensation [67]. However, the drawback of this method is a decrease in speed. Some optimal PID control methods have been proposed, such as gain tuning with dynamic consideration [68] and time-varying nonlinear gains [60].

Computed-torque control is based on the inverse-dynamics model [59]. The integral gain is applied to compensate for unmodelled phenomena and to improve the positioning accuracy. The biggest advantage of this method is that the dynamic response of the system is compensated for in the whole workspace. However, this advantage is only achievable when the dynamic model is accurate enough, which can be achieved by means of inertial-parameter identification. Identification methods of this kind were reviewed by Wu et al. [69].

[2]The parametric formula of the clothoid: $(\int_0^t \cos(x^2/2)dx, \int_0^t \sin(x^2/2)dx)$

Moreover, a more complex model is one more alternative solution to cope with the modelling error. Kock and Schumacher [70] proposed a dynamics model of a flexible body with deformable, as opposed to rigid, links, which improved the modelling accuracy. Oen and Wang [64] proposed a model taking task-influence and external torques into account.

There is an extensive related literature [71, 72, 73, 74] for the control of PKMs in Cartesian-space. Firstly, the equivalent of PID control in Cartesian-space will be discussed. Some work only considered the MP dynamics. A numerical, estimated model is usually added in the control loop, thereby leading to a decrease in accuracy and stability, with an increase in control complexity. Only the MP inertia is considered and leg inertia is neglected, which is obviously not applicable when the legs are as heavy, or even heavier, than the MP. Some work has only considered leg dynamics, which is neither applicable. When both MP and leg dynamics are considered, compensation will be more efficient. Vivas and Poignet [75] applied predictive control to a high-speed PKM, but this calls for a heavy computational load.

However, computed-torque control in Cartesian-space is computationally less demanding and offers a better or equal performance than PID control, because the only computational burden is mapping the dynamics of Cartesian-space into the active joint-space by means of the transposed Jacobian [76]. The computational complexity is lower than that required by the forward-kinematics problem.

Therefore, compared with joint-space control [58], Cartesian-space control is state-feedback control, ensuring a better accuracy and a lower computational burden. Cartesian-space control provides the error between desired and actual MP trajectory. It ensures a more direct task control than joint-space control, which improves the accuracy. Moreover, the MP pose will change if there is a disturbance in the joint trajectory, while Cartesian-space control observes the pose of the MP and brings it back to its reference trajectory.

However, it should be noted that even though Cartesian-space control offers many advantages over joint-space control, it is still applied occasionally because the accurate measurement of the MP pose is hard [77]. In most of the literature, forward kinematics is applied to estimate the MP pose. However, forward kinematics is computationally highly demanding [78]. An adaptive algorithm was proposed by Merlet [79], while metrological redundancy was proposed by Baron and Angeles [80] and Marquet et al. [81], which can improve stability and control accuracy. Model accuracy plays an important role in forward kinematics. The parameters of the dynamics model carry uncertainty, which strongly affects

the performance of control algorithms, especially under high-speed operations. Therefore, inertial-parameter identification plays an important role in model-based control algorithms. Wu et al. [69] reviewed the methods and models on dynamic identification, optimal trajectory, validation and applications. Inverse dynamics control offers a good performance if all the inertial parameters are known accurately. Laser tracking and computer vision are two main methods to measure the MP pose directly. However, laser tracking is expensive and cannot measure the MP attitude. Therefore, laser tracking is out of the question in our case. Newman et al. [82] applied this tool to kinematic identification. Computer vision, i.e., visual servoing, is more widely used in control, even though it is not as fast and accurate as laser tracking. Kino et al. [83] and Dallej [84] applied this method successfully to PKMs. Fast visual servoing was applied to a serial robot by Ginhoux et al. [85].

In the last ten years, the literature on PKM control has surged. Control based on PD/PID is the most widely applied method because it is simple to use and offers good performance [86, 87]. Literature on PID control, combined with model-based control, is availiable [88, 89, 90]. Model-based control algorithms are often used in robotics because these algorithms can improve the reliability and precision of the system [91, 92]. Some control techniques, while not widely studied, still offer some attractive features, namely, fuzzy control [93, 94, 95]; cascade control [94, 96]; switch control [97, 98]; iterative learning control [91, 99]; decoupling control [100]; sliding-mode control [101]; active joint-synchronization control [86]; and active vibration control [102].

In the realm of parallel pick-and-place robots, the control schemes applied on the fastest one, the Quattro robot, has attracted the most attention. Three different kinds of control schemes have been applied on the Quattro, namely, sensor-based dynamic control [103], control based on the MP pose [104] via leg-posture observation, and virtual visual servoing control law [105].

We aim at manipulators designed as rigid as possible, but deformation is inevitable due to the inertia forces brought about by high-speed operations. Therefore, manipulator flexibility must be considered in our case. Flexible-link manipulators have been applied in many realms: microsurgical devices [106]; high-precision PPO in industry [107] and decontamination in nuclear sites [108]. However, the flexible components of a parallel manipulator will bring about vibration when high-speed and high-acceleration operations are conducted. Therefore, the residual vibration after the motion stops will lead to longer settling times and lower positioning accuracy. Moreover, vibration impacts trajectory-

tracking precision and system stability [109].

The control of flexible serial manipulators is well recorded in the literature. Benosman and Le Vey [110] reviewed the control of flexible multi-link manipulators between 1983 and 2003. Dwivedy and Eberhard [111] published a survey on the modelling of flexible manipulators and referenced the work related to control. Kiang et al. [112] reported on the control and the pertinent sensor systems of flexible-link manipulators and summarized the advantages and disadvantages of a broad range of flexible-manipulator control methods. Rahimi and Nazemizadeh [113] carried out a review on the "intelligent" control of flexible-manipulators up to 2013, including fuzzy logic, neural networks and genetic algorithms.

However, publications on the control of parallel manipulators with flexible links are scarce. The control of 3-PRR manipulators with three flexible links is well developed. Zhang et al. applied independent modal-space control, input shaper [109], PD feedback control combined with feed-forward computed-torque control [114] to suppress the residual vibration and the structural vibration of the flexible links. Moreover, Lagrange equations, assumed-mode and modal-control [115] are also reportedly applied. Zhang et al. [116, 117, 102, 118, 119, 120] applied several control schemes on the 3-PRR manipulator. The main methods applied by this team are strain-rate feedback control, modal strain-rate feedback control, assumed-mode method and optimal active vibration control.

Except for 3-PRR manipulators, many other kinds of parallel architectures have been studied. Chu and Cui [121] applied input-shaper and adaptive positive position-feedback control to suppress the vibrations of a two-link planar flexible-manipulator. Kozak et al. [122] applied input-shaper to suppress the vibrations of a two-dof parallel manipulator. Burkhardt et al. [123, 124] applied feed-forward control to suppress the vibration of a two-flexible-link manipulator.

1.2 Thesis Organization

Chapter 1 includes the literature review and the motivation of the reported research work. A broad class of pick-and-place robots are discussed in this chapter, while highlighting their pros and cons. The state-of-the-art control schemes for parallel robots and flexible-link parallel robots, a motivation for this research work, are thoroughly discussed in this opening chapter.

Chapter 2 provides the elastostatic analysis of the PKM motivating this work. The

limbs are modelled as flexible bodies in the presence of high-speed operations. The concept of the six-degree-of-freedom generalized spring and the finite element analysis are applied to model the flexible links. This methodology improves the modelling accuracy, especially for flexible links with complex shapes or links made of materials with complex constitutive relations. The stiffness matrix of the PMC is calculated in this chapter. Moreover, the rotational and translational stiffness indices of the Cartesian stiffness matrix of the robot are obtained and plotted along the Adept cycle, which serves to identify the poor-stiffness postures.

Chapter 3 pertains to the elastodynamics analysis of the PKM. This analysis requires the stiffness and mass matrices of the robot. The stiffness matrix is obtained in Chapter 2. The mass matrix is calculated as the Hessian matrix of the kinetic energy generated by the flexible-component motion. The objective of elastodynamics analysis is to obtain the natural frequencies of the robot. The elastodynamics analysis is essential because the natural frequencies should lie far from the excitation frequency spectrum of a highly repetitive mechanical system, to avoid resonance. The elastodynamics analysis of the PMC, as an illustrative example, is conducted. The natural frequencies and the excitation spectrum are plotted along the test cycle of the pick-and-place operation. Finally, the elastodynamic performance of the robot is evaluated, then incorporated into the dynamics model of the robot. These results should be useful in the robot structural optimum design.

Chapter 4 is devoted to building the dynamics model of the PMC. Firstly, the rigid-link dynamics model is obtained by means of the concept of the natural orthogonal complement. In order to make the model closer to reality, joint friction, process noise, measurement noise and parameter uncertainties are added into the dynamics model. Moreover, the flexibility of the arms, forearms and the harmonic drives cannot be ignored in high-speed operations. Therefore, link flexibility is taken into consideration to improve the accuracy of the dynamics model. The flexibility of arms and forearms are not included directly in the dynamics model. The arms and the forearms are modelled as rigid links, their flexibilities transferred to the corresponding motor shafts. The motor shafts are considered connected to the motors by massless torsional springs, namely, lumped spring-mass systems, whose first natural frequency is the same as that of the flexible-link PMC. The dynamics model of the PMC with virtual flexibilities of the motor shafts is built, which has a higher modelling accuracy than that of its rigid-link couterpart.

In Chapter 5, the control scheme design of the PMC is described. Two kinds of gain-

scheduling linear quadratic regulator (LQR) control schemes are proposed, then applied to lead the robot through high-speed operations. In the design of the gain-scheduling controller, a constant-gain LQR control scheme is found to be effective and robust to control the robot in the presence of nonlinear dynamics. Inspired by the constant-gain control scheme, a feed-forward PD controller based on the sliding mode scheme is proposed. Compared with their nonlinear counterparts, linear controllers offer smaller computational complexity and improve the real-time response. The reason why a linear controller is eligible to control a nonlinear system is elucidated. The pros and cons of all four control schemes are discussed.

Chapter 6 summarizes the research work and provides suggestions for future work.

Chapter 2

Elastostatic Analysis

2.1 Introduction

This chapter is devoted to the elastostatic analysis of the PMC. The limbs are considered as flexible bodies under high-speed operations. The concept of six-degree-of-freedom generalized spring, combined with the finite-element analysis, is applied to model the flexible-links. This method improves the modelling accuracy, especially for flexible-links with complex shapes or made of special materials. The stiffness matrix of the PMC is then calculated. Moreover, the rotational and translational stiffness indices are defined and plotted along the Adept test cycle, which serves to identify the poor-stiffness postures.

2.2 Research Methodology

This section includes the research methodology related to the elastostatic analysis. First, the small-amplitude rotation matrix and the corresponding six-dimensional small-amplitude displacement screw are introduced. Afterwards, the concept of the generalized spring is recalled. Moreover, the small-amplitude displacements between two articulated generalized springs are discussed.

2.2.1 The Small-amplitude Rotation Matrix

The natural invariants [125] are invoked to represent a rigid-body rotation from an initial attitude to a new one. These invariants are the angle of rotation ϕ and the unit vector $\mathbf{e}$

parallel to the axis of rotation. The rotation matrix $\mathbf{Q}$ is then given as [125]

$$\mathbf{Q} = \mathbf{1} + (\sin\phi)\mathbf{E} + (1 - \cos\phi)\mathbf{E}^2 \tag{2.1}$$

where $\mathbf{E}$ represents the cross-product matrix (CPM) [125] [1] of $\mathbf{e}$, and $\mathbf{1}$ the 3×3 identity matrix. The angular velocity of a rigid body is obtained as the axial vector $\boldsymbol{\omega}$ of $\boldsymbol{\Omega}$, defined as $\boldsymbol{\Omega} = \dot{\mathbf{Q}}\mathbf{Q}^T = -\mathbf{Q}\dot{\mathbf{Q}}^T$. Hence,

$$\boldsymbol{\omega} = [(\sin\phi)\mathbf{1} + (1 - \cos(\phi)\mathbf{E}) \quad \mathbf{e}] \begin{bmatrix} \dot{\mathbf{e}} \\ \dot{\phi} \end{bmatrix} \tag{2.2}$$

If ϕ is small, then $\sin\phi \to \phi$ and $\cos\phi \to 1$, $\mathbf{Q}$ then becoming

$$\mathbf{Q} = \mathbf{1} + \phi\mathbf{E} \tag{2.3}$$

and the angular velocity reducing, in this case, to

$$\boldsymbol{\omega} = [\phi\mathbf{1} \quad \mathbf{e}] \begin{bmatrix} \dot{\mathbf{e}} \\ \dot{\phi} \end{bmatrix} = \dot{\boldsymbol{\phi}} = \phi\dot{\mathbf{e}} + \dot{\phi}\mathbf{e} \equiv \frac{d}{dt}(\phi\mathbf{e}) \tag{2.4}$$

where $\boldsymbol{\phi} \equiv \phi\mathbf{e} \equiv \text{vect}(\mathbf{Q} - \mathbf{1})$[2].

The Plücker coordinates [126] of a line $\mathcal{L}$ are included in the array $\begin{bmatrix} \mathbf{a}^T & (\mathbf{r} \times \mathbf{a})^T \end{bmatrix}^T$, where $\mathbf{a}$ denotes the unit vector parallel to the line, and $\mathbf{r}$ the position vector of a point R in the line. The unit screw $\mathbf{s}$ is a line with a pitch, namely,

$$\mathbf{s} = \begin{bmatrix} \mathbf{a} \\ \mathbf{r} \times \mathbf{a} + p\mathbf{a} \end{bmatrix} \tag{2.5}$$

where p represents the pitch of the screw, measured in m/rad in this paper.

A six-dimensional small-amplitude displacement (SAD) screw $\mathbf{u}$ is the product of a unit screw $\mathbf{s}$ by a "small" angle of rotation ϕ, i.e.[3],

$$\mathbf{u} = \begin{bmatrix} \phi\mathbf{a} \\ \mathbf{r} \times \phi\mathbf{a} + p\phi\mathbf{a} \end{bmatrix} = \begin{bmatrix} \boldsymbol{\phi} \\ \mathbf{p} \end{bmatrix}, \quad |\phi| << 1 \tag{2.6}$$

[1] The definition of cross-product matrix $\mathbf{V}$ of vector $\mathbf{v}$: $\mathbf{v} \times \mathbf{x} = \mathbf{V}\mathbf{x}$. $\forall \mathbf{x}, \mathbf{v} \in \mathbb{R}^3$.

[2] Denote $\mathbf{V}\mathbf{x} = \mathbf{v} \times \mathbf{x}$. $\forall \mathbf{x}, \mathbf{v} \in \mathbb{R}^3$, then $\text{vect}(\mathbf{V}) = \mathbf{v}$

[3] ϕ is the "small-amplitude" rotation and $\mathbf{p}$ the "small" concomitant translation.

2.2.2 Generalized Spring

Flexible parts can be modelled as six-dimensional generalized springs [127]. The elastic potential energy is generated by the linearly elastic deformation of the flexible parts.

Broadly speaking, a generalized spring is a lump of a massless, linearly elastic material coupling two rigid plates (or bodies, for that matter), i and j, as depicted in Fig. 2.1(a). If the rigid plate j is fixed, then the stiffness matrix $\mathbf{K}$ of the generalized spring is a 6×6 symmetric positive-definite matrix. This matrix is displayed below in block form:

$$\mathbf{K} = \begin{bmatrix} \mathbf{K}_{11} & \mathbf{K}_{12} \\ \mathbf{K}_{12}^T & \mathbf{K}_{22} \end{bmatrix} \tag{2.7}$$

where $\mathbf{K}_{11}$, $\mathbf{K}_{12}$, and $\mathbf{K}_{22}$ are 3×3 blocks, carrying the units of Nm, N and N/m. Then, we will consider the situation in which the two rigid plates can move independently.

A six-dimensional wrench array $\mathbf{w}_i = \begin{bmatrix} \mathbf{n}_i^T & \mathbf{f}_i^T \end{bmatrix}^T$ is now introduced as acting on plate i, where $\mathbf{n}_i$ is a moment with respect to the plate center of mass (COM) and $\mathbf{f}_i$ is a force acting at the plate COM. A balancing wrench $\mathbf{w}_j$ acts on plate j. Due to the two wrenches acting on the lump of elastic material, the two coupled plates undergo corresponding SAD screws, $\mathbf{u}_i$ and $\mathbf{u}_j$. The SAD screw arrays are now cast in the 12-dimensional array $\mathbf{u} = \begin{bmatrix} \mathbf{u}_i^T & \mathbf{u}_j^T \end{bmatrix}^T$. Similarly, $\mathbf{w}_i$ and $\mathbf{w}_j$ are cast in the 12-dimensional array $\mathbf{w} = \begin{bmatrix} \mathbf{w}_i^T & \mathbf{w}_j^T \end{bmatrix}^T$. The wrench array $\mathbf{w}$ is the image of the SAD screw array $\mathbf{u}$ under a 12×12 transformation given by the symmetric stiffness matrix $\mathbf{K}$, partitioned into four 6×6 blocks: $\mathbf{w} = \mathbf{K}\mathbf{u}$. This matrix is displayed below in block form:

$$\mathbf{K} = \begin{bmatrix} \mathbf{K}_{ii} & \mathbf{K}_{ij} \\ \mathbf{K}_{ij}^T & \mathbf{K}_{jj} \end{bmatrix} \tag{2.8}$$

The potential energy of the generalized spring is, thus,

$$V = \frac{1}{2} \begin{bmatrix} \mathbf{u}_i^T & \mathbf{u}_j^T \end{bmatrix} \begin{bmatrix} \mathbf{K}_{ii} & \mathbf{K}_{ij} \\ \mathbf{K}_{ij}^T & \mathbf{K}_{jj} \end{bmatrix} \begin{bmatrix} \mathbf{u}_i \\ \mathbf{u}_j \end{bmatrix} \tag{2.9}$$

While the stiffness matrix $\mathbf{K}$ is of 12×12, its rank is six. The physical meaning of its six-dimensional null space is that the two plates can undergo displacements that leave the lump of elastic material undeformed. This happens when the two plates move as one single

rigid body.

2.2.3 The Small-amplitude Displacements of Two Articulated Generalized Springs

When two generalized springs are coupled by a passive kinematic pair, some dof will be constrained. Each generalized spring has six elastic dof, two *uncoupled* generalized springs then having 12 elastic dof. If a passive kinematic pair[4] brings $m < 6$ constraints, the number of elastic dof of the two coupled generalized springs is $12-m$. Taking the revolute (R) joint as an example, it constrains two rotational and three translational dof of the coupled plates, which is interpreted as follows: with plate i fixed, a wrench $\mathbf{w}_l$ is applied on plate l, shown in Fig. 2.1(b). In the absence of the R joint, plates j and k would be welded, which would lead to $\mathbf{u} = \mathbf{u}'$, where $\mathbf{u}$ and $\mathbf{u}'$ represent the SAD screw of plates j and k, respectively. Under these conditions, the system has 12 elastic dof, six for each generalized spring. The presence of the R joint introduces five constraint-wrenches components, transmitted by plate k onto plate j, which means that only one component of the wrench $\mathbf{w}_j$ transmitted by the R joint to the left-hand generalized spring is independent from those of $\mathbf{w}_k$, acting on plate k. This is the moment transmitted by the R joint, with the right-hand generalized spring acting as a motor that drives this joint. As a consequence, the number of elastic dof of the system of two articulated generalized springs is $12 - 5 = 7$. The difference between $\mathbf{u}$ and $\mathbf{u}'$ can only be a screw with a small-amplitude angle β. This angle is associated with the free motion allowed by the R joint. It is "small" because it is assumed that one plate, e.g., i, is fixed, while plate l undergoes a SAD screw. Therefore, the relation between $\mathbf{u}$ and $\mathbf{u}'$ is

$$\mathbf{u}' = \mathbf{u} + \beta\mathbf{s}, \quad \mathbf{s} = \begin{bmatrix} \mathbf{e}^T & \mathbf{0}^T \end{bmatrix}^T, \quad |\beta| << 1 \tag{2.10}$$

where $\mathbf{e}$ is the unit vector parallel to the axis of the R joint, $\mathbf{0}$ the three-dimensional zero vector and β the small-amplitude angle of relative rotation, shown in Fig. 2.1(b). Different lower kinematic pairs (LKPs) have different $\mathbf{s}$ and different variable(s) β [128][5].

[4] Any of the six lower kinematic pairs: revolute (R), prismatic (P), helical (H), cylindrical (C), planar (F) and spherical (S).

[5] More than one variable is needed in the case of a multi-dof kinematic pair.

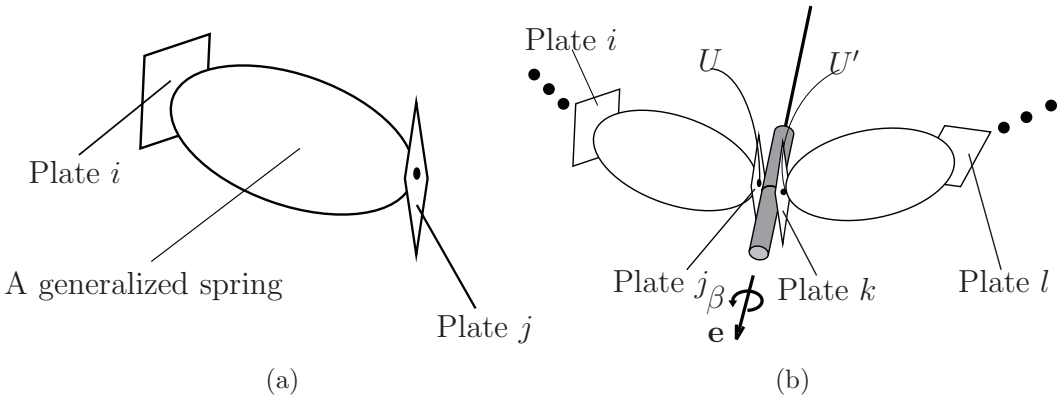

Fig. 2.1: The concept of generalized spring: (a) two rigid plates coupled by a generalized spring; (b) the coupling of two generalized springs via a R joint

2.3 Case Study: Peppermill Carrier

This section is devoted to the elastostatic analysis of the PMC. First, the elastostatic model of the PMC is built, which is applied to obtain the stiffness matrix. Afterwards, the elastostatic analysis is conducted to obtain the stiffness indices, which are used to identify the poor-stiffness postures.

2.3.1 Elastostatics Model

The hypothesis underlying the elastostatic model of the PMC is summarized as: all links are modelled as rigid bodies, except for the arms and forearms. The reason for this hypothesis lies in that the arms and the forearms are much more flexible, than the other links. Notice that the screws of the C-drives and the screws of the Peppermill cannot be assumed flexible, because the PMC cannot work if the screws deform. Moreover, the flexibility of the harmonic drive is taken into consideration.

The kinematic chain of the PMC is shown in Fig. 2.2(a). The robot is modelled as an elastostatic system, like the one in Fig. 2.2(b). Each of the four springs of the figure represents, in fact, a *generalized spring*.

The two arms and the two forearms are thus modelled as massless generalized springs. In following Zou [129], the stiffness matrices of arms and forearms are obtained by finite element analysis (FEA) in their own body-fixed frames. It is assumed that the generalized spring is coupled by two rigid plates. In order to obtain the stiffness matrix of the gen-

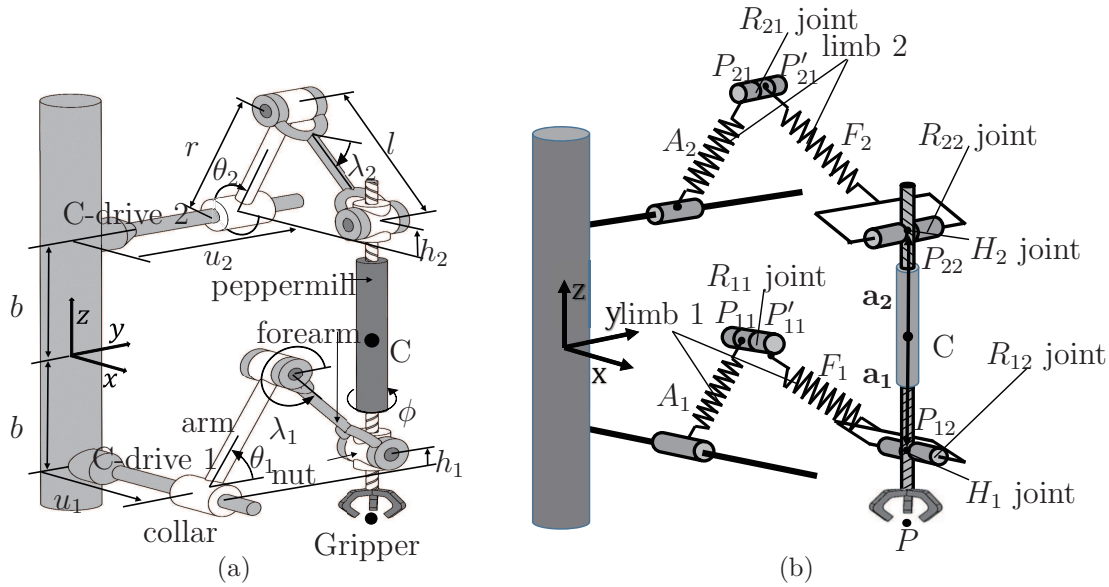

Fig. 2.2: The models of the PMC: (a) kinematics chain (b) elastostatic model

eralized spring in FEA, one rigid plate is locked and an external wrench is added on the other rigid plate to obtained the small-amplitude displacement array. Then, the array and the external wrench are further used to calculate the stiffness matrices of the generalized spring. Therein, $\mathbf{q}_{J1}$ is the SAD screw defined at point P_{J1}, where J is the limb label, for $J = 1, 2$, as depicted in Fig. 2.2(b). Furthermore, $\mathbf{q}_{J2}$ is the SAD screw defined at point P_{J2}. By virtue of the presence of the R_{J1} joint, the SAD screw, defined at point P'_{J1}, becomes

$$\mathbf{q}'_{J1} = \mathbf{q}_{J1} + \delta\beta_J \mathbf{s}_J, \quad \mathbf{s}_J = \begin{bmatrix} \mathbf{e}_J^T & \mathbf{0}^T \end{bmatrix}^T \tag{2.11}$$

where $\mathbf{e}_J$ is the unit vector parallel to the axis of the R_{J1} joint and $\delta\beta_J$ the small-amplitude relative rotation about the same axis.

The forearms are connected to the nuts via R joints of horizontal axes. The SAD screws defined at the COM of the nuts (P_{J2}) and the COM of the Peppermill (C) are represented by $\mathbf{q}_{nJ}$ and $\mathbf{q}_m$, respectively. According to the rigidity assumption and the presence of the R joint, the relationship between $\mathbf{q}_{J2}$ and $\mathbf{q}_{nJ}$ is

$$\mathbf{q}_{J2} = \mathbf{q}_{nJ} + \delta\gamma_J \mathbf{s}_J \tag{2.12}$$

where $\delta\gamma_J$ is the small-amplitude angle of rotation of the R_{J2} joint, and $\mathbf{s}_J$ is defined in eq. (2.11).

The nuts are connected to the Peppermill via H joints of *nominally* vertical axes. The relationship between $\mathbf{q}_{nJ}$ and $\mathbf{q}_m$ is

$$\mathbf{q}_{nJ} = \mathbf{G}_J\mathbf{q}_m + \delta\alpha_J\mathbf{s}_{HJ}, \quad \mathbf{s}_{HJ} = \begin{bmatrix}\mathbf{e}_{HJ}^T & p_J\mathbf{e}_{HJ}^T\end{bmatrix}^T \tag{2.13}$$

where $\delta\alpha_J$ is the small-amplitude angle of rotation of the H_J joint with respect to the direction of its axis, $\mathbf{e}_{HJ}$ the unit vector of its axis and p_J the pitch of the H_J joint.

Moreover, $\mathbf{G}_J$ is the SAD screw *transfer matrix* that transfers the SAD screw of one given rigid body from one point to another point of the same body. In the case at hand, from point C to point P_{J2} of the Peppermill, which is given by

$$\mathbf{G}_J = \begin{bmatrix}\mathbf{1} & \mathbf{0}\\ -\mathbf{A}_J & \mathbf{1}\end{bmatrix} \tag{2.14}$$

where $\mathbf{A}_J = \text{CPM}\ (\mathbf{a}_J)$, vector $\mathbf{a}_J$ stemming from C and ending at P_{J2}.

2.3.2 Elastostatic Analysis

The objective of elastostatic analysis is to obtain the stiffness performance of the PMC along the test trajectory. The Cartesian stiffness matrix $\mathbf{K}_e \in \mathbb{R}^{6\times6}$ maps the SAD screw of the Peppermill into the external wrench applied onto it, which is given by

$$\mathbf{w}_{\text{ext}} = \mathbf{K}_e\mathbf{q} \tag{2.15}$$

where $\mathbf{w}_{\text{ext}}$ is the external wrench and $\mathbf{q}$ the SAD screw of the Peppermill. If we apply a unit external wrench on the six different directions of the wrench space, separately, the corresponding SAD screws are nothing but the columns of the inverse matrix of the Cartesian stiffness matrix.

Firstly, a unit external force in the x-direction, $\mathbf{w}_{fx}$, is applied at the centre of mass C of the Peppermill. From the mechanical structure of the PMC, we can find that $\mathbf{w}_{fx}$ will bring about a deformation of the arm and the forearm of limbs 1 and 2. Through the force analysis of the Peppermill, balancing forces $\mathbf{f}_{f1p}$ and $\mathbf{f}_{f2p}$ are added on the Peppermill at points P_{12} and P_{22}, respectively. Since the effects of a force are mutual, reactive forces

$\mathbf{f}_{pf1} = -\mathbf{f}_{f1p}$ and $\mathbf{f}_{pf2} = -\mathbf{f}_{f2p}$ are applied on the forearms of limbs 1 and 2, henceforth termed forearm 1 and forearm 2. Therefore, we can obtain the SAD screws of the two forearms in the forms

$$\mathbf{q}_{f1} = (\mathbf{K}^{F1})^{-1}\mathbf{w}_{pf1}, \quad \mathbf{q}_{f2} = (\mathbf{K}^{F2})^{-1}\mathbf{w}_{pf2} \tag{2.16}$$

where $\mathbf{K}^{F1}$ and $\mathbf{K}^{F2}$ are the Cartesian stiffness matrices of forearm 1 and forearm 2, respectively, while $\mathbf{w}_{pf1} = \begin{bmatrix}\mathbf{m}_{pf1}^T & \mathbf{f}_{pf1}^T\end{bmatrix}^T$ and $\mathbf{w}_{pf2} = \begin{bmatrix}\mathbf{m}_{pf2}^T & \mathbf{f}_{pf2}^T\end{bmatrix}^T$.

On the other hand, the forces acting on forearm 1 and forearm 2 will be transferred to arm 1 and arm 2 via corresponding passive revolute joints. The SAD screws of arm 1 and arm 2 are given by

$$\mathbf{q}_{a1} = (\mathbf{K}^{A1})^{-1}\mathbf{w}_{f1a1}, \quad \mathbf{q}_{a2} = (\mathbf{K}^{A2})^{-1}\mathbf{w}_{f2a2} \tag{2.17}$$

where $\mathbf{K}^{A1}$ and $\mathbf{K}^{A2}$ is the Cartesian stiffness matrix of the corresponding arm, and $\mathbf{w}_{f1a1} = \mathbf{w}_{pf1}$ and $\mathbf{w}_{f2a2} = \mathbf{w}_{pf2}$. A SAD-screw transfer matrix $\mathbf{G}_{Jc}$ is defined as

$$\mathbf{G}_{Jc} = \begin{bmatrix}\mathbf{1} & \mathbf{0} \\ -\mathbf{A}_{Jc} & \mathbf{1}\end{bmatrix} \tag{2.18}$$

where $\mathbf{A}_{Jc} = \text{CPM}\ (\mathbf{a}_{Jc})$, vector $\mathbf{a}_{Jc}$ stemming from P_{J2} and ending at C. $\mathbf{G}_{Jc}$ transfers the SAD screw of point P_{J2} to point C, the COM of the Peppermill. Therefore, the total deformation caused by the external wrench $\mathbf{w}_{fx}$ is

$$\mathbf{q}_{wfx} = \mathbf{G}_{1c}(\mathbf{q}_{a1} + \mathbf{q}_{f1}) + \mathbf{G}_{2c}(\mathbf{q}_{a2} + \mathbf{q}_{f2}) \tag{2.19}$$

The SAD screws, $\mathbf{q}_{wfy}$, $\mathbf{q}_{wmx}$, $\mathbf{q}_{wmy}$ and $\mathbf{q}_{wmz}$, caused by the unit external wrenches $\mathbf{w}_{fy}$, $\mathbf{w}_{mx}$, $\mathbf{w}_{my}$ and $\mathbf{w}_{mz}$ can be obtained likewise.

The deformation $\mathbf{q}_{wfz}$, caused by the unit external force in the z-direction, will be analyzed separately because it is related to the flexibility of the harmonic drive.

A unit external force $\mathbf{w}_{fz}$, is applied at the center of mass C of the Peppermill in the z-direction. Because of the symmetric mechanical structure, the wrenches acting on the Peppermill by forearm 1, $\mathbf{w}_{f1p}$, and forearm 2, $\mathbf{w}_{f2p}$, equals half of $\mathbf{w}_{fz}$, respectively. Therefore, the deformation of forearms 1 and 2 are given by

$$\mathbf{q}_{f1} = (\mathbf{K}^{F1})^{-1}\mathbf{w}_{pf1} \tag{2.20}$$

$$\mathbf{q}_{f2} = (\mathbf{K}^{F2})^{-1}\mathbf{w}_{pf2} \tag{2.21}$$

where $\mathbf{w}_{pf1} = -\mathbf{w}_{f1p}$ and $\mathbf{w}_{pf2} = -\mathbf{w}_{f2p}$.

On the other hand, the deformation of arms 1 and 2 are given by

$$\mathbf{q}_{a1} = (\mathbf{K}^{A1})^{-1}\mathbf{w}_{f1a1} \tag{2.22}$$

$$\mathbf{q}_{a2} = (\mathbf{K}^{A2})^{-1}\mathbf{w}_{f2a2} \tag{2.23}$$

where $\mathbf{w}_{f1a1} = \mathbf{w}_{pf1}$ and $\mathbf{w}_{f2a2} = \mathbf{w}_{pf2}$.

As for the angular displacements of the harmonic drives, which are given by

$$\alpha_1 = f_{f1a1}\cos(\theta_1)r/k_{\text{harm}} \tag{2.24}$$

$$\alpha_2 = f_{f2a2}\cos(\theta_2)r/k_{\text{harm}} \tag{2.25}$$

where f_{f1a1} and f_{f2a2} are the force components in the z direction of $\mathbf{w}_{f1a1}$ and $\mathbf{w}_{f2a2}$, θ_1 and θ_2 defined in Fig. 2.2(a), k_{harm} the torsional stiffness of the harmonic drive. Therefore, the deformation caused by the harmonic drives at points P_{11} and P_{21} are

$$\mathbf{q}_{h1} = \begin{bmatrix}\mathbf{0}^T & \mathbf{d}_{h1}^T\end{bmatrix}^T, \quad \mathbf{d}_{h1} = \begin{bmatrix}0 & -\alpha_1 r\sin(\theta_1) & \alpha_1 r\cos(\theta_1)\end{bmatrix}^T \tag{2.26}$$

$$\mathbf{q}_{h2} = \begin{bmatrix}\mathbf{0}^T & \mathbf{d}_{h2}^T\end{bmatrix}^T, \quad \mathbf{d}_{h2} = \begin{bmatrix}\alpha_2 r\sin(\theta_2) & 0 & \alpha_2 r\cos(\theta_2)\end{bmatrix}^T \tag{2.27}$$

where $\mathbf{0}$ is the three-dimensional zero vector.

The total deformation caused by the unit external wrench $\mathbf{w}_{fz}$ is

$$\mathbf{q}_{wfz} = \mathbf{G}_{1c}(\mathbf{q}_{a1} + \mathbf{q}_{f1} + \mathbf{q}_{h1}) + \mathbf{G}_{2c}(\mathbf{q}_{a2} + \mathbf{q}_{f2} + \mathbf{q}_{h2}) \tag{2.28}$$

Since the unit external forces and moments are applied at the COM of the Peppermill, the SAD screws are nothing but the columns of the inverse matrix of the Cartesian stiffness matrix of the PMC. Therefore, matrix $\mathbf{K}_e$ is given by

$$\mathbf{K}_e = \begin{bmatrix}\mathbf{q}_{wmx} & \mathbf{q}_{wmy} & \mathbf{q}_{wmz} & \mathbf{q}_{wfx} & \mathbf{q}_{wfy} & \mathbf{q}_{wfz}\end{bmatrix}^{-1} \tag{2.29}$$

In the above analysis, $\mathbf{K}^{AJ}$ and $\mathbf{K}^{FJ}$ are defined in the base frame and $\bar{\mathbf{K}}^{AJ}$ and $\bar{\mathbf{K}}^{FJ}$

denote the stiffness matrices of arms and forearms defined in the body-fixed frame. $\bar{\mathbf{K}}^{AJ}$ and $\bar{\mathbf{K}}^{FJ}$ are posture-independent, obtained by FEA. $\mathbf{K}^{AJ}$ and $\mathbf{K}^{FJ}$ are posture-dependent, derived from $\bar{\mathbf{K}}^{AJ}$, $\bar{\mathbf{K}}^{FJ}$ by means of similarity transformations in terms of 6×6 rotation matrices, as described below.

The coordinate frames of arms and forearms are shown in Fig. 2.3. $\mathcal{F}_0$ represents the fixed frame. $\mathbf{Q}_{J10}$ is the rotation matrix that carries $\mathcal{F}_{J1}$ into $\mathcal{F}_0$. Similarly, $\mathbf{Q}_{J21}$ and $\mathbf{Q}_{J20}$

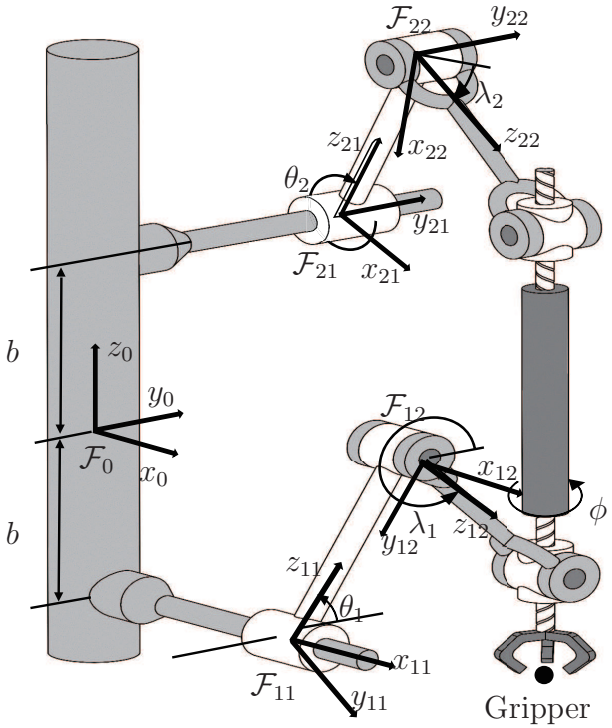

Fig. 2.3: Cartesian coordinate and body-fixed coordinates

are the rotation matrices that carry $\mathcal{F}_{J2}$ into $\mathcal{F}_{J1}$ and $\mathcal{F}_{J2}$ into $\mathcal{F}_0$, respectively.

A 6×6 rotation matrix $\mathbf{R}_{J10}$ is now introduced to transfer six-dimensional SAD screws from $\mathcal{F}_{J1}$ into $\mathcal{F}_0$:

$$\mathbf{R}_{J10} = \begin{bmatrix} \mathbf{Q}_{J10} & \mathbf{O} \\ \mathbf{O} & \mathbf{Q}_{J10} \end{bmatrix} \tag{2.30}$$

Likewise, the 6×6 rotation matrices $\mathbf{R}_{J21}$ and $\mathbf{R}_{J20}$ are further introduced:

$$\mathbf{R}_{J21} = \begin{bmatrix} \mathbf{Q}_{J21} & \mathbf{O} \\ \mathbf{O} & \mathbf{Q}_{J21} \end{bmatrix}, \quad \mathbf{R}_{J20} = \begin{bmatrix} \mathbf{Q}_{J20} & \mathbf{O} \\ \mathbf{O} & \mathbf{Q}_{J20} \end{bmatrix} \tag{2.31}$$

where $\mathbf{R}_{J21}$ and $\mathbf{R}_{J20}$ carry $\mathcal{F}_{J2}$ into $\mathcal{F}_{J1}$ and $\mathcal{F}_{J2}$ into $\mathcal{F}_0$, respectively.

Therefore, the relationships between $\mathbf{K}^{AJ}$ ($\mathbf{K}^{FJ}$) and its counterpart $\bar{\mathbf{K}}^{AJ}$ ($\bar{\mathbf{K}}^{FJ}$) are readily derived:

$$\mathbf{K}^{AJ} = \mathbf{R}_{J10}^T \bar{\mathbf{K}}^{AJ} \mathbf{R}_{J10}, \quad \mathbf{K}^{FJ} = \mathbf{R}_{J20}^T \bar{\mathbf{K}}^{FJ} \mathbf{R}_{J20} \tag{2.32}$$

2.3.3 Stiffness Indices

In order to characterize how stiff the PKM is, stiffness indices are introduced. The Cartesian stiffness matrix is dimensionally inhomogeneous, and hence, cannot admit a norm[6]. Therefore, a *normalization* of the Cartesian stiffness matrix is needed.

The Cartesian stiffness matrix $\mathbf{K}_e$ maps a SAD screw $\mathbf{u}$ into an external wrench $\mathbf{w}$, namely,

$$\mathbf{w} = \begin{bmatrix} \mathbf{n} \\ \mathbf{f} \end{bmatrix} = \begin{bmatrix} \mathbf{K}_{11} & \mathbf{K}_{12} \\ \mathbf{K}_{12}^T & \mathbf{K}_{22} \end{bmatrix} \begin{bmatrix} \boldsymbol{\theta} \\ \boldsymbol{\sigma} \end{bmatrix} = \mathbf{K}_e \mathbf{u} \tag{2.33}$$

where $\mathbf{n}$ and $\mathbf{f}$ denote the external moment and force, $\boldsymbol{\theta}$ and $\boldsymbol{\sigma}$ the "small"-amplitude rotation and its translation counterpart, the latter being "small" when compared with the dimensions of the link in question. Moreover, the submatrices $\mathbf{K}_{11}$, $\mathbf{K}_{12}$ and $\mathbf{K}_{22}$ have units of Nm, N and N/m, respectively. Equation (2.33) is now rewritten in term of its individual blocks:

$$\mathbf{f} = \mathbf{K}_{11}\boldsymbol{\theta} + \mathbf{K}_{12}\boldsymbol{\sigma}, \quad \mathbf{n} = \mathbf{K}_{12}^T\boldsymbol{\theta} + \mathbf{K}_{22}\boldsymbol{\sigma} \tag{2.34}$$

Firstly, dimensionless parameters will be obtained by the normalization method proposed by Kövecses and Ebrahimi [130], as illustrated in the example below. Let $\mathbf{C}_\eta \mathbf{z}_\eta = \boldsymbol{\tau}_\eta$, $\eta = 1, \ldots, d$. A physically meaningful quadratic form $\mathbf{z}_\eta^T \mathbf{C}_\eta^T \mathbf{C}_\eta \mathbf{z}_\eta = \boldsymbol{\tau}_\eta^T \boldsymbol{\tau}_\eta$, defines a generalized force/torque ellipse in the linear space of the parameter set grouped in η. The eigenvalues of the matrix $\mathbf{C}_\eta^T \mathbf{C}_\eta$ are then used to define a natural coordinate system in parameter space η. The units of the parameter set η can be transferred into the base vectors of the coordinate system. Dimensionless parameters $\mathbf{s}_\eta$ can be obtained as

$$\mathbf{z}_\eta = \mathbf{V}_\eta \mathbf{s}_\eta \tag{2.35}$$

where $\mathbf{V}_\eta$ is an orthogonal matrix whose columns are the eigenvectors of $\mathbf{C}_\eta^T \mathbf{C}_\eta$. Moreover,

[6]The putative norm would involve additions, or comparisons, of quantities that carry different units.

$\mathbf{V}_\eta$ has the units of the parameter set η.

By resorting to this method, we have, for the force equation,

$$\begin{bmatrix} \boldsymbol{\theta} \\ \boldsymbol{\sigma} \end{bmatrix} = \begin{bmatrix} \mathbf{S}_\theta & \mathbf{O} \\ \mathbf{O} & \mathbf{S}_\sigma \end{bmatrix} \begin{bmatrix} \boldsymbol{\zeta}_\theta \\ \boldsymbol{\zeta}_\sigma \end{bmatrix} \tag{2.36}$$

while, for the moment equation,

$$\begin{bmatrix} \boldsymbol{\theta} \\ \boldsymbol{\sigma} \end{bmatrix} = \begin{bmatrix} \mathbf{H}_\theta & \mathbf{O} \\ \mathbf{O} & \mathbf{H}_\sigma \end{bmatrix} \begin{bmatrix} \boldsymbol{\eta}_\theta \\ \boldsymbol{\eta}_\sigma \end{bmatrix} \tag{2.37}$$

where $\boldsymbol{\zeta}_\theta$, $\boldsymbol{\zeta}_\sigma$, $\boldsymbol{\eta}_\theta$ and $\boldsymbol{\eta}_\sigma$ are dimensionless parameters, $\mathbf{S}_\theta$, $\mathbf{S}_\sigma$, $\mathbf{H}_\theta$ and $\mathbf{H}_\sigma$ being orthogonal matrices whose columns are the eigenvectors of $\mathbf{K}_{11}^T\mathbf{K}_{11}$, $\mathbf{K}_{12}^T\mathbf{K}_{12}$, $\mathbf{K}_{12}\mathbf{K}_{12}^T$ and $\mathbf{K}_{22}^T\mathbf{K}_{22}$, respectively. Substitution of eqs. (2.36) and (2.37) into eq. (2.34) leads to

$$\mathbf{n} = \begin{bmatrix} \mathbf{K}_{11} & \mathbf{K}_{12} \end{bmatrix} \begin{bmatrix} \mathbf{S}_\theta & \mathbf{O} \\ \mathbf{O} & \mathbf{S}_\sigma \end{bmatrix} \begin{bmatrix} \boldsymbol{\zeta}_\theta \\ \boldsymbol{\zeta}_\sigma \end{bmatrix} = \mathbf{G}_n\boldsymbol{\zeta} \tag{2.38a}$$

$$\mathbf{f} = \begin{bmatrix} \mathbf{K}_{12}^T & \mathbf{K}_{22} \end{bmatrix} \begin{bmatrix} \mathbf{H}_\theta & \mathbf{O} \\ \mathbf{O} & \mathbf{H}_\sigma \end{bmatrix} \begin{bmatrix} \boldsymbol{\eta}_\theta \\ \boldsymbol{\eta}_\sigma \end{bmatrix} = \mathbf{G}_f\boldsymbol{\eta} \tag{2.38b}$$

Matrices $\mathbf{G}_n^T\mathbf{G}_n$ and $\mathbf{G}_f^T\mathbf{G}_f$ have three mutually orthogonal eigenvectors corresponding to three positive eigenvalues. These eigenvalues characterize the distortions of the $||\mathbf{n}|| = 1$ (Nm) and $||\mathbf{f}|| = 1$ (N) unit spheres. Let the positive square roots of the eigenvalues of $\mathbf{G}_n^T\mathbf{G}_n$ and $\mathbf{G}_f^T\mathbf{G}_f$ be λ_i and μ_i, $i = 1, 2, 3$, respectively. The rotational and translational stiffness indices $\lambda_{\min}$ and $\mu_{\min}$ are the minima of $\lambda_i, i = 1, 2, 3$ and $\mu_i, i = 1, 2, 3$, respectively, i.e.,

$$\lambda_{\min} = \min_i \lambda_i, \quad \mu_{\min} = \min_i \mu_i \tag{2.39}$$

2.3.4 Numerical Results

The stiffness performance indices of the PMC are computed and plotted along the Adept test cycle, as introduced in this subsection. The rotational and translational square root eigenvalues λ_i and μ_i, $i = 1, \ldots, 3$, are plotted along the test cycle trajectory in Fig. 2.4. The rotational and translational stiffness indices $\lambda_{\min}$ and $\mu_{\min}$ are plotted in Fig. 2.5. These indices serve to identify the poor-stiffness postures along the trajectory, the smallest

stiffness index corresponding to the weakest stiffness posture. According to Fig. 2.5, the rotational and translational stiffness indices attain their minima at $t = 0.5$ s and $t = 0$ s, respectively, which means that at the "place" posture ($t = 0.5$ s), the rotational stiffness of the robot is the weakest. Meanwhile, at the "pick" posture, the translational stiffness performance of the robot is the weakest.

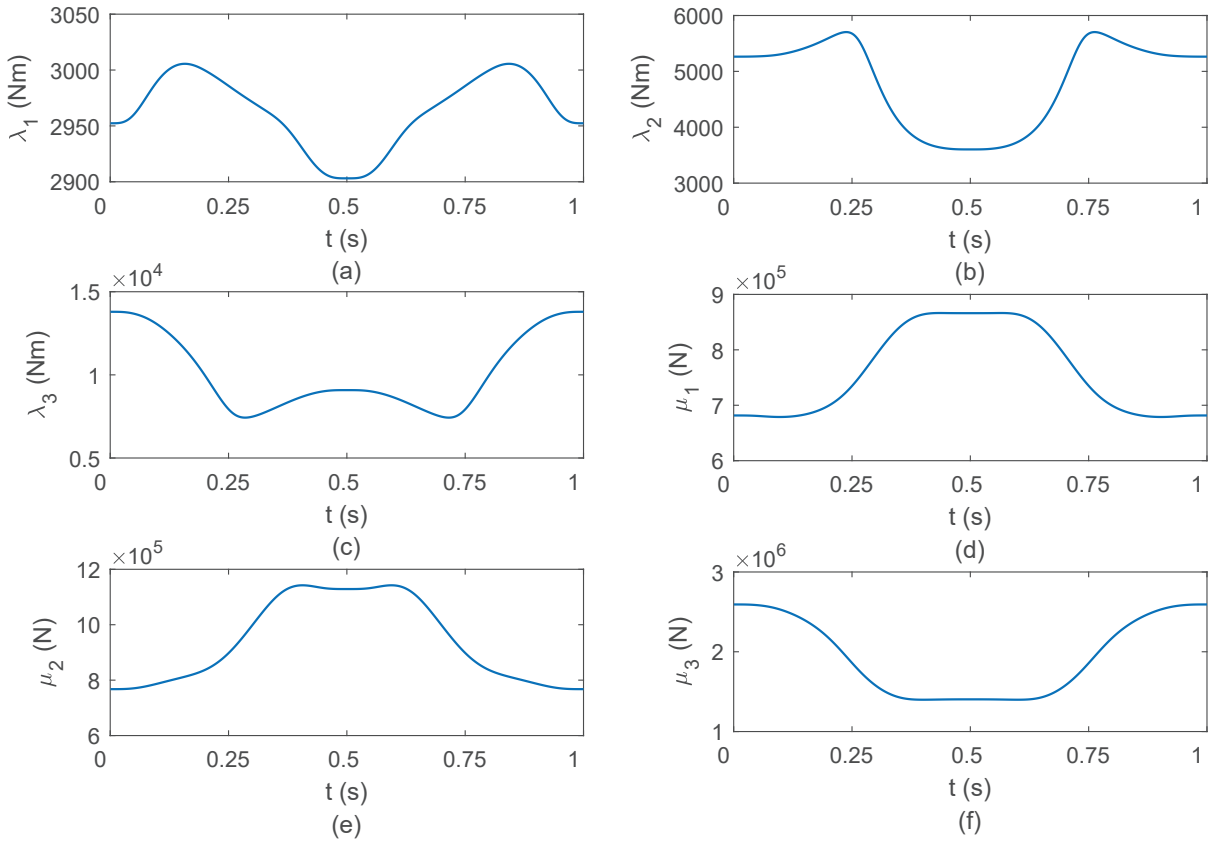

Fig. 2.4: The rotational and translational square root eigenvalues along the Adept test cycle trajectory

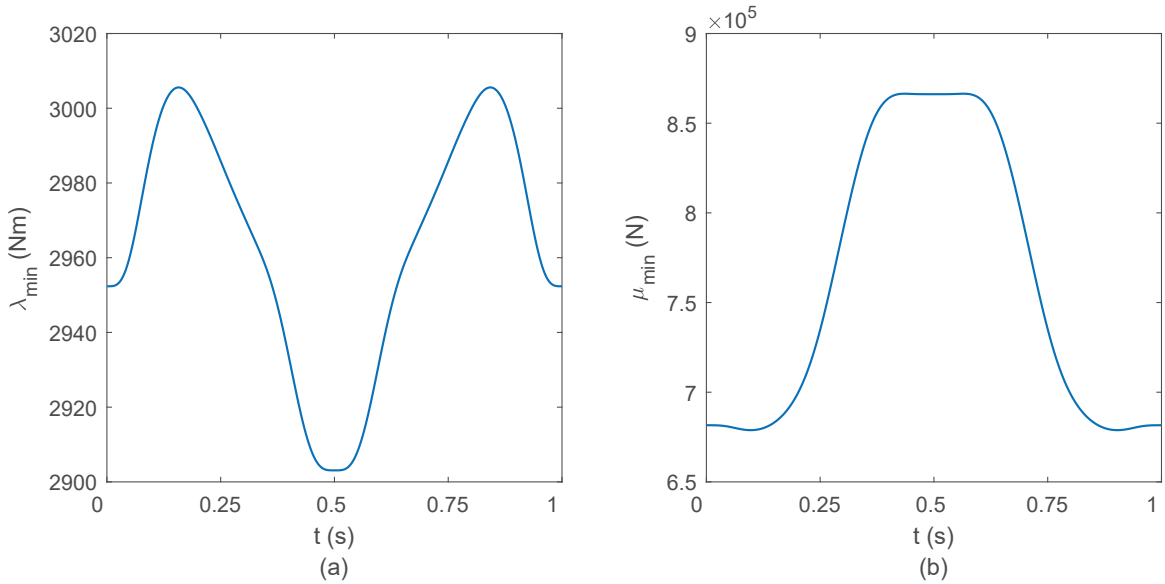

Fig. 2.5: The rotational and translational stiffness indices along the Adept test cycle trajectory

Chapter 3

Elastodynamics Analysis

3.1 Introduction

The elastodynamics analysis requires the stiffness and mass matrices of the robot. The stiffness matrix was obtained in Chapter 2. The mass matrix is calculated as the Hessian matrix of the kinetic energy generated by the flexible-component motion with the motors locked. The objective of elastodynamics analysis is to obtain the natural frequencies of the robot, which vary from posture to posture. To this end, the motors are assumed to be locked at every posture along the prescribed trajectory, while the inertia forces act as the loads on the elastostatic system thus resulting. This is a crucial step in the modelling because the natural frequencies should be placed far from the excitation frequency spectrum of a highly repetitive mechanical system to avoid resonance. The elastodynamics analysis of the PMC, as an illustrative example, is conducted. The natural frequency and the excitation spectrum are plotted along the test cycle of the pick-and-place operation. The natural frequency will be further applied to build the dynamics model of the PMC in Chapter 4.

3.2 Calculation of the Mass Matrix

In this section, the mass matrix of the PMC is calculated as the Hessian of the kinetic energy, generated by the flexible-component motion with the motors locked, with respect to the generalized velocities.

To formulate the kinetic energy, the generalized coordinates and the generalized velocities are defined below.

The independent generalized-coordinate array is defined as

$$\mathbf{q} = \begin{bmatrix} \mathbf{q}_m^T & \mathbf{q}_{11}^T & \mathbf{q}_{21}^T & \delta\gamma_1 & \delta\gamma_2 & \delta\beta_1 & \delta\beta_2 & \delta\alpha_1 & \delta\alpha_1 \end{bmatrix}^T \tag{3.1}$$

the corresponding generalized velocity array $\dot{\mathbf{q}}$ being

$$\dot{\mathbf{q}} = \begin{bmatrix} \dot{\mathbf{q}}_m^T & \dot{\mathbf{q}}_{11}^T & \dot{\mathbf{q}}_{21}^T & \delta\dot{\gamma}_1 & \delta\dot{\gamma}_2 & \delta\dot{\beta}_1 & \delta\dot{\beta}_2 & \delta\dot{\alpha}_1 & \delta\dot{\alpha}_1 \end{bmatrix}^T \tag{3.2}$$

Since all the motors are locked at a particular posture, the motion is generated by the deformation of the flexible components. As for the PMC, the kinetic energy is generated by the elastic motion of the arms, the forearms, the nuts and the Peppermill, as displayed in Fig. 2.2(a). Let $\dot{\mathbf{q}}_{J1}$, $\dot{\mathbf{q}}'_{J1}$, $\dot{\mathbf{q}}_{J2}$, $\dot{\mathbf{q}}_{nJ}$ and $\dot{\mathbf{q}}_m$ denote the corresponding twists defined at the points P_{J1}, P'_{J1}, P_{J2}, P'_{J2} and C, respectively, as shown in Fig. 2.2(b).

The schematic of the side view of limb J is shown in Fig. 3.1, where the points R_{cJ} and L_{cJ} are the COM of the arm and the forearm, respectively. Let $\dot{\mathbf{q}}_{aJ}$ and $\dot{\mathbf{q}}_{fJ}$ denote the twists defined at the points R_{cJ} and L_{cJ}, respectively.

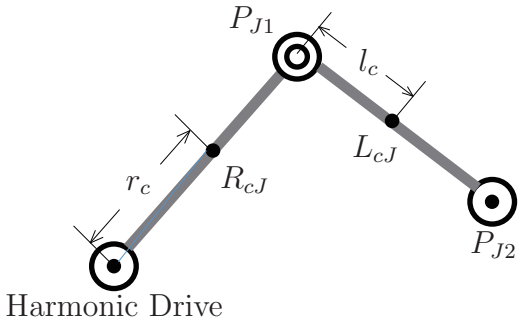

Fig. 3.1: Side view of limb J

The relationship between $\dot{\mathbf{q}}_{J1}$ and $\dot{\mathbf{q}}_{aJ}$ is

$$\dot{\mathbf{q}}_{aJ} = \mathbf{G}_{J1}\dot{\mathbf{q}}_{J1}, \quad \mathbf{G}_{J1} = \begin{bmatrix} \mathbf{1} & \mathbf{0} \\ -\mathbf{R}_J & \mathbf{1} \end{bmatrix} \tag{3.3}$$

where $\mathbf{R}_J = \text{CPM}\,(\mathbf{r}_{cJ})$, vector $\mathbf{r}_{cJ}$ stemming from P_{J1} and ending at R_{cJ}.

Similarly, the relationships among $\dot{\mathbf{q}}'_{J1}$, $\dot{\mathbf{q}}_{J2}$ and $\dot{\mathbf{q}}'_{fJ}$ are readily derived:

$$\dot{\mathbf{q}}_{fJ} = \mathbf{G}_{J2}\dot{\mathbf{q}}'_{J1} + \mathbf{G}_{J3}\dot{\mathbf{q}}_{J2}, \quad \mathbf{G}_{J2} = \begin{bmatrix} \mathbf{1} & \mathbf{0} \\ -\mathbf{L}_J & \mathbf{1} \end{bmatrix}, \quad \mathbf{G}_{J3} = \begin{bmatrix} \mathbf{1} & \mathbf{0} \\ -\mathbf{L}'_J & \mathbf{1} \end{bmatrix} \tag{3.4}$$

where $\mathbf{L}_J = \text{CPM}\ (\mathbf{l}_{cJ})$, $\mathbf{L}'_J = \text{CPM}\ (\mathbf{l}'_{cJ})$, vector $\mathbf{l}_{cJ}$ stemming from P'_{J1} and ending at L_{cJ}, vector $\mathbf{l}'_{cJ}$ stemming from P_{J2} and ending at L_{cJ}. The *inertia dyad* was introduced by von Mises [131], given by

$$\mathbf{M} = \begin{bmatrix} \mathbf{I}_C & \mathbf{O} \\ \mathbf{O} & m\mathbf{1} \end{bmatrix}$$

where m and $\mathbf{I}_C$ are the mass and the moment of inertia, defined at the centre of mass of a rigid body, $\mathbf{O}$ and $\mathbf{1}$ the 3×3 zero and identity matrices.

The kinetic energy of the arm J is

$$T_J^A = \frac{1}{2}\dot{\mathbf{q}}_{aJ}^T \mathbf{M}^{AJ} \dot{\mathbf{q}}_{aJ}, \quad \mathbf{M}^{AJ} = \begin{bmatrix} \mathbf{I}^{AJ} & \mathbf{O} \\ \mathbf{O} & m^{AJ}\mathbf{1} \end{bmatrix} \tag{3.5}$$

where $\mathbf{M}^{AJ}$, $\mathbf{I}^{AJ}$ and m^{AJ} are the inertia dyad, inertia tensor and mass of the arm J, respectively. Similarly, the kinetic energy of the forearm, the nut and the Peppermill are further introduced:

$$T_J^F = \frac{1}{2}\dot{\mathbf{q}}_{fJ}^T \mathbf{M}^{FJ} \dot{\mathbf{q}}_{fJ}, \quad T_J^N = \frac{1}{2}\dot{\mathbf{q}}_{nJ}^T \mathbf{M}^{NJ} \dot{\mathbf{q}}_{nJ}, \quad T^P = \frac{1}{2}\dot{\mathbf{q}}_m^T \mathbf{M}^P \dot{\mathbf{q}}_m \tag{3.6}$$

where $\mathbf{M}^{FJ}$, $\mathbf{M}^{NJ}$ and $\mathbf{M}^P$ are the inertia dyads of the forearm and the nut of limb J, and the Peppermill, respectively, given by

$$\mathbf{M}^{FJ} = \begin{bmatrix} \mathbf{I}^{FJ} & \mathbf{O} \\ \mathbf{O} & m^{FJ}\mathbf{1} \end{bmatrix}, \quad \mathbf{M}^{NJ} = \begin{bmatrix} \mathbf{I}^{NJ} & \mathbf{O} \\ \mathbf{O} & m^{NJ}\mathbf{1} \end{bmatrix}, \quad \mathbf{M}^P = \begin{bmatrix} \mathbf{I}^P & \mathbf{O} \\ \mathbf{O} & m^P\mathbf{1} \end{bmatrix} \tag{3.7}$$

The kinetic energy of the PMC is the sum of the kinetic energies, generated by the arms, the forearms, the nuts and the Peppermill:

$$T_e = \sum_{J=1}^{2} (T_J^A + T_J^F + T_J^N) + T^P \tag{3.8}$$

Substitution of eqs. (3.3–3.6) into eq. (3.8), the kinetic energy of the PMC becomes,

$$T_e = \frac{1}{2}\sum_{J=1}^{2}[(\mathbf{G}_{J1}\dot{\mathbf{q}}_{J1})^T\mathbf{M}^{AJ}(\mathbf{G}_{J1}\dot{\mathbf{q}}_{J1}) + (\mathbf{G}_{J2}\dot{\mathbf{q}}'_{J1} + \mathbf{G}_{J3}\dot{\mathbf{q}}_{J2})^T\mathbf{M}^{FJ}(\mathbf{G}_{J2}\dot{\mathbf{q}}'_{J1} + \mathbf{G}_{J3}\dot{\mathbf{q}}_{J2}) + \dot{\mathbf{q}}_{nJ}^T\mathbf{M}^{NJ}\dot{\mathbf{q}}_{nJ}] + \frac{1}{2}\dot{\mathbf{q}}_m^T\mathbf{M}^P\dot{\mathbf{q}}_m \tag{3.9}$$

Moreover, differentiation of the two sides of eq. (2.11), the relationship between $\dot{\mathbf{q}}_{J1}$ and $\dot{\mathbf{q}}'_{J1}$ is obtained:

$$\dot{\mathbf{q}}'_{J1} = \dot{\mathbf{q}}_{J1} + \delta\dot{\beta}_J\mathbf{s}_J \tag{3.10}$$

By resorting to eqs. (2.12) and (2.13), the relationships between $\dot{\mathbf{q}}_{J2}$ ($\dot{\mathbf{q}}_{nJ}$) and its counterpart $\dot{\mathbf{q}}_{nJ}$ ($\dot{\mathbf{q}}_m$) are readily derived:

$$\dot{\mathbf{q}}_{J2} = \dot{\mathbf{q}}_{nJ} + \delta\dot{\gamma}_J\mathbf{s}_J, \quad \dot{\mathbf{q}}_{nJ} = \mathbf{G}_J\dot{\mathbf{q}}_m + \delta\dot{\alpha}_J\mathbf{s}_{HJ} \tag{3.11}$$

Substitution of eqs. (3.10) and (3.11) into eq. (3.9), leads to

$$\begin{aligned} T_e = \frac{1}{2}\sum_{J=1}^{2}[&(\mathbf{G}_{J1}\dot{\mathbf{q}}_{J1})^T\mathbf{M}^{AJ}(\mathbf{G}_{J1}\dot{\mathbf{q}}_{J1}) + \mathbf{G}_{J2}(\dot{\mathbf{q}}_{J1} + \delta\dot{\beta}_J\mathbf{s}_J) \\ &+ \mathbf{G}_{J3}(\dot{\mathbf{q}}_{nJ} + \delta\dot{\gamma}_J\mathbf{s}_J))^T\mathbf{M}^{FJ}(\mathbf{G}_{J2}(\dot{\mathbf{q}}_{J1} + \delta\dot{\beta}_J\mathbf{s}_J) + \mathbf{G}_{J3}(\dot{\mathbf{q}}_{nJ} + \delta\dot{\gamma}_J\mathbf{s}_J) \\ &+ (\mathbf{G}_J\dot{\mathbf{q}}_m + \delta\dot{\alpha}_J\mathbf{s}_{HJ})^T\mathbf{M}^{NJ}(\mathbf{G}_J\dot{\mathbf{q}}_m + \delta\dot{\alpha}_J\mathbf{s}_{HJ})] + \frac{1}{2}\dot{\mathbf{q}}_m^T\mathbf{M}^P\dot{\mathbf{q}}_m \end{aligned} \tag{3.12}$$

The generalized mass matrix of the PMC is the Hessian matrix of T_e with respect to the generalized velocities. This matrix maps the generalized velocity array into the generalized momentum array:

$$\begin{bmatrix} \mathbf{p}_m \\ \mathbf{p}_1 \\ \mathbf{p}_2 \\ p_{12} \\ p_{22} \\ p_{11} \\ p_{21} \\ p_{13} \\ p_{23} \end{bmatrix} = \begin{bmatrix} \mathbf{M}_{11} & \mathbf{M}_{12} & \mathbf{M}_{13} & \mathbf{m}_{14} & \mathbf{m}_{15} & \mathbf{m}_{16} & \mathbf{m}_{17} & \mathbf{m}_{18} & \mathbf{m}_{19} \\ \mathbf{M}_{12}^T & \mathbf{M}_{22} & \mathbf{O} & \mathbf{m}_{24} & \mathbf{0} & \mathbf{m}_{26} & \mathbf{0} & \mathbf{m}_{28} & \mathbf{0} \\ \mathbf{M}_{13}^T & \mathbf{O} & \mathbf{M}_{33} & \mathbf{0} & \mathbf{m}_{35} & \mathbf{0} & \mathbf{m}_{37} & \mathbf{0} & \mathbf{m}_{39} \\ \mathbf{m}_{14}^T & \mathbf{m}_{24}^T & \mathbf{0}^T & m_{44} & 0 & m_{46} & 0 & m_{48} & 0 \\ \mathbf{m}_{15}^T & \mathbf{0}^T & \mathbf{m}_{35}^T & 0 & m_{55} & 0 & m_{57} & 0 & m_{59} \\ \mathbf{m}_{16}^T & \mathbf{m}_{26}^T & \mathbf{0}^T & m_{46} & 0 & m_{66} & 0 & m_{68} & 0 \\ \mathbf{m}_{17}^T & \mathbf{0}^T & \mathbf{m}_{37}^T & 0 & m_{57} & 0 & m_{77} & 0 & m_{79} \\ \mathbf{m}_{18}^T & \mathbf{m}_{28}^T & \mathbf{0}^T & m_{48} & 0 & m_{68} & 0 & m_{88} & 0 \\ \mathbf{m}_{19}^T & \mathbf{0}^T & \mathbf{m}_{39}^T & 0 & m_{59} & 0 & m_{79} & 0 & m_{99} \end{bmatrix} \begin{bmatrix} \dot{\mathbf{q}}_m \\ \dot{\mathbf{q}}_{11} \\ \dot{\mathbf{q}}_{21} \\ \delta\dot{\gamma}_1 \\ \delta\dot{\gamma}_2 \\ \delta\dot{\beta}_1 \\ \delta\dot{\beta}_2 \\ \delta\dot{\alpha}_1 \\ \delta\dot{\alpha}_1 \end{bmatrix} \tag{3.13}$$

where $\mathbf{p}_m$, $\mathbf{p}_J$, p_{J1}, p_{J2} and p_{J3} are, respectively, the six-dimensional generalized momenta defined are C, P_{J1} and the generalized angular momenta about the R_{J1}, R_{J2} and H_J joints, $\mathbf{O}$ the 6×6 zero matrix, $\mathbf{0}$ the six-dimensional zero vector, the non-zero blocks of the mass matrix being defined below:

$$\begin{aligned}
&\mathbf{M}_{11} = \mathbf{G}_1^T\mathbf{G}_{13}^T\mathbf{M}^{F1}\mathbf{G}_{13}\mathbf{G}_1 + \mathbf{G}_1^T\mathbf{M}^{N1}\mathbf{G}_1 + \mathbf{G}_2^T\mathbf{G}_{23}^T\mathbf{M}^{F2}\mathbf{G}_{23}\mathbf{G}_2 + \mathbf{G}_2^T\mathbf{M}^{N2}\mathbf{G}_2 + \mathbf{M}^P \\
&\mathbf{M}_{12} = \mathbf{G}_1^T\mathbf{G}_{13}^T\mathbf{M}^{F1}\mathbf{G}_{12}, \quad \mathbf{M}_{13} = \mathbf{G}_2^T\mathbf{G}_{23}^T\mathbf{M}^{F2}\mathbf{G}_{22}, \quad \mathbf{m}_{14} = \mathbf{G}_1^T\mathbf{G}_{13}^T\mathbf{M}^{F1}\mathbf{G}_{13}\mathbf{s}_1, \\
&\mathbf{m}_{15} = \mathbf{G}_2^T\mathbf{G}_{23}^T\mathbf{M}^{F2}\mathbf{G}_{23}\mathbf{s}_2, \quad \mathbf{m}_{16} = \mathbf{G}_1^T\mathbf{G}_{13}^T\mathbf{M}^{F1}\mathbf{G}_{12}\mathbf{s}_1, \quad \mathbf{m}_{17} = \mathbf{G}_2^T\mathbf{G}_{23}^T\mathbf{M}^{F2}\mathbf{G}_{22}\mathbf{s}_2, \\
&\mathbf{m}_{18} = \mathbf{G}_1^T\mathbf{G}_{13}^T\mathbf{M}^{F1}\mathbf{G}_{13}\mathbf{s}_{H1} + \mathbf{G}_1^T\mathbf{M}^{N1}\mathbf{s}_{H1}, \quad \mathbf{m}_{19} = \mathbf{G}_2^T\mathbf{G}_{23}^T\mathbf{M}^{F2}\mathbf{G}_{23}\mathbf{s}_{H2} + \mathbf{G}_2^T\mathbf{M}^{N2}\mathbf{s}_{H2}, \\
&\mathbf{M}_{22} = \mathbf{G}_{11}^T\mathbf{M}^{A1}\mathbf{G}_{11} + \mathbf{G}_{12}^T\mathbf{M}^{F1}\mathbf{G}_{12}, \quad \mathbf{m}_{24} = \mathbf{G}_{12}^T\mathbf{M}^{F1}\mathbf{G}_{13}\mathbf{s}_1, \\
&\mathbf{m}_{26} = \mathbf{G}_{12}^T\mathbf{M}^{F1}\mathbf{G}_{12}\mathbf{s}_1, \quad \mathbf{m}_{28} = \mathbf{G}_{12}^T\mathbf{M}^{F1}\mathbf{G}_{13}\mathbf{s}_{H1}, \quad \mathbf{M}_{33} = \mathbf{G}_{21}^T\mathbf{M}^{A2}\mathbf{G}_{21} + \mathbf{G}_{22}^T\mathbf{M}^{F2}\mathbf{G}_{22}, \\
&\mathbf{m}_{35} = \mathbf{G}_{22}^T\mathbf{M}^{F2}\mathbf{G}_{23}\mathbf{s}_2, \quad \mathbf{m}_{37} = \mathbf{G}_{22}^T\mathbf{M}^{F2}\mathbf{G}_{22}\mathbf{s}_2, \quad \mathbf{m}_{39} = \mathbf{G}_{22}^T\mathbf{M}^{F2}\mathbf{G}_{23}\mathbf{s}_{H2}, \\
&m_{44} = \mathbf{s}_1^T\mathbf{G}_{13}^T\mathbf{M}^{F1}\mathbf{G}_{13}\mathbf{s}_1, \quad m_{46} = \mathbf{s}_1^T\mathbf{G}_{13}^T\mathbf{M}^{F1}\mathbf{G}_{12}\mathbf{s}_1, \quad m_{48} = \mathbf{s}_{H1}^T\mathbf{G}_{13}^T\mathbf{M}^{F1}\mathbf{G}_{13}\mathbf{s}_1, \\
&m_{55} = \mathbf{s}_2^T\mathbf{G}_{23}^T\mathbf{M}^{F2}\mathbf{G}_{23}\mathbf{s}_2, \quad m_{57} = \mathbf{s}_2^T\mathbf{G}_{23}^T\mathbf{M}^{F2}\mathbf{G}_{22}\mathbf{s}_2, \quad m_{59} = \mathbf{s}_{H2}^T\mathbf{G}_{23}^T\mathbf{M}^{F2}\mathbf{G}_{23}\mathbf{s}_2, \\
&m_{66} = \mathbf{s}_1^T\mathbf{G}_{12}^T\mathbf{M}^{F1}\mathbf{G}_{12}\mathbf{s}_1, \quad m_{68} = \mathbf{s}_{H1}^T\mathbf{G}_{13}^T\mathbf{M}^{F1}\mathbf{G}_{12}\mathbf{s}_1, \quad m_{77} = \mathbf{s}_2^T\mathbf{G}_{22}^T\mathbf{M}^{F2}\mathbf{G}_{22}\mathbf{s}_2, \\
&m_{79} = \mathbf{s}_{H2}^T\mathbf{G}_{23}^T\mathbf{M}^{F2}\mathbf{G}_{22}\mathbf{s}_2, \quad m_{88} = \mathbf{s}_{H1}^T\mathbf{G}_{13}^T\mathbf{M}^{F1}\mathbf{G}_{13}\mathbf{s}_{H1} + \mathbf{s}_{H1}^T\mathbf{M}^{N1}\mathbf{s}_{H1}, \\
&m_{99} = \mathbf{s}_{H2}^T\mathbf{G}_{23}^T\mathbf{M}^{F2}\mathbf{G}_{23}\mathbf{s}_{H2} + \mathbf{s}_{H2}^T\mathbf{M}^{N2}\mathbf{s}_{H2}
\end{aligned} \tag{3.14}$$

R_{J1}, R_{J2} and H_J being passive joints, the angular momentum acting on them vanishes,

i.e., $p_{ij} = 0$. The Cartesian mass matrix $\mathbf{M}_e \in \mathbb{R}^{6\times6}$, mapping the twist of the Peppermill into the momentum applied onto it, namely, $\mathbf{p}_J = \mathbf{0}$. From eq. (3.13), the Cartesian mass matrix is obtained:

$$\mathbf{M}_e = \mathbf{M}_{11} - \mathbf{M}_{b1}\mathbf{M}_{b2}^{-1}\mathbf{M}_{b1}^T \tag{3.15}$$

where

$$\mathbf{M}_{b1} = \begin{bmatrix} \mathbf{M}_{12}^T \\ \mathbf{M}_{13}^T \\ \mathbf{m}_{14}^T \\ \mathbf{m}_{15}^T \\ \mathbf{m}_{16}^T \\ \mathbf{m}_{17}^T \\ \mathbf{m}_{18}^T \\ \mathbf{m}_{19}^T \end{bmatrix}^T, \quad \mathbf{M}_{b2} = \begin{bmatrix} \mathbf{M}_{22} & \mathbf{O} & \mathbf{m}_{24} & \mathbf{0} & \mathbf{m}_{26} & \mathbf{0} & \mathbf{m}_{28} & \mathbf{0} \\ \mathbf{O} & \mathbf{M}_{33} & \mathbf{0} & \mathbf{m}_{35} & \mathbf{0} & \mathbf{m}_{37} & \mathbf{0} & \mathbf{m}_{39} \\ \mathbf{m}_{24}^T & \mathbf{0}^T & m_{44} & 0 & m_{46} & 0 & m_{48} & 0 \\ \mathbf{0}^T & \mathbf{m}_{35}^T & 0 & m_{55} & 0 & m_{57} & 0 & m_{59} \\ \mathbf{m}_{26}^T & \mathbf{0}^T & m_{46} & 0 & m_{66} & 0 & m_{68} & 0 \\ \mathbf{0}^T & \mathbf{m}_{37}^T & 0 & m_{57} & 0 & m_{77} & 0 & m_{79} \\ \mathbf{m}_{28}^T & \mathbf{0}^T & m_{48} & 0 & m_{68} & 0 & m_{88} & 0 \\ \mathbf{0}^T & \mathbf{m}_{39}^T & 0 & m_{59} & 0 & m_{79} & 0 & m_{99} \end{bmatrix} \tag{3.16}$$

3.3 Fourier Analysis

In this section, the excitation frequency spectrum is obtained by Fourier analysis, which will be used to compare with the natural frequency to analyze the existence of the resonance.

3.3.1 Methodology

It is essential to obtain the frequency spectrum of a highly repetitive mechanical system because the natural frequencies should be placed far from it to avoid resonance. The frequency spectrum is obtained by means of Fourier analysis [132].

A periodic function $f(t)$ with a fundamental frequency ω can be represented as:

$$f(t) = \frac{a_0}{2} + \sum_{i=1}^{\infty} a_i \cos(i\omega t) + \sum_{i=1}^{\infty} b_i \sin(i\omega t)$$

where

$$a_0 = \frac{1}{T}\int_{-T/2}^{T/2} f(t)dt,\ a_i = \frac{1}{T}\int_{-T/2}^{T/2} f(t)\cos(i\omega t)dt,\ b_i = \frac{1}{T}\int_{-T/2}^{T/2} f(t)\sin(i\omega t)dt$$

in which i and T are the harmonic index and the period of function $f(t)$, respectively.

In this case, the periodic functions are the trajectory functions of the MP, namely, the translations along the x-, the y- and the z-axes along with the rotation about the z-axis. The trajectory introduced in Subsection 1.1, is depicted in Fig. 3.2.

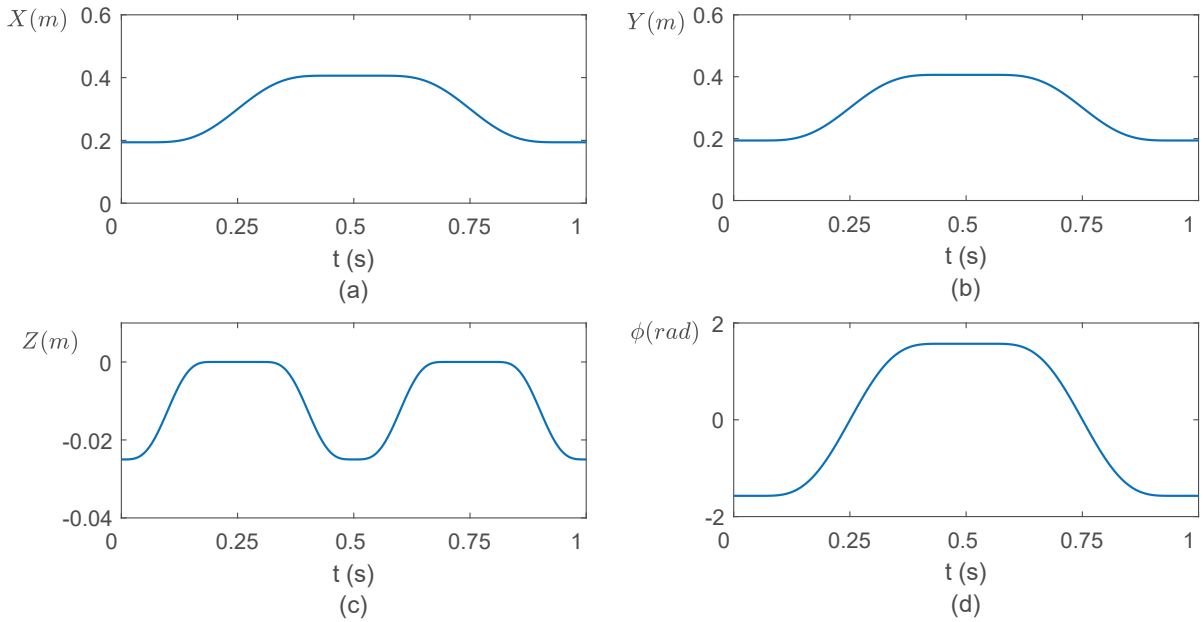

Fig. 3.2: The test trajectory plots: (a) the translation along the x-axis, (b) the translation along the y-axis, (c) the translation along the z-axis , and (d) the rotation about the z-axis

3.3.2 Numerical Results

In order to obtain the excitation frequency spectrum and find the highest operation speed whose excitation frequency spectrum is under the first natural frequency of the PMC, the distribution of normalized parameters $|\bar{a}_{xn}|$, $|\bar{a}_{yn}|$, $|\bar{a}_{zn}|$ and $|\bar{a}_{\phi n}|$ with respect to the frequency f when the speed is 1 and 2 cycles/s are plotted in the Figs. 3.3 and 3.4, respectively.

3.4 Modal Analysis

In this section, the modal analysis is conducted to obtain the natural frequencies of the PMC.

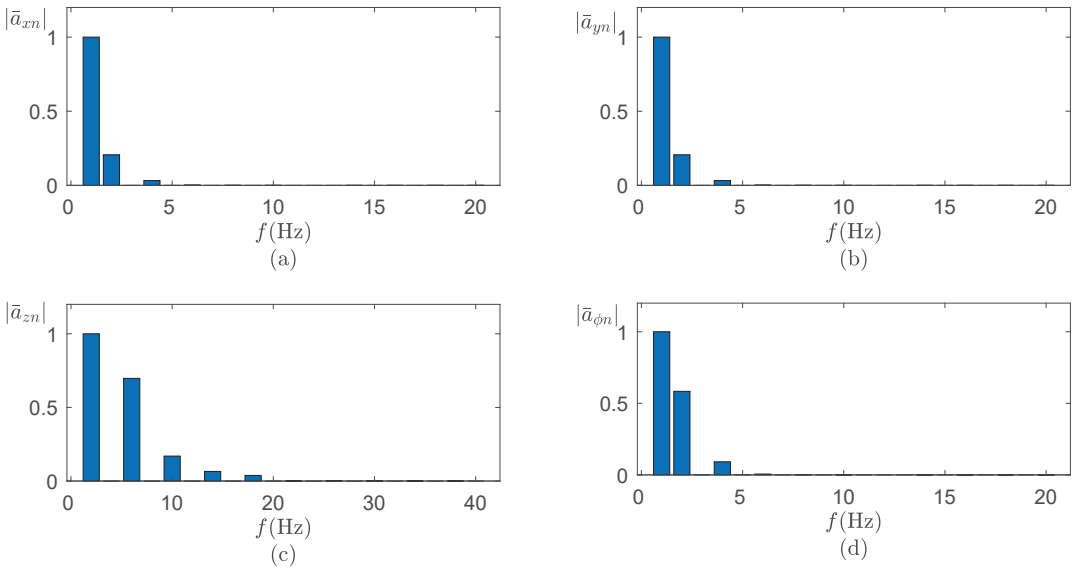

Fig. 3.3: Amplitudes of the harmonics of the four independent motions vs. frequency (1 cycle/s): (a) translation along the x-axis; (b) translation along the y-axis; (c) translation along the z-axis; (d) rotation about the z-axis

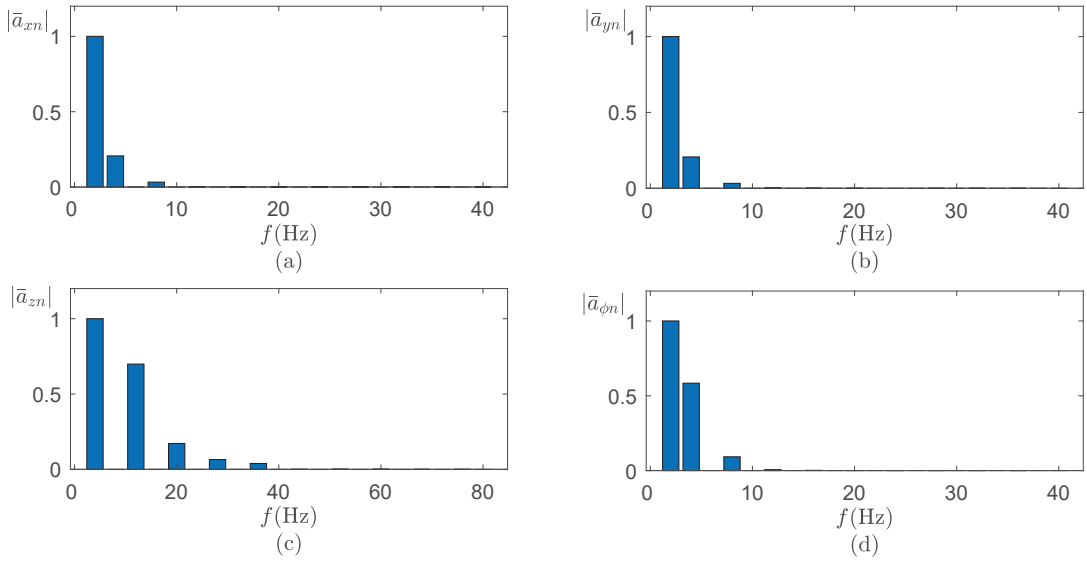

Fig. 3.4: Amplitudes of the harmonics of the four independent motions vs. frequency (2 cycles/s): (a) translation along the x-axis; (b) translation along the y-axis; (c) translation along the z-axis; (d) rotation about the z-axis

3.4.1 Methodology

Modal analysis calls for the stiffness and mass matrices, obtained above. The mathematical model of the robot, at an equilibrium posture, is

$$\mathbf{M}\ddot{\mathbf{x}} + \mathbf{K}\dot{\mathbf{x}} = \mathbf{0} \tag{3.17}$$

where $\mathbf{M}$ and $\mathbf{K}$ are the mass and stiffness matrices, while $\mathbf{x}$ is the SAD screw. To obtain the natural frequencies of the system, the well-known *dynamic-matrix* is recalled. One has

$$(\lambda\mathbf{M} + \mathbf{K})\mathbf{u} = \mathbf{0} \tag{3.18}$$

where λ and $\mathbf{u}$ are, respectively, the eigenvalue and the corresponding eigenvector. Therefore, by computing the eigenvalues of the dynamic matrix $\mathbf{M}^{-1}\mathbf{K}$, $-\omega^2$ is obtained, with ω being an eigenfrequency. It should be noted, however, that the last three components of the six-dimensional eigenvector $\mathbf{u}$ carry units of length, while the first three are nondimensional.

3.4.2 Numerical Results

Now we let the PMC conduct the pick-and-place operation along the Adept test cycle and evaluate the first natural frequency, as displayed in Fig. 3.5. Only the first natural frequency is shown, as the subsequent frequencies are well above the first, and, hence, are not significant.

The minimum value of the first natural frequency is 52.5 Hz. According to Fig. 3.4, the excitation frequency spectrum of an operation at 2 cycles/s, we can find that the translation along the x- and y-axis as well as the rotation about the z-axis are obviously on the safe side. The translation along the z-axis has already reached its limit; hence, resonance will ensue if the operation speed is 3 cycles/s.

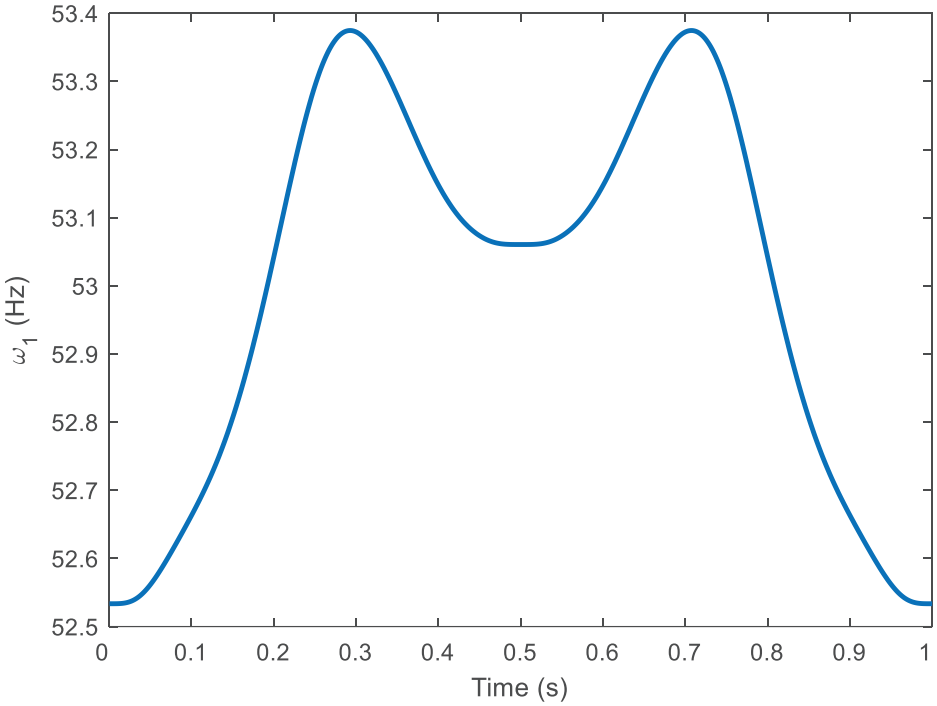

Fig. 3.5: The evolution of the first natural frequency of the PMC along the test trajectory

Chapter 4

Dynamics Modelling

4.1 Introduction

After the derivation of the elastodynamics model in the previous section, the pertinent dynamics models are formulated as described in this chapter. A rigid-link conservative dynamics model of the PMC is first built. Then, process noise, measurement noise, and parameter uncertainty are taken into consideration to make the model realistic. In the end, the first natural frequency of the PMC obtained from the elastodynamics analysis is applied to build the dynamics model of the virtual flexible motor shaft of the PMC.

4.2 Rigid-link Conservative Dynamics Model

In this section, a rigid-link conservative dynamics model of the PMC is built, which is used to design the control schemes in Chapter 5. The dynamics of the original-version PMC was reported by Karimi Eskandary and Angeles [133] and Karimi Eskandary et al. [134]. The current version of the PMC is shown in Fig. 4.1. Compared with the original-version, the current-version robot structure has six more rigid bodies, as described below. Each screw is connected to the belt through a pulley. The robot has four pulleys in total, one for each screw. The belt-pulley transmission system is connected to a harmonic drive through a sliding base in each limb. The four pulleys and the two sliding bases are considered in the model.

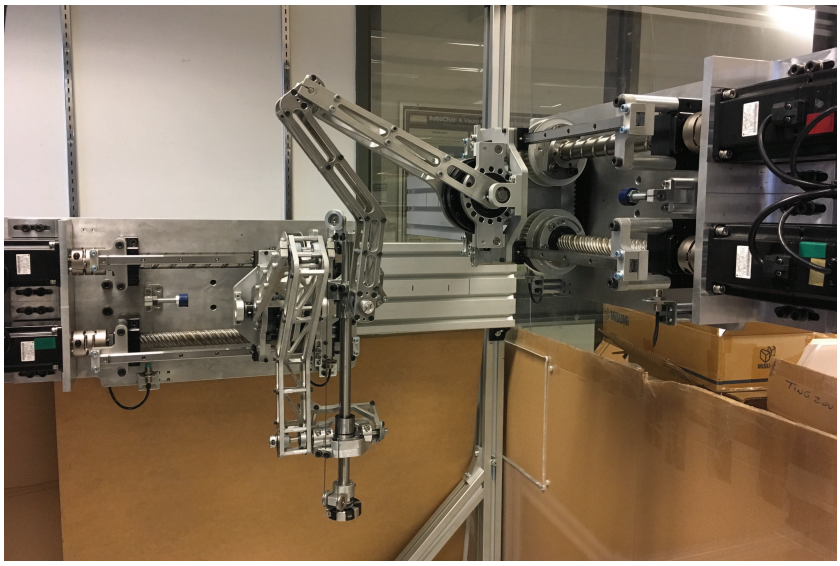

Fig. 4.1: Current versoin of the PMC

The dynamics of the current-version PMC is given by

$$\boldsymbol{\tau} = \mathbf{I}\ddot{\boldsymbol{\psi}} + \mathbf{C}\dot{\boldsymbol{\psi}} - \boldsymbol{\gamma} \tag{4.1}$$

with

$$\begin{aligned}
&\boldsymbol{\tau} \equiv \begin{bmatrix} \tau_{1R} & \tau_{1L} & \tau_{2R} & \tau_{2L} \end{bmatrix}^T, \quad \boldsymbol{\psi} \equiv \begin{bmatrix} \psi_{1R} & \psi_{1L} & \psi_{2R} & \psi_{2L} \end{bmatrix}^T, \quad \mathbf{I} \equiv \sum_{i=1}^{17} {\mathbf{T}_i}^T \mathbf{M}_i \mathbf{T}_i, \\
&\mathbf{C} \equiv \sum_{i=1}^{17} ({\mathbf{T}_i}^T \mathbf{M}_i \dot{\mathbf{T}}_i + {\mathbf{T}_i}^T \mathbf{W}_i \mathbf{M}_i \mathbf{T}_i), \quad \boldsymbol{\gamma} \equiv \sum_{i=1}^{17} {\mathbf{T}_i}^T {\mathbf{w}_i}^G, \quad \mathbf{M}_i \equiv \begin{bmatrix} \mathbf{I}_i & \mathbf{O} \\ \mathbf{O} & m_i \mathbf{1} \end{bmatrix}, \\
&\mathbf{W}_i \equiv \begin{bmatrix} \boldsymbol{\Omega}_i & \mathbf{O} \\ \mathbf{O} & \mathbf{O} \end{bmatrix}, \quad \mathbf{T}_i \equiv \frac{\partial \mathbf{t}_i}{\partial \dot{\boldsymbol{\psi}}}
\end{aligned} \tag{4.2}$$

where $\mathbf{1}$ and $\mathbf{O}$ are the 3×3 identity and zero matrices; $\boldsymbol{\tau}$ the four-dimensional motor-torque array; $\boldsymbol{\gamma}$ the four-dimensional generalized gravity-force array, which appears with a negative sign because gravity opposes the actuator torques; $\boldsymbol{\psi}$ the four-dimensional motor angular displacement array; $\mathbf{T}_i$ the twist-shaping matrix, mapping the joint rates of the motors into the twist vector $\mathbf{t}_i$ of the ith body [135]; $\mathbf{I}_i$ the inertia tensor defined at the centre of mass (COM) of the ith body and m_i the mass of the ith body. Moreover, $\mathbf{w}_i^G$ is

the gravitational wrench acting on the ith body, while $\mathbf{\Omega}_i$ is the angular-velocity matrix, defined as the CPM of the angular-velocity vector $\boldsymbol{\omega}_i$. Furthermore, $\mathbf{t}_i$ and $\mathbf{w}_i$ are defined as,

$$\mathbf{t}_i \equiv \begin{bmatrix} \boldsymbol{\omega}_i \\ \mathbf{v}_i \end{bmatrix}, \quad \mathbf{w}_i \equiv \begin{bmatrix} \mathbf{n}_i \\ \mathbf{f}_i \end{bmatrix} \tag{4.3}$$

where $\boldsymbol{\omega}_i$ and $\mathbf{v}_i$ are the angular velocity and the velocity of the COM of the ith body, while $\mathbf{n}_i$ and $\mathbf{f}_i$ are the moment and the force acting on the ith body. As well, $\mathbf{f}_i$ acts at the COM of the ith body. The six-dimensional twist vectors are

$$\mathbf{t}_{sL1} = \begin{bmatrix} \dot{\psi}_{1L} \\ 0 \\ 0 \\ 0 \\ 0 \\ 0 \end{bmatrix}, \quad \mathbf{t}_{sR1} = \begin{bmatrix} \dot{\psi}_{1R} \\ 0 \\ 0 \\ 0 \\ 0 \\ 0 \end{bmatrix}, \quad \mathbf{t}_{sL2} = \begin{bmatrix} 0 \\ \dot{\psi}_{2L} \\ 0 \\ 0 \\ 0 \\ 0 \end{bmatrix}, \quad \mathbf{t}_{sR2} = \begin{bmatrix} 0 \\ \dot{\psi}_{2R} \\ 0 \\ 0 \\ 0 \\ 0 \end{bmatrix}, \quad \mathbf{t}_{pU1} = \begin{bmatrix} \dot{\psi}_{1L} \\ 0 \\ 0 \\ \dot{u}_1 \\ 0 \\ 0 \end{bmatrix},$$

$$\mathbf{t}_{pD1} = \begin{bmatrix} \dot{\psi}_{1R} \\ 0 \\ 0 \\ \dot{u}_1 \\ 0 \\ 0 \end{bmatrix}, \quad \mathbf{t}_{pU2} = \begin{bmatrix} 0 \\ \dot{\psi}_{2L} \\ 0 \\ 0 \\ \dot{u}_2 \\ 0 \end{bmatrix}, \quad \mathbf{t}_{pD2} = \begin{bmatrix} 0 \\ \dot{\psi}_{2R} \\ 0 \\ 0 \\ \dot{u}_2 \\ 0 \end{bmatrix}, \quad \mathbf{t}_{b1} = \begin{bmatrix} 0 \\ 0 \\ 0 \\ \dot{u}_1 \\ 0 \\ 0 \end{bmatrix}, \quad \mathbf{t}_{b2} = \begin{bmatrix} 0 \\ 0 \\ 0 \\ 0 \\ \dot{u}_2 \\ 0 \end{bmatrix},$$

$$\mathbf{t}_{a1} = \begin{bmatrix} \dot{\theta}_1 \\ 0 \\ 0 \\ \dot{u}_1 \\ -r_a\dot{\theta}_1 \sin(\theta_1) \\ r_a\dot{\theta}_1 \cos(\theta_1) \end{bmatrix}, \quad \mathbf{t}_{a2} = \begin{bmatrix} 0 \\ \dot{\theta}_2 \\ 0 \\ -r_a\dot{\theta}_2 \sin(\theta_2) \\ \dot{u}_2 \\ -r_a\dot{\theta}_2 \cos(\theta_2) \end{bmatrix}, \quad \mathbf{t}_{n1} = \begin{bmatrix} 0 \\ 0 \\ 0 \\ \dot{u}_1 \\ \dot{u}_2 \\ \dot{h}_1 \end{bmatrix}, \quad \mathbf{t}_{n2} = \begin{bmatrix} 0 \\ 0 \\ 0 \\ \dot{u}_1 \\ \dot{u}_2 \\ \dot{h}_2 \end{bmatrix},$$

$$\mathbf{t}_{f1} = \begin{bmatrix} \dot{\lambda}_1 \\ 0 \\ 0 \\ \dot{u}_1 \\ -r\dot{\theta}_1 \sin(\theta_1) - r_f\dot{\lambda}_1 \sin(\lambda_1) \\ r\dot{\theta}_1 \cos(\theta_1) + r_f\dot{\lambda}_1 \cos(\lambda_1) \end{bmatrix}, \quad \mathbf{t}_{f2} = \begin{bmatrix} 0 \\ \dot{\lambda}_1 \\ 0 \\ -r\dot{\theta}_2 \sin(\theta_2) - r_f\dot{\lambda}_2 \sin(\lambda_2) \\ \dot{u}_2 \\ -r\dot{\theta}_2 \cos(\theta_2) - r_f\dot{\lambda}_2 \cos(\lambda_2) \end{bmatrix},$$

$$\mathbf{t}_p = \begin{bmatrix} 0 \\ 0 \\ \frac{\pi}{p_p}(\dot{h}_1 - \dot{h}_2) \\ \dot{u}_1 \\ \dot{u}_2 \\ \frac{1}{2}(\dot{h}_1 + \dot{h}_2) \end{bmatrix}$$

with

$$u_i = \frac{p(\psi_{iL} - \psi_{iR})}{4\pi}, \quad \theta_i = \frac{\psi_{iL} + \psi_{iR}}{2G}, \quad h_i = (-1)^{i+1}(r\sin(\theta_i) + l\sin(\lambda_i)), \quad i = 1, 2$$
$$\lambda_1 = 2\pi - \arccos\Big(\frac{u_2}{r} - \cos(\theta_1)\Big), \quad \lambda_2 = \arccos\Big(\frac{u_1}{r} - \cos(\theta_2)\Big)$$

where i indicates the ith limb of the PMC, $\mathbf{t}_{sLi}$, $\mathbf{t}_{sRi}$, $\mathbf{t}_{pUi}$, $\mathbf{t}_{pDi}$, $\mathbf{t}_{bi}$, $\mathbf{t}_{ai}$, $\mathbf{t}_{ni}$, $\mathbf{t}_{fi}$ and $\mathbf{t}_p$ the twists of the left-hand screw; the right-hand screw; the up and the down pulleys; the sliding base; the arm; the nut; the forearm of the ith link, and the twist of the Peppermill, respectively. Moreover, G is the total gear-reduction ratio due to the belt-pulley transmission and the harmonic drive. As well, p_p is the pitch of the Peppermill. Furthermore, r_c and l_c denote the distances of the COM of the arm and the forearm, as depicted in Fig. 4.2.

The principle of conservation of energy is applied to verify the effectiveness of the model: the total output energy of the actuators should equal the change of the system energy within any time interval.

$$\int_{T_0}^{T} \boldsymbol{\tau}^T \dot{\boldsymbol{\psi}}\, dt = \sum_{i=1}^{17} (\Delta K_i + \Delta U_i) \tag{4.4}$$

where $\boldsymbol{\tau}$ and $\dot{\boldsymbol{\psi}}$ are the motor torque array and the array of motor joint rates, respectively. Furthermore, in the above principle, energy loses are neglected. As well, ΔK_i and ΔU_i are the changes of the kinetic energy and the potential energy of the ith body for $t \in [T_0,\ T]$.

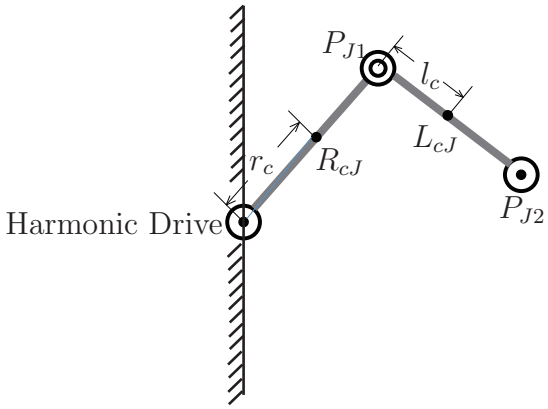

Fig. 4.2: Side view of limb J

The total energy of the PMC and the total energy generated by the actuators are shown in Fig. 4.3. It can be seen that the error between the two plots is negligible, which validates

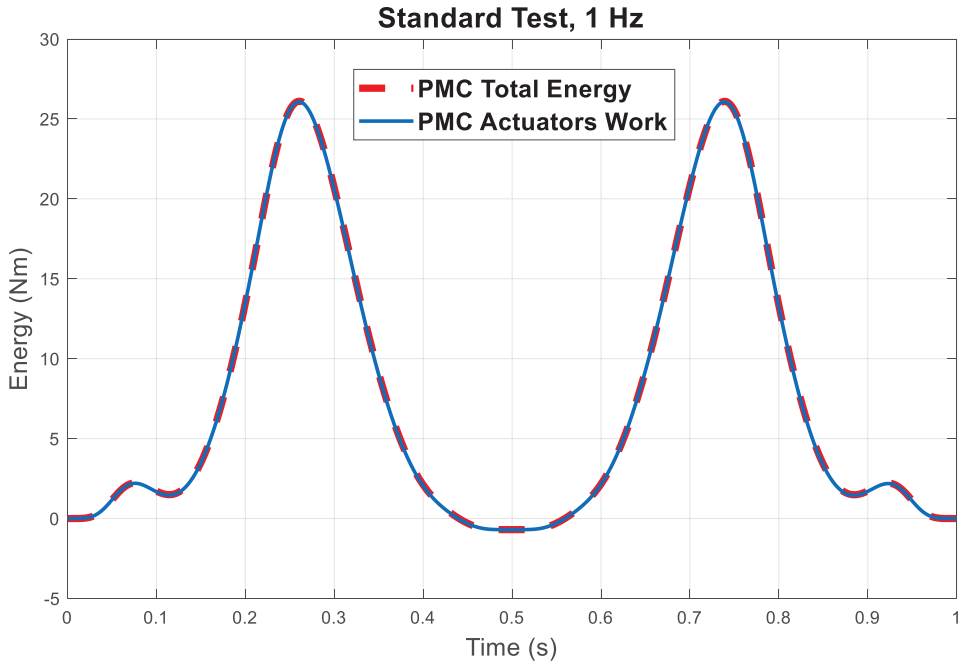

Fig. 4.3: PMC total energy and the actuators work

the model.

4.3 Model Enhancement

In the foregoing section, the rigid-link conservative dynamics model of the PMC was built. In this section, joint friction, parameter uncertainty, process noise, and measurement noise are all taken into account in order to make the model realistic.

Friction plays an important role in robot performance. It is crucial to compensate for friction in the robot control schemes, which becomes crucial in high-speed operations. The tracking performance of the control scheme is decisively affected by friction compensation. In our case, Rayleigh damping is introduced to model power losses, without taking stiffness matrix into consideration. To this end, we introduce the *damping friction matrix*, namely,

$$\mathbf{D}(t) = \alpha \mathbf{I}(t) \tag{4.5}$$

where $\mathbf{I}(t)$ is defined in eq. (4.1) as the inertia tensor, while α is the *mass proportional Rayleigh damping coefficient*. Therefore, the enhanced dynamics model of the PMC, taking friction into consideration, is obtained as

$$\boldsymbol{\tau}(t) = \mathbf{I}(t)\ddot{\boldsymbol{\psi}}(t) + \mathbf{C}(t)\dot{\boldsymbol{\psi}}(t) + \mathbf{D}(t)\dot{\boldsymbol{\psi}}(t) - \boldsymbol{\gamma}(t) \tag{4.6}$$

Some parameters in the dynamics model of the PMC are known only through their nominal design values, their actual values deviating from nominal in practice. In our case, these parameters include the mass and the length of the arms and the forearms of the PMC. These values are assumed to deviate from the *nominal design values* by small amounts that follow a Gaussian distribution with a standard deviation of 5%, which is higher than the one would find upon considering standard tolerances.

Moreover, process noise and measurement noise are introduced in the model. The former comes from the rotor imbalance and friction in the motors, the latter from encoder uncertainty due to their discrete nature. The covariance matrix of the process noise is related to the maximum motor torques, arrayed in vector $\boldsymbol{\tau}_{\max}$; the covariance matrix of the measurement noise is related to the resolution of the encoder ϵ. Noise has a significant influence on controller design. In our case, a Kalman filter and an extended Kalman filter are applied and optimized to mitigate the impact noise. Based on the three-sigma model, the assumption is that the standard deviation of the process noise and measurement noise are $\sigma_p = (1/30)\tau_{\max}$ and $\sigma_m = 2\epsilon$. The mean and covariance matrices of process and

measurement noise are

$$E[\mathbf{w}] = E[\mathbf{v}] = \mathbf{O}, \quad E[\mathbf{w}\mathbf{w}^T] = \text{diag}(\sigma_{p1}^2, \sigma_{p2}^2, \sigma_{p3}^2, \sigma_{p4}^2), \quad E[\mathbf{v}\mathbf{v}^T] = \sigma_m^2 \mathbf{1},$$

where $\mathbf{w}$ is the process noise, $\mathbf{v}$ the measurement noise, σ_{pi} the standard deviation of the ith motor, $\mathbf{O}$ the 4×4 zero matrix and $\mathbf{1}$ the 4×4 identity matrix.

4.4 Dynamics Model of the Virtual Flexible Motor Shaft

In this section, the dynamics model of the virtual flexible motor shaft (VFMS) of the PMC is built, which takes link flexibility into consideration to make the model realistic. The flexibility of the arms and the forearms is transferred to the motor shafts. Then, the model represents a robot with rigid arms and forearms, but flexible motor shafts. It is assumed that the motor and the shaft are connected by a massless torsional spring, as shown in Fig. 4.4. The natural frequency of this motor-shaft system is assumed to coincide with the

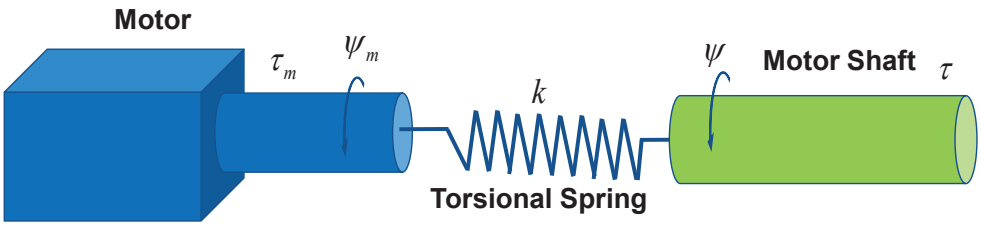

Fig. 4.4: VFMS model

natural frequency of the flexible-link robot structure, obtained in Section 3.4. This model is developed on the basis of the rigid-link model, as shown in eq. (4.6).

The dynamics model of this system is represented as

$$\mathbf{J}\ddot{\boldsymbol{\psi}}_m(t) + \mathbf{K}[\boldsymbol{\psi}_m(t) - \boldsymbol{\psi}(t)] = \boldsymbol{\tau}_m(t) \tag{4.7}$$

where

$$\mathbf{J} = J\mathbf{1}, \quad \mathbf{K} = k\mathbf{1} \tag{4.8}$$

with $\mathbf{1}$ denoting the 4×4 identity matrix, while $\boldsymbol{\psi}_m$ the angular displacement vector of the motors, $\boldsymbol{\psi}$ the angular displacement vector of the motor shafts, $\boldsymbol{\tau}_m$ the motor torque

vector, J and k the moment of inertia of the motor shaft and the torsional stiffness of the virtual spring. The torque $\boldsymbol{\tau}$ is generated by the elastic torsional deformation of the spring, namely,

$$\boldsymbol{\tau}(t) = \mathbf{K}[\boldsymbol{\psi}_m(t) - \boldsymbol{\psi}(t)] = k[\boldsymbol{\psi}_m(t) - \boldsymbol{\psi}(t)] \tag{4.9}$$

Substitution of eqs. (4.7) and (4.9) into eq. (4.6) leads to the VFMS dynamics model of the PMC:

$$\boldsymbol{\tau}_m(t) = \mathbf{I}(t)\ddot{\boldsymbol{\psi}}(t) + \mathbf{C}(t)\dot{\boldsymbol{\psi}}(t) + \mathbf{D}(t)\dot{\boldsymbol{\psi}}(t) - \boldsymbol{\gamma}(t) + \mathbf{J}\ddot{\boldsymbol{\psi}}_m(t) \tag{4.10}$$

Chapter 5

Control Schemes

5.1 Introduction

Based on the mathematical models derived in the previous sections, the pertinent control schemes are formulated as described in this chapter. Four kinds of control schemes are designed based on the rigid-link mathematical model and introduced in Sections 5.2–5.5. Process and measurement noise are applied to the VFMS model to validate the control schemes. Moreover, several trajectories are designed to test the robustness of the schemes. Their tracking performance, pros and cons, are discussed in Section 5.6. In Section 5.7, the eligibility of a linear controller for this nonlinear system is discussed.

5.2 Gain-scheduling: Linear Quadratic Regulator and Kalman Filter

This section is devoted to the gain-scheduling linear quadratic regulator combined with the Kalman filter control scheme. First, the concept of a gain-scheduling control scheme is introduced. The design details of this scheme are introduced in the balance of the chapter.

5.2.1 Introduction of the Gain-scheduling Controller

The gain-scheduling method is one of the most widely used control schemes for nonlinear systems. It is based on linearization and interpolation. The gain-scheduling control scheme of the PMC is taken as an example to illustrate the design process. Firstly, the nonlinear

mathematical model is linearized at several operation points along the desired trajectory to obtain a family of linear plant models. The output of the PMC is the vector array of the motor angular displacements. Because joint positions are only measured, an observer is designed to estimate the joint rates. Secondly, the controller and observer gains are tuned for each linear plant model. Thirdly, a gain-scheduling architecture is designed, with the controller and observer gains tuned according to a scheduling variable, i.e., the output of the plant. Lastly, the output of the feedback controller is obtained by multiplying the controller gain by the state error. The motor torque is obtained through the sum of the feed-forward desired torque and the output torque of the feedback controller. The process noise **d** and the measurement noise **n** are taken into account as introduced in Section 4.3. The control scheme diagram is shown in Fig. 5.1. The design details of the gain-scheduling

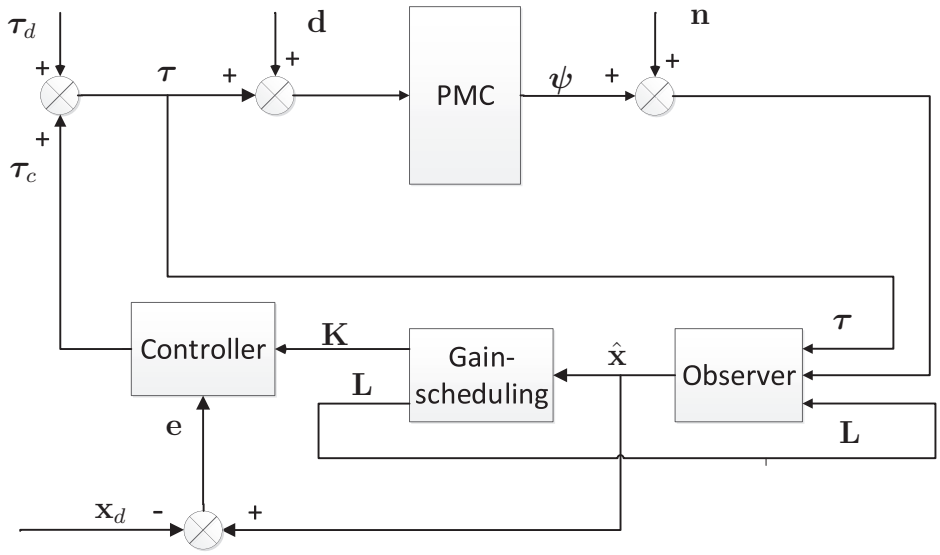

Fig. 5.1: Control scheme diagram

LQR combined with the Kalman filter (KF) are introduced below.

5.2.2 Operation Points

The operation trajectory under study is called the Adept cycle [56, 57, 56]. The trajectory involves a vertical upward translation of 25 mm of the gripper, followed by a horizontal translation of 300 mm and a final vertical downward translation of 25 mm, then back to the starting pose along the same path. During the horizontal section, the gripper has to

undergo a rotation of 180° about a vertical axis, then come back to the original orientation, as depicted in Fig. 3.2. There are i_N operation points in total, and hence $j_N = i_N - 1$ segments, distributed along the path. In our case, 11 operation points are chosen. There are only six points on the spatial path because another five points, printed in red, overlap in the space domain, as shown in Fig. 5.2.

Fig. 5.2: Operation points of the path

5.2.3 Linearization

A nonlinear system, in general, is described as

$$\dot{\mathbf{x}}(t) = \mathbf{f}(\mathbf{x}(t), \mathbf{u}(t)), \quad \mathbf{x}(0) = \mathbf{x}_0, \tag{5.1a}$$

$$\mathbf{y}(t) = \mathbf{g}(\mathbf{x}(t), \mathbf{u}(t)), \tag{5.1b}$$

where $\mathbf{x}(t) \in \mathbb{R}^q$ is the state, $\mathbf{u}(t) \in \mathbb{R}^p$ the input, $\mathbf{y}(t) \in \mathbb{R}^m$ the output. The relationships between a nominal trajectory, $\bar{\mathbf{x}}(t)$, $\bar{\mathbf{u}}(t)$ and $\bar{\mathbf{y}}(t)$, and perturbations, $\delta\mathbf{x}(t)$, $\delta\mathbf{u}(t)$ and $\delta\mathbf{y}(t)$, to the nominal trajectory are

$$\mathbf{x}(t) = \bar{\mathbf{x}}(t) + \delta\mathbf{x}(t) \tag{5.2}$$

$$\mathbf{u}(t) = \bar{\mathbf{u}}(t) + \delta\mathbf{u}(t) \tag{5.3}$$

$$\mathbf{y}(t) = \bar{\mathbf{y}}(t) + \delta\mathbf{y}(t) \tag{5.4}$$

Substitution of eqs. (5.2) and (5.3) into eq. (5.1a), then expansion of $\mathbf{f}(\mathbf{x}(t), \mathbf{u}(t))$ using a Taylor-series expansion leads to

$$\dot{\bar{\mathbf{x}}}(t) + \delta\dot{\mathbf{x}}(t) = \mathbf{f}(\bar{\mathbf{x}}(t) + \delta\mathbf{x}(t), \bar{\mathbf{u}}(t) + \delta\mathbf{u}(t)) = \mathbf{f}(\bar{\mathbf{x}}(t), \bar{\mathbf{u}}(t)) + \widetilde{\mathbf{A}}(t)\delta\mathbf{x}(t) + \widetilde{\mathbf{B}}(t)\delta\mathbf{u}(t) + \text{HOT} \tag{5.5}$$

where

$$\widetilde{\mathbf{A}}(t) = \left.\frac{\partial \mathbf{f}(\mathbf{x}(t), \mathbf{u}(t))}{\partial \mathbf{x}(t)}\right|_{\mathbf{x}(t)=\bar{\mathbf{x}}(t), \mathbf{u}(t)=\bar{\mathbf{u}}(t)} \tag{5.6}$$

$$\widetilde{\mathbf{B}}(t) = \left.\frac{\partial \mathbf{f}(\mathbf{x}(t), \mathbf{u}(t))}{\partial \mathbf{u}(t)}\right|_{\mathbf{x}(t)=\bar{\mathbf{x}}(t), \mathbf{u}(t)=\bar{\mathbf{u}}(t)} \tag{5.7}$$

and HOT stands for the higher-order terms.

Substitution of eqs. (5.2–5.4) into eq. (5.1b), then expansion of $\mathbf{g}(\mathbf{x}(t), \mathbf{u}(t))$ using a Taylor-series expansion leads to

$$\bar{\mathbf{y}}(t) + \delta\mathbf{y}(t) = \mathbf{g}(\bar{\mathbf{x}}(t) + \delta\mathbf{x}(t), \bar{\mathbf{u}}(t) + \delta\mathbf{u}(t)) = \mathbf{g}(\bar{\mathbf{x}}(t), \bar{\mathbf{u}}(t)) + \widetilde{\mathbf{C}}(t)\delta\mathbf{x}(t) + \widetilde{\mathbf{D}}(t)\delta\mathbf{u}(t) + \text{HOT} \tag{5.8}$$

where

$$\widetilde{\mathbf{C}}(t) = \left.\frac{\partial \mathbf{g}(\mathbf{x}(t), \mathbf{u}(t))}{\partial \mathbf{x}(t)}\right|_{\mathbf{x}(t)=\bar{\mathbf{x}}(t), \mathbf{u}(t)=\bar{\mathbf{u}}(t)} \tag{5.9}$$

$$\widetilde{\mathbf{D}}(t) = \left.\frac{\partial \mathbf{g}(\mathbf{x}(t), \mathbf{u}(t))}{\partial \mathbf{u}(t)}\right|_{\mathbf{x}(t)=\bar{\mathbf{x}}(t), \mathbf{u}(t)=\bar{\mathbf{u}}(t)} \tag{5.10}$$

Neglecting the HOT, the linearized system is represented as

$$\delta\dot{\mathbf{x}}(t) = \widetilde{\mathbf{A}}(t)\delta\mathbf{x}(t) + \widetilde{\mathbf{B}}(t)\delta\mathbf{u}(t) \tag{5.11}$$

$$\delta\mathbf{y}(t) = \widetilde{\mathbf{C}}(t)\delta\mathbf{x}(t) + \widetilde{\mathbf{D}}(t)\delta\mathbf{u}(t) \tag{5.12}$$

In our case, the rigid-link dynamics model of the PMC is

$$\boldsymbol{\tau}(t) = \mathbf{I}(t)\ddot{\boldsymbol{\psi}}(t) + \mathbf{C}(t)\dot{\boldsymbol{\psi}}(t) - \boldsymbol{\gamma}(t) \tag{5.13}$$

as defined in eq. (4.1).

Rearrangement of eq. (5.13) leads to

$$\ddot{\boldsymbol{\psi}}(t) = \mathbf{I}(t)^{-1}(\boldsymbol{\tau}(t) - \mathbf{C}(t)\dot{\boldsymbol{\psi}}(t) + \boldsymbol{\gamma}(t)) = \mathbf{f}(\mathbf{x}(t), \boldsymbol{\tau}(t)) \tag{5.14}$$

where $\mathbf{x}(t) = \begin{bmatrix}\boldsymbol{\psi}(t)^T & \dot{\boldsymbol{\psi}}(t)^T\end{bmatrix}^T$.

By resorting to eqs. (5.6) and (5.7), the linearized model of the PMC is

$$\delta\ddot{\boldsymbol{\psi}}(t) = \widetilde{\mathbf{A}}_{\text{b}1}(t)\delta\boldsymbol{\psi}(t) + \widetilde{\mathbf{A}}_{\text{b}2}(t)\delta\dot{\boldsymbol{\psi}}(t) + \widetilde{\mathbf{B}}_{\text{b}}(t)\delta\boldsymbol{\tau}(t) \tag{5.15}$$

with the definitions below:

$$\widetilde{\mathbf{A}}_{\mathrm{b}1}(t) = \left.\frac{\partial \mathbf{f}(\mathbf{x}(t), \boldsymbol{\tau}(t))}{\partial \boldsymbol{\psi}(t)}\right|_{\mathbf{x}(t)=\bar{\mathbf{x}}(t), \boldsymbol{\tau}(t)=\bar{\boldsymbol{\tau}}(t)} \tag{5.16}$$

$$\widetilde{\mathbf{A}}_{\mathrm{b}2}(t) = \left.\frac{\partial \mathbf{f}(\mathbf{x}(t), \boldsymbol{\tau}(t))}{\partial \dot{\boldsymbol{\psi}}(t)}\right|_{\mathbf{x}(t)=\bar{\mathbf{x}}(t), \boldsymbol{\tau}(t)=\bar{\boldsymbol{\tau}}(t)} \tag{5.17}$$

$$\widetilde{\mathbf{B}}_{\mathrm{b}}(t) = \left.\frac{\partial \mathbf{f}(\mathbf{x}(t), \boldsymbol{\tau}(t))}{\partial \boldsymbol{\tau}(t)}\right|_{\mathbf{x}(t)=\bar{\mathbf{x}}(t), \boldsymbol{\tau}(t)=\bar{\boldsymbol{\tau}}(t)} \tag{5.18}$$

5.2.4 State-space Form

By resorting to eq. (5.15), the state-space form is represented as

$$\begin{bmatrix} \delta\dot{\boldsymbol{\psi}}(t) \\ \delta\ddot{\boldsymbol{\psi}}(t) \end{bmatrix} = \begin{bmatrix} \mathbf{O} & \mathbf{1} \\ \widetilde{\mathbf{A}}_{\mathrm{b}1}(t) & \widetilde{\mathbf{A}}_{\mathrm{b}2}(t) \end{bmatrix} \begin{bmatrix} \delta\boldsymbol{\psi}(t) \\ \delta\dot{\boldsymbol{\psi}}(t) \end{bmatrix} + \begin{bmatrix} \mathbf{0} \\ \widetilde{\mathbf{B}}_{\mathrm{b}}(t) \end{bmatrix} \delta\boldsymbol{\tau}(t) = \widetilde{\mathbf{A}}(t) \begin{bmatrix} \delta\boldsymbol{\psi}(t) \\ \delta\dot{\boldsymbol{\psi}}(t) \end{bmatrix} + \widetilde{\mathbf{B}}(t)\delta\boldsymbol{\tau}(t) \tag{5.19}$$

where $\mathbf{O}$ is the 4×4 zero matrix, $\mathbf{1}$ the 4×4 identity matrix and $\mathbf{0}$ the four-dimensional zero vector. In the developments below, $\widetilde{\mathbf{A}}_i$ and $\widetilde{\mathbf{B}}_i$, $i = 1, 2, \ldots, i_{\mathrm{tol}}$, denote the values of $\widetilde{\mathbf{A}}$ and $\widetilde{\mathbf{B}}$ at the ith operation point.

5.2.5 Linear Quadratic Regulator and Kalman Filter

LQR is a controller based on the theory of optimal control. The optimal controller is obtained upon minimization of the quadratic cost function given by [136]

$$J(\mathbf{K}) = \int_0^\infty (\mathbf{x}^T(t)\mathbf{Q}\mathbf{x}(t) + \mathbf{u}^T(t)\mathbf{R}\mathbf{u}(t))\, dt \tag{5.20}$$

where $\mathbf{Q} = \mathbf{Q}^T \geq \mathbf{O}$ and $\mathbf{R} = \mathbf{R}^T > \mathbf{O}$ are the weight matrices, penalizing the state $\mathbf{x}(t)$ and control input $\mathbf{u}(t)$, respectively. The LQR is tuned based on these two matrices. The choice of $\mathbf{Q}$ and $\mathbf{R}$ depends on how we want to penalize the states and the control inputs. Therefore, the idea of the LQR is to seek the maximum return from the system at a minimum cost. In our case, the minimization of the above cost *functional* leads to the algebraic Riccati equation, namely,

$$\widetilde{\mathbf{A}}_i^T\mathbf{P}_i + \mathbf{P}_i\widetilde{\mathbf{A}}_i - \mathbf{P}_i\widetilde{\mathbf{B}}_i\mathbf{R}^{-1}\widetilde{\mathbf{B}}_i^T\mathbf{P}_i + \mathbf{Q} = \mathbf{0}, \quad i = 1, 2, \ldots, i_{\mathrm{tol}} \tag{5.21}$$

which results in the feedback gain matrix $\mathbf{K}_i = -\mathbf{R}^{-1}\widetilde{\mathbf{B}}_i^T\mathbf{P}_i$ at the ith operation point. The LQR requires that all the states be available for feedback, but, in our case, the angular rates of the motors are not available. Therefore, an observer needs to be designed to estimate them. In particular, a KF will be used to estimate the states.

A time-varying linear system, taking the measurement noise and process noise into consideration, is given by

$$\begin{aligned}\dot{\mathbf{x}}(t) &= \mathbf{A}(t)\mathbf{x}(t) + \mathbf{B}(t)\mathbf{u}(t) + \mathbf{G}\mathbf{w}, \quad \mathbf{x}(0) = \mathbf{x}_0\\ \mathbf{y}(t) &= \mathbf{C}(t)\mathbf{x}(t) + \mathbf{v}\end{aligned}$$

where $\mathbf{w}$ and $\mathbf{v}$ are Gaussian, stationary white process and measurement noise. Matrix $\mathbf{G}$ is often set equal to the identity matrix, which means that the process noise goes directly into the state-variables. The mean and covariance matrices of $\mathbf{w}$ and $\mathbf{v}$ are

$$E[\mathbf{w}] = E[\mathbf{v}] = \mathbf{O}, \quad E[\mathbf{w}\mathbf{w}^T] = \mathbf{W}, \quad E[\mathbf{v}\mathbf{v}^T] = \mathbf{V}$$

The optimal state estimate $\hat{\mathbf{x}}(t)$, given by the KF, is obtained upon integration of

$$\dot{\hat{\mathbf{x}}}(t) = \mathbf{A}(t)\hat{\mathbf{x}}(t) + \mathbf{B}(t)\mathbf{u}(t) + \mathbf{L}(t)(\mathbf{y}(t) - \mathbf{C}(t)\hat{\mathbf{x}}(t)), \quad \hat{\mathbf{x}}(0) = \mathbf{x}_0$$

Key to the synthesis of the KF is the solution of the Riccati equation [137]

$$\mathbf{A}(t)\mathbf{S}(t)+\mathbf{S}(t)\mathbf{A}^T(t)-\mathbf{S}(t)\mathbf{C}^T(t)\mathbf{V}^{-1}\mathbf{C}(t)\mathbf{S}(t)+\mathbf{G}(t)\mathbf{W}\mathbf{G}^T(t) = \dot{\mathbf{S}}(t), \quad \mathbf{S}(0) = \mathbf{S}_0 \quad (5.22)$$

which results in the observer gain matrix $\mathbf{L}(t) = \mathbf{S}(t)\mathbf{C}^T(t)\mathbf{V}^{-1}$.

In our case, $\mathbf{C} = \begin{bmatrix}\mathbf{1} & \mathbf{O}\end{bmatrix}$, where $\mathbf{1}$ is the 4×4 identity matrix, while $\mathbf{O}$ the 4×4 zero matrix. In our case, the problem formulation leads to a sequence of algebraic Riccati equations, namely,

$$\widetilde{\mathbf{A}}_i\mathbf{S}_i + \mathbf{S}_i\widetilde{\mathbf{A}}_i^T - \mathbf{S}_i\mathbf{C}^T\mathbf{V}^{-1}\mathbf{C}\mathbf{S}_i + \mathbf{G}\mathbf{W}\mathbf{G}^T = \mathbf{0}, \quad i = 1, 2, \ldots, i_{\text{tol}} \quad (5.23)$$

which results in the observer gain $\mathbf{L}_i = \mathbf{S}_i\mathbf{C}^T\mathbf{V}^{-1}$ at the ith operation point.

5.2.6 Gain-scheduling Method

In order to obtain the controller and observer gains between operation points, a linear gain-scheduling method is introduced in this subsection, based on [138]. The estimated state variable $\hat{\mathbf{x}}(t) = \begin{bmatrix} \boldsymbol{\psi}^T(t) & \dot{\boldsymbol{\psi}}^T(t) \end{bmatrix}^T$ is chosen as the scheduling variable. The estimated state variable is an eight-dimensional vector, as only the four-dimensional angular position vector $\boldsymbol{\psi}(t)$ is used as the scheduling variable. This vector is applied to obtain the estimated platform pose $\hat{\mathbf{p}}(t) = [\hat{x}_c(t) \quad \hat{y}_c(t) \quad \hat{z}_c(t) \quad \hat{\phi}_c(t)]^T$. In our case, there are i_N operation points along the path, distributed evenly in the x-direction. The length of the path in the x-direction is x_N. The path is divided into $i_N - 1$ segments. In the ith segment, the controller and observer gains $\mathbf{K}_i^{\text{ip}}(\hat{x}_c(t))$ and $\mathbf{L}_i^{\text{ip}}(\hat{x}_c(t))$ are

$$\mathbf{K}_i^{\text{ip}}(\hat{x}_c(t)) = s_i(\hat{x}_c(t))\mathbf{K}_i + s_{i+1}(\hat{x}_c(t))\mathbf{K}_{i+1} \tag{5.24}$$

$$\mathbf{L}_i^{\text{ip}}(\hat{x}_c(t)) = s_i(\hat{x}_c(t))\mathbf{L}_i + s_{i+1}(\hat{x}_c(t))\mathbf{L}_{i+1} \tag{5.25}$$

where

$$\begin{aligned} s_i(\hat{x}_c(t)) &= 1 - (\hat{x}_c - (x_N/(i_N-1))(j-1))/(x_N/(i_N-1)) \\ s_{i+1}(\hat{x}_c(t)) &= 1 - s_i(\hat{x}_c(t)) \end{aligned} \tag{5.26}$$

Moreover, in the ith segment, the state-space matrices $\widetilde{\mathbf{A}}_i^{\text{ip}}(\hat{x}_c(t))$ and $\widetilde{\mathbf{B}}_i^{\text{ip}}(\hat{x}_c(t))$ are obtained as convex combinations of $\widetilde{\mathbf{A}}_i$, $\widetilde{\mathbf{A}}_{i+1}$, $\widetilde{\mathbf{B}}_i$ and $\widetilde{\mathbf{B}}_{i+1}$, i.e.,

$$\widetilde{\mathbf{A}}_i^{\text{ip}}(\hat{x}_c(t)) = s_i(\hat{x}_c(t))\widetilde{\mathbf{A}}_i + s_{i+1}(\hat{x}_c(t))\widetilde{\mathbf{A}}_{i+1} \tag{5.27}$$

$$\widetilde{\mathbf{B}}_i^{\text{ip}}(\hat{x}_c(t)) = s_i(\hat{x}_c(t))\widetilde{\mathbf{B}}_i + s_{i+1}(\hat{x}_c(t))\widetilde{\mathbf{B}}_{i+1} \tag{5.28}$$

Since state-space matrices, controller and observer gains are obtained in different segments, the next step is to combine them together into a closed-loop system.

5.2.7 Combination

The combination of controller and observer are shown in the diagram of Fig. 5.1.

5.3 Linear Quadratic Regulator and Extended Kalman Filter

The second control scheme is introduced in this section. The KF observer, used in the first control scheme, is replaced by the extended Kalman filter (EKF). Compared with the linear observer KF, the EKF is a nonlinear observer that takes the nonlinear dynamics of the plant into the account. The EKF can be designed as a semi-real-time or a real-time observer. The real-time extended Kalman filter (REKF) updates the observer gain by solving the Riccati equation in real-time. Therefore, the REKF has a high computational burden, especially in high-speed operations. Compared with the REKF, the semi-real-time extended Kalman filter (SEKF) updates the observer gains by interpolating the observer gains between the operation points according to the estimated state $\hat{\mathbf{x}}(t)$, which sacrifices the property of updating the observer gain in real-time to achieve a smaller computational complexity. Therefore, the SEKF is more suitable for real-time control in practice. The EKF is introduced below.

5.3.1 Extended Kalman Filter

A nonlinear system is given by eq. (5.1a), its output being given by

$$\mathbf{y}(t) = \mathbf{g}(\mathbf{x}(t)) \tag{5.29}$$

The EKF is constructed as

$$\dot{\hat{\mathbf{x}}}(t) = \mathbf{f}(\hat{\mathbf{x}}(t), \mathbf{u}(t)) + \mathbf{L}(t)(\mathbf{y}(t) - \mathbf{g}(\hat{\mathbf{x}}(t))), \quad \hat{\mathbf{x}}(0) = \mathbf{x}_0 \tag{5.30}$$

where $\mathbf{L}(t)$ is the observer gain matrix updated in real-time. To obtain $\mathbf{L}(t)$, the Riccati equation given in eq. (5.22) must be solved, where $\mathbf{A}(t)$ and $\mathbf{C}(t)$ are given in eqs. (5.6) and (5.9) and, in this case $\mathbf{G} = \mathbf{1}$. The observer gain is represented as

$$\mathbf{L}(t) = \mathbf{S}(t)\mathbf{C}^T(t)\mathbf{V}^{-1} \tag{5.31}$$

5.4 Constant-gain Controller

In this section, the third control scheme is introduced. During the process of finding the minimum operation points of the gain-scheduling controller, it is found that the PMC can

be controlled by a controller designed using one operation point, namely, a constant-gain controller combined with a constant-gain observer. The constant controller and observer gains are designed at the middle operation point of the path. The reason why this point is chosen as the only one, instead of any other points, will be explained in Section 5.7. In general, a nonlinear system is controllable by means of a nonlinear controller. A mechanical system is controllable by a PD controller because of its skew-symmetry property [139]. In our case, a constant-gain LQR, combined with the constant-gain KF, is applied to control the robot. Then, an constant-gain EKF is applied to substitute the constant-gain KF to improve the tracking performance of the controller. In order to find the limitations of this controller, a higher-speed operation trajectory is applied to verify the relationship between controllability and operation speed. Moreover, a sine-wave trajectory, is designed and applied to test the tracking performance of this linear controller, as shown in Section 5.6.

5.5 Feed-forward PD Controller Based on the Sliding Mode Scheme

The fourth control scheme is introduced in this section. Inspired by the constant-gain controller, one more linear controller—the feed-forward PD controller, based on the sliding-mode scheme—is designed based on an adaptive control scheme [140]. The dynamics of a general manipulator with n rigid links is given by the model

$$\mathbf{M}(\mathbf{q})\ddot{\mathbf{q}} + \mathbf{C}(\mathbf{q}, \dot{\mathbf{q}})\dot{\mathbf{q}} + \mathbf{g}(\mathbf{q}) = \boldsymbol{\tau} \tag{5.32}$$

where $\mathbf{q}$ is the n-dimensional joint displacement vector array, $\boldsymbol{\tau}$ the n-dimensional motor torque array, $\mathbf{M}(\mathbf{q})$ the $n \times n$ generalized inertia matrix of the manipulator, $\mathbf{C}(\mathbf{q}, \dot{\mathbf{q}})$ the $n \times n$ matrix of Coriolis-and-centrifugal force and $\mathbf{g}(\mathbf{q})$ the n-dimensional generalized-force vector, stemming from gravity. The manipulator is guided to operate along a desired trajectory $\mathbf{q}_d$.

A sliding surface is defined as

$$\dot{\mathbf{e}} + \boldsymbol{\Lambda}\mathbf{e} = \mathbf{0} \tag{5.33}$$

where $\mathbf{e}$ is the tracking error of joint positions, given by

$$\mathbf{e} = \mathbf{q} - \mathbf{q}_d \tag{5.34}$$

while $\dot{\mathbf{e}}$ is the tracking error of the joint velocities, given by

$$\dot{\mathbf{e}} = \dot{\mathbf{q}} - \dot{\mathbf{q}}_d \tag{5.35}$$

Moreover, $\mathbf{\Lambda}$ is a $n \times n$ positive-definite matrix and $\mathbf{0}$ is the n-dimensional zero vector.

A reference trajectory $\mathbf{q}_r$ is then defined as

$$\mathbf{q}_r = \mathbf{q}_d - \mathbf{\Lambda} \int_0^t \mathbf{e}\, dt \tag{5.36}$$

Accordingly,

$$\dot{\mathbf{q}}_r = \dot{\mathbf{q}}_d - \mathbf{\Lambda}\mathbf{e} \tag{5.37}$$

$$\ddot{\mathbf{q}}_r = \ddot{\mathbf{q}}_d - \mathbf{\Lambda}\dot{\mathbf{e}} \tag{5.38}$$

If a sliding surface is defined as

$$\mathbf{s} = \dot{\mathbf{e}}_r = \dot{\mathbf{q}} - \dot{\mathbf{q}}_r = \dot{\mathbf{e}} + \mathbf{\Lambda}\mathbf{e} \tag{5.39}$$

then, the control law becomes

$$\boldsymbol{\tau} = \mathbf{M}(\mathbf{q})\ddot{\mathbf{q}}_r + \mathbf{C}(\mathbf{q}, \dot{\mathbf{q}})\dot{\mathbf{q}}_r + \mathbf{g}(\mathbf{q}) - \mathbf{K}_D\mathbf{s} \tag{5.40}$$

where $\mathbf{K}_D$ is a $n \times n$ positive-definite matrix.

To demonstrate the global convergence of the tracking scheme, a Lyapunov function candidate is considered as

$$V(t) = \frac{1}{2}\mathbf{s}^T\mathbf{M}(\mathbf{q})\mathbf{s} \tag{5.41}$$

whose derivative is

$$\dot{V}(t) = \mathbf{s}^T\mathbf{M}(\mathbf{q})\dot{\mathbf{s}} + \frac{1}{2}\mathbf{s}^T\dot{\mathbf{M}}(\mathbf{q}, \dot{\mathbf{q}})\mathbf{s} \tag{5.42}$$

where $\dot{\mathbf{s}}$ is given by

$$\dot{\mathbf{s}} = \ddot{\mathbf{q}} - \ddot{\mathbf{q}}_r \tag{5.43}$$

Upon substitution of eqs. (5.32) and (5.43) into eq. (5.42), we obtain

$$\dot{V}(t) = \mathbf{s}^T(\boldsymbol{\tau} - \mathbf{C}(\mathbf{q}, \dot{\mathbf{q}})\dot{\mathbf{q}} - \mathbf{g}(\mathbf{q}) - \mathbf{M}(\mathbf{q})\ddot{\mathbf{q}}_r) + \frac{1}{2}\mathbf{s}^T\dot{\mathbf{M}}(\mathbf{q}, \dot{\mathbf{q}})\mathbf{s} \tag{5.44}$$

Further, substitution of eqs. (5.39) and (5.40) into eq. (5.44) leads to

$$\dot{V}(t) = -\mathbf{s}^T \mathbf{K}_D \mathbf{s} + \frac{1}{2}\mathbf{s}^T[\dot{\mathbf{M}}(\mathbf{q}, \dot{\mathbf{q}}) - 2\mathbf{C}(\mathbf{q}, \dot{\mathbf{q}})]\mathbf{s} \tag{5.45}$$

Since the matrix $\dot{\mathbf{M}}(\mathbf{q}, \dot{\mathbf{q}}) - 2\mathbf{C}(\mathbf{q}, \dot{\mathbf{q}})$ is *skew-symmetric*, we have

$$\dot{V}(t) = -\mathbf{s}^T \mathbf{K}_D \mathbf{s} < 0 \tag{5.46}$$

which shows that the output error converges to the sliding surface $\mathbf{s} = \mathbf{0}$. Since $\mathbf{\Lambda}$ is positive-definite, $\mathbf{e}$ and $\dot{\mathbf{e}}$ converge to the n-dimensional zero vector as $t \to \infty$. Therefore, the controller defined by eq. (5.40) is globally, asymptotically stable, thereby guaranteeing a zero steady-state error for joint position and velocity.

5.6 Simulation

This section provides the results obtained when applying different kinds of schemes to control the PMC. Four kinds of controllers are designed based on the rigid-link dynamics model of the robot. We used the simplest plant model to design the controllers and used the most complex model to test their robustness. Joint friction, link flexibility, measurement plus process noise, and parameter uncertainty are all included in the test model. Furthermore, different kinds of trajectories are applied to verify the robustness of the control schemes and to find the limitations of linear control schemes.

5.6.1 1 Cycle Per Second

The simulation is conducted at one Adept cycle per second. The maximum translational tracking error of gain-scheduling LQR combined with KF controller is about 1.7×10^{-4} meter while the maximum rotational error is about -0.05 rad, as shown in Fig. 5.3. Then, the KF observer is substituted by the SEKF observer, which results in a lower rotation error, as shown in Fig. 5.4. The REKF observer is better than the SEKF observer, as introduced. From the simulation results, shown in Fig. 5.5, the translational and rotational tracking errors of gain-scheduling LQR combined with the REKF controller are smaller than the errors shown in Fig. 5.4. The constant-gain LQR combined with the constant-gain EKF controller is applied to control the robot. The maximum translational tracking error is

1×10^{-4} m larger than the gain-scheduling controller, which is still good, as plotted in Fig. 5.6. However, another linear controller, namely, the feed-forward PD controller, based on the sliding-mode scheme, is not as good as the constant-gain LQR controller. The maximum translational tracking error is about twice as big as that of the constant-gain LQR controller, as shown in Fig. 5.7.

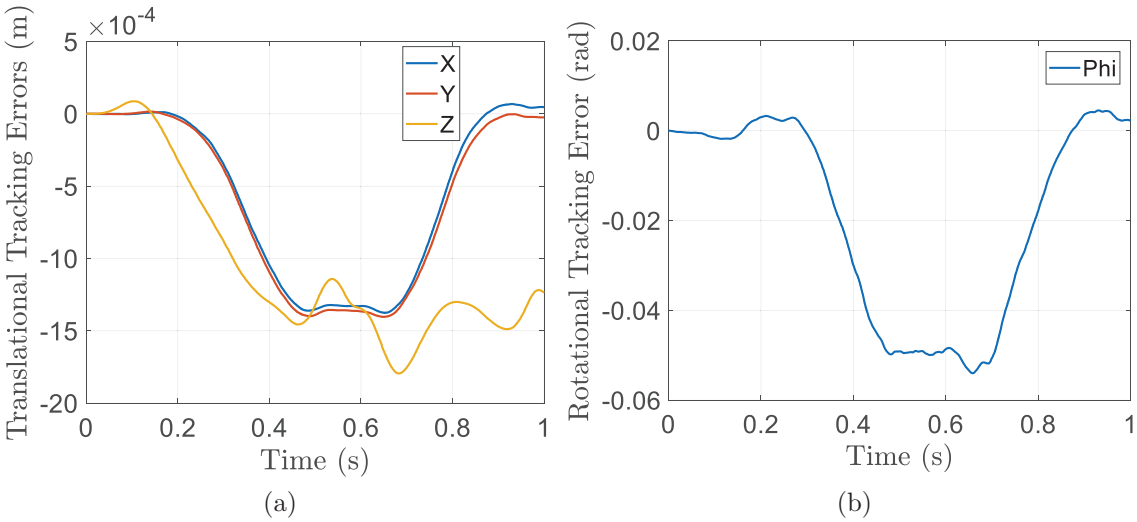

Fig. 5.3: The tracking errors of a 1-cycle/s operation in Cartesian space of the gain-scheduling LQR combined with the KF controller: (a) translational tracking errors; (b) rotational tracking error

In order to verify the design quality of the observers, the relationships between 3σ and estimation errors of four motor angular positions ψ_i of the KF, the SEKF, and the REKF are shown in Figs. 5.8–5.10, respectively. From these results, it is apparent that our observers are suitably designed, because the estimation error of the state variables are located inside the 3σ curves.

From the simulation results, we can observe that the tracking performance of these controllers is promising when the speed is 1 cycle per second. The best controller is the constant-gain LQR combined with the constant-gain EKF controller, which has almost the minimum tracking errors and the lowest computational complexity.

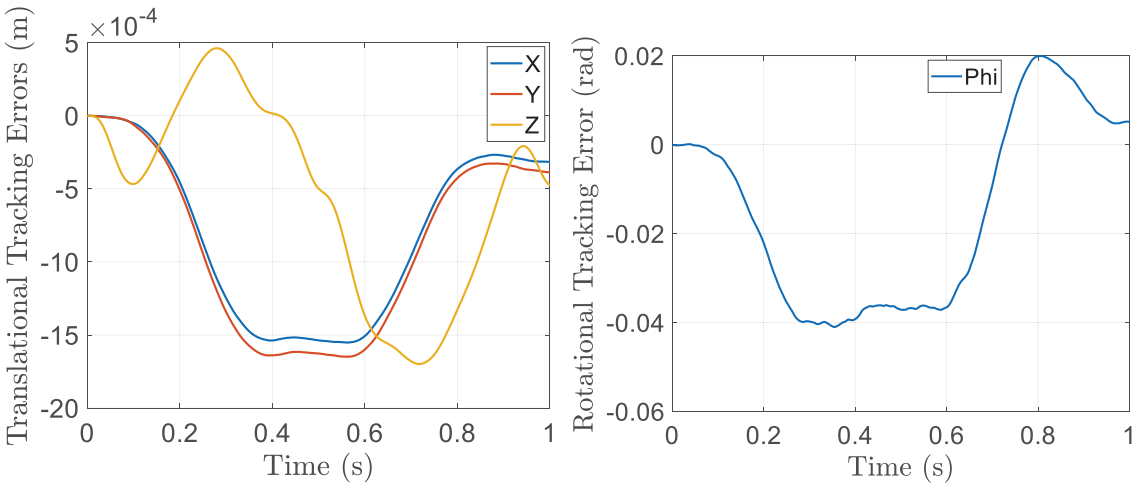

Fig. 5.4: The tracking errors of a 1-cycle/s operation in Cartesian space of the gain-scheduling LQR combined with the SEKF controller: (a) translational tracking errors; (b) rotational tracking error

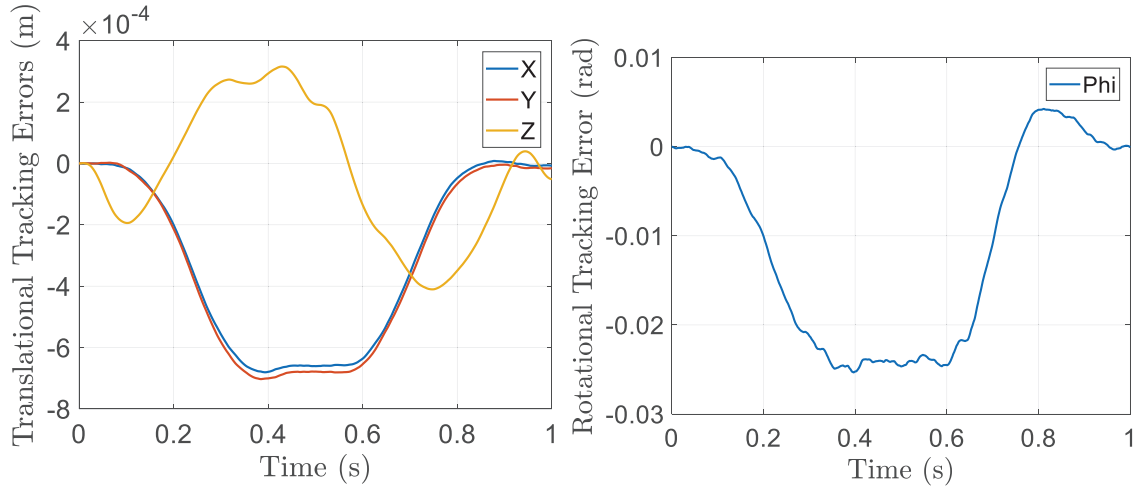

Fig. 5.5: The tracking errors of a 1-cycle/s operation in Cartesian space of the gain-scheduling LQR combined with the REKF controller: (a) translational tracking errors; (b) rotational tracking error

5.6.2 10 Cycles Per Second

It is necessary to test the performance of the linear controllers under high-speed because our aim is a high-speed pick-and-place robot to break the current record of three cycles

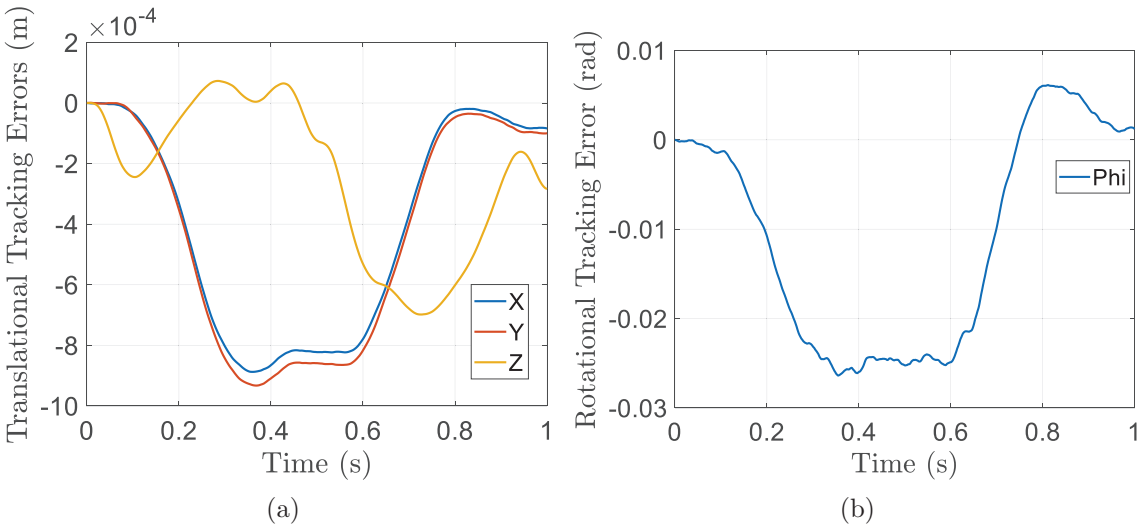

Fig. 5.6: The tracking errors of a 1-cycle/s operation in Cartesian space of the constant-gain LQR combined with the constant-gain EKF controller: (a) translational tracking errors; (b) rotational tracking error

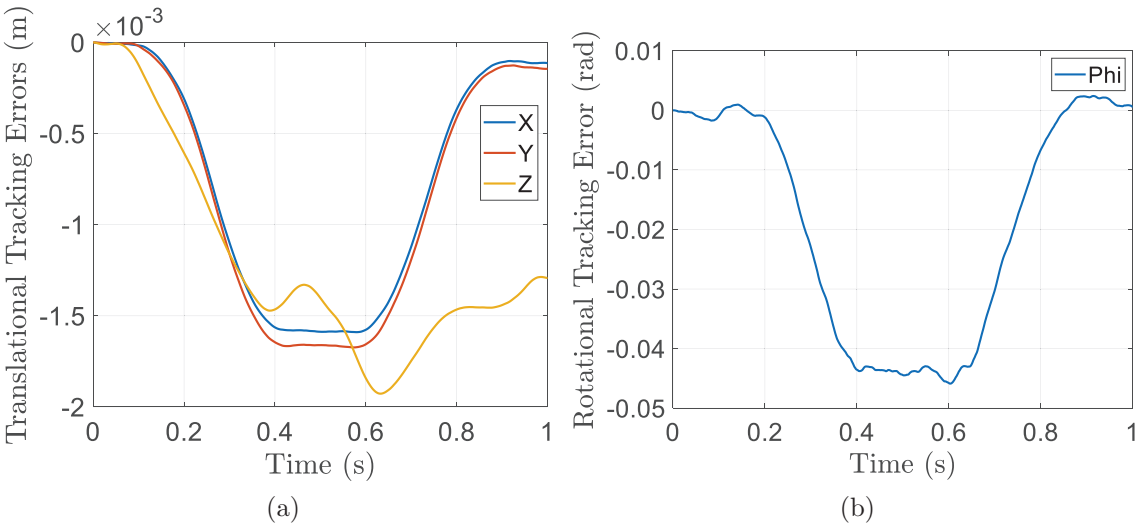

Fig. 5.7: The tracking errors of a 1-cycle/s operation in Cartesian space of the feed-forward PD controller, based on the sliding-mode scheme: (a) translational tracking errors; (b) rotational tracking error

per second. Moreover, we want to investigate whether our controller is effective under high operation speeds. The linear controllers were tested at 10 cycles per second, which is three times the record. A friction-matrix term is added to the model to account for power losses.

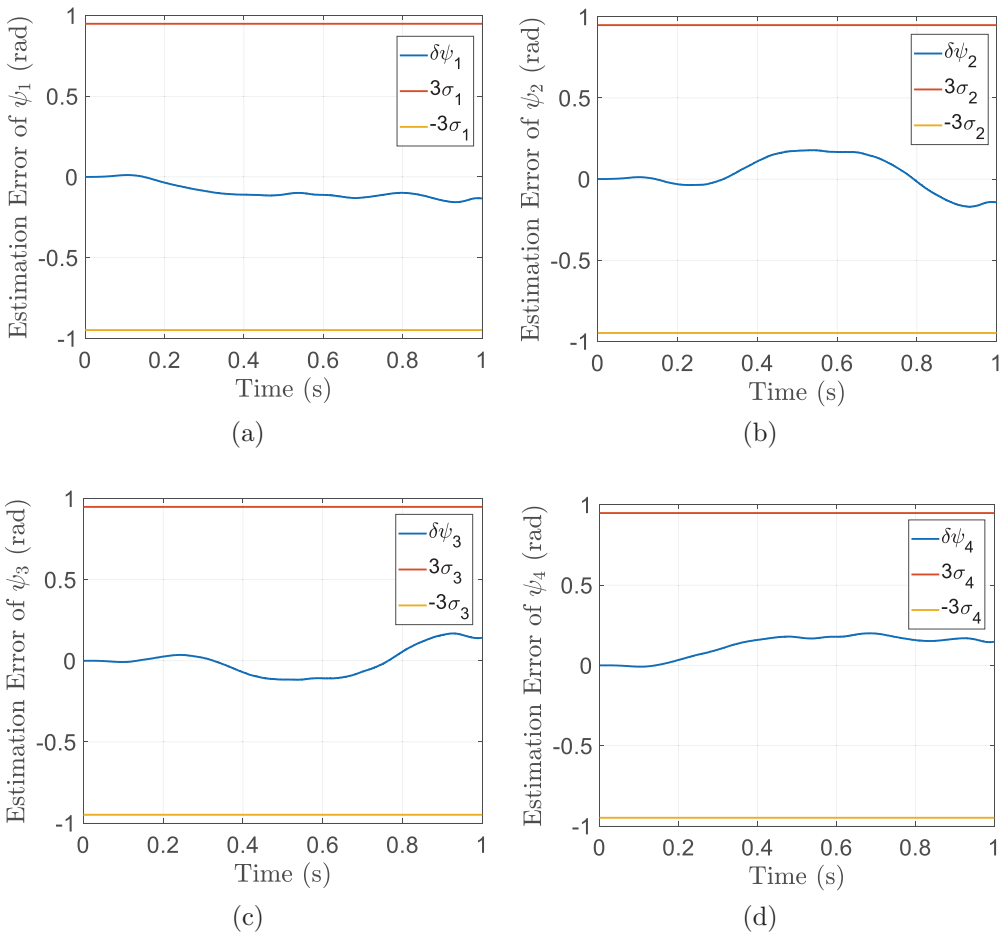

Fig. 5.8: Estimation errors of angular positions of the KF: (a) $\delta\psi_1$; (b) $\delta\psi_2$; (c) $\delta\psi_3$; and (d) $\delta\psi_4$

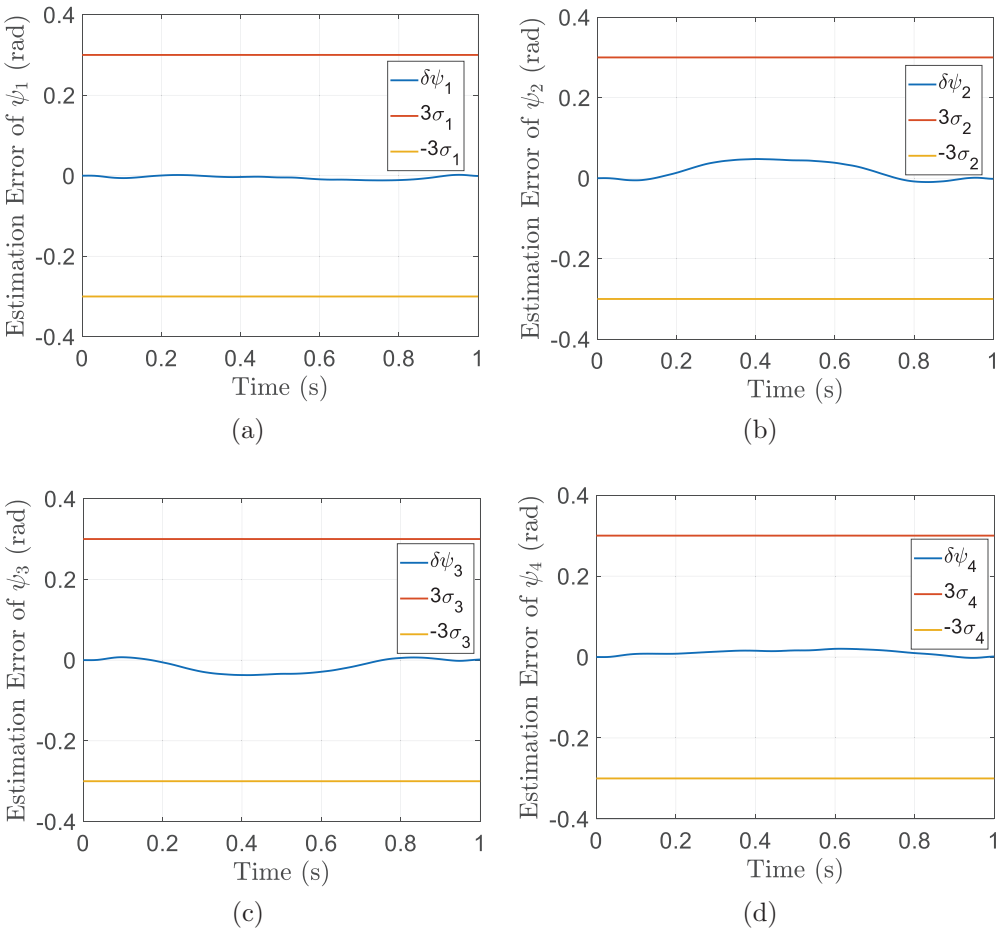

Fig. 5.9: Estimation errors of angular positions of the SEKF: (a) $\delta\psi_1$; (b) $\delta\psi_2$; (c) $\delta\psi_3$; and (d) $\delta\psi_4$

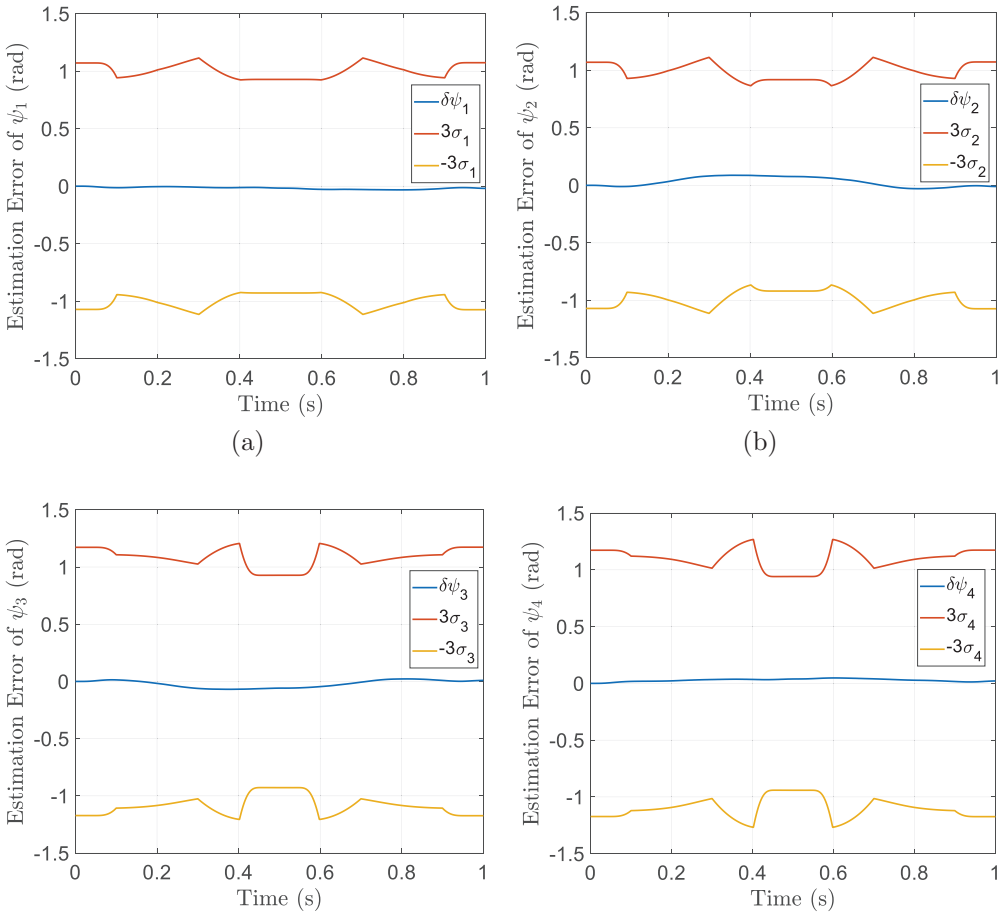

Fig. 5.10: Estimation errors of angular positions of the REKF: (a) $\delta\psi_1$; (b) $\delta\psi_2$; (c) $\delta\psi_3$; and (d) $\delta\psi_4$

The Cartesian space tracking errors are displayed in Figs. 5.11 and 5.12. Simulation results show that the linear controllers have an excellent tracking performance even at 10 cycles per second.

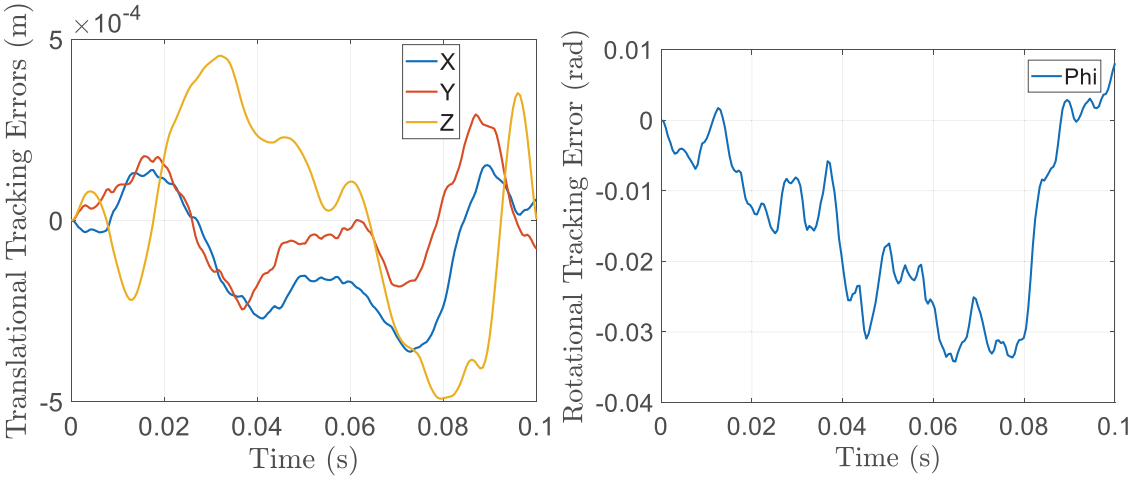

Fig. 5.11: The tracking errors at 10 cycles/s in Cartesian space of the constant-gain LQR combined with the constant-gain EKF controller: (a) translational tracking errors; (b) rotational tracking error

5.6.3 Sine-wave Trajectory

The horizontal translation length of the Adept cycle, 300 mm, is much longer than that in the vertical direction, 25 mm. The short vertical direction occludes the nonlinearity of the dynamics of the PMC, when the robot tracks that trajectory. Therefore, a more complex trajectory, dubbed the *sine-wave trajectory* is designed. One more objective when designing this trajectory is to verify whether the linear controllers are suitable for a more demanding task. The trajectory is depicted in Fig. 5.13. The Cartesian space tracking errors of the two linear controllers are shown in Figs. 5.14 and 5.15. The simulation results show that the linear controllers can still have a good tracking performance even in the presence of a trajectory richer in nonlinearities.

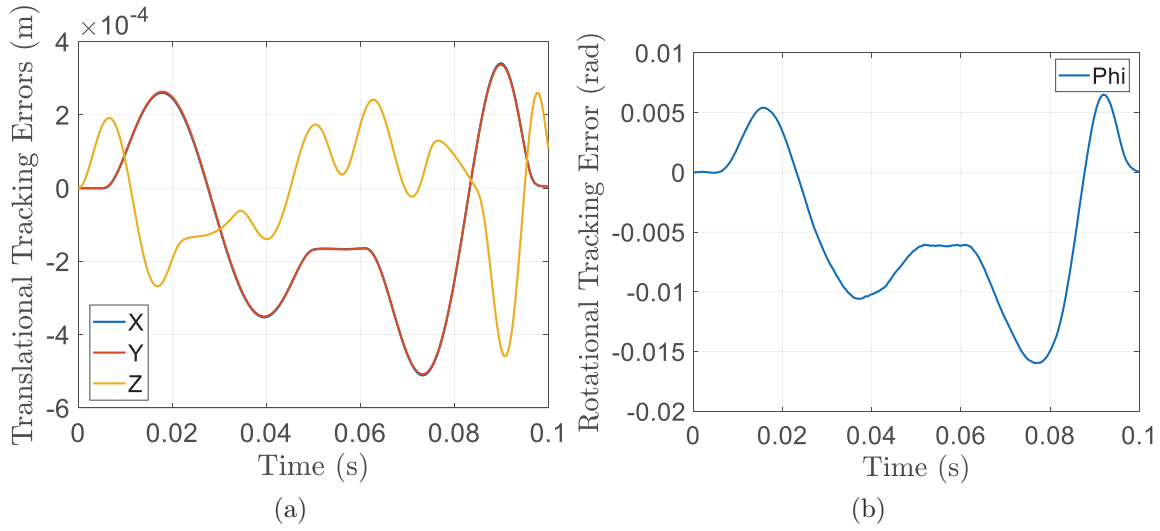

Fig. 5.12: The tracking errors at 10 cycles/s in Cartesian space of the feed-forward PD controller, based on the sliding-mode scheme: (a) translational tracking errors; (b) rotational tracking error

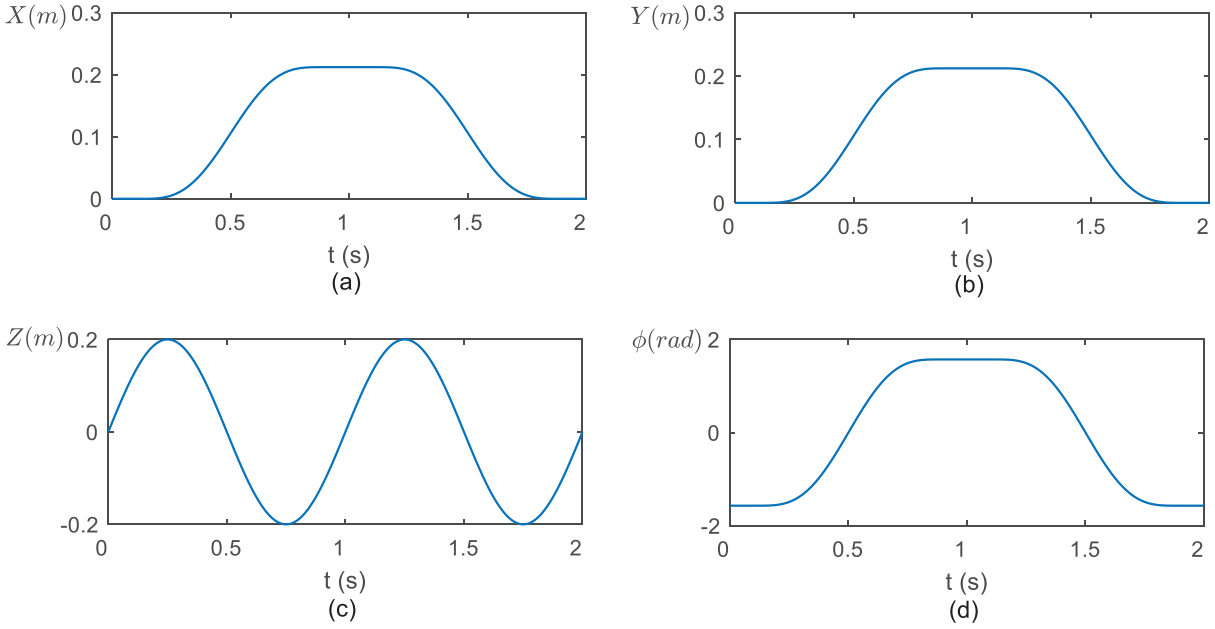

Fig. 5.13: The sine-wave trajectory plots: (a) the translation along the x-axis, (b) the translation along the y-axis, (c) the translation along the z-axis , and (d) the rotation about the z-axis

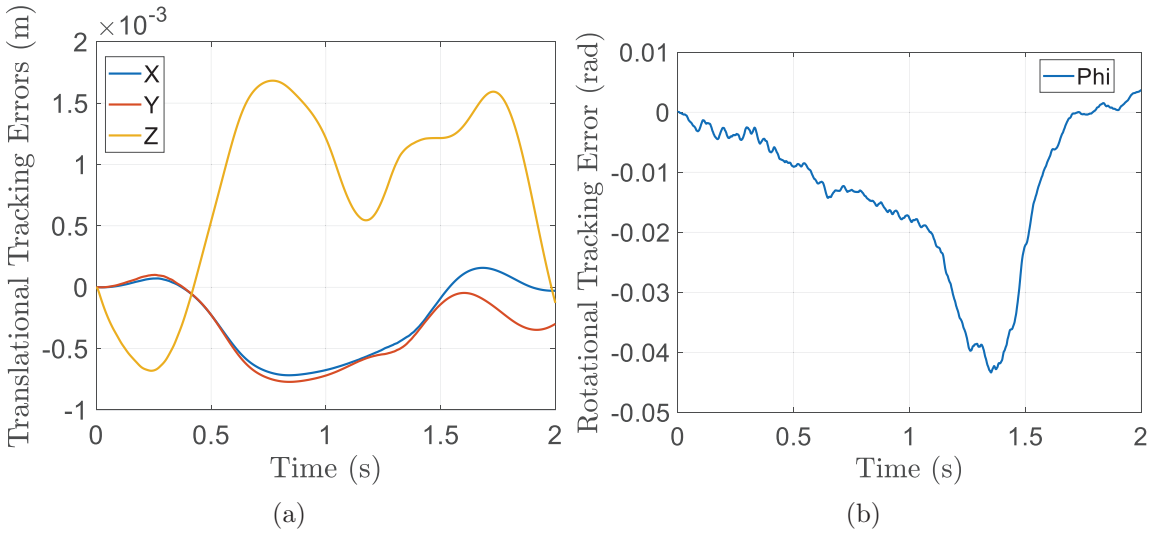

Fig. 5.14: The tracking errors of the sine-wave trajectory in Cartesian space of the constant-gain controller: (a) translational tracking errors; (b) rotational tracking error

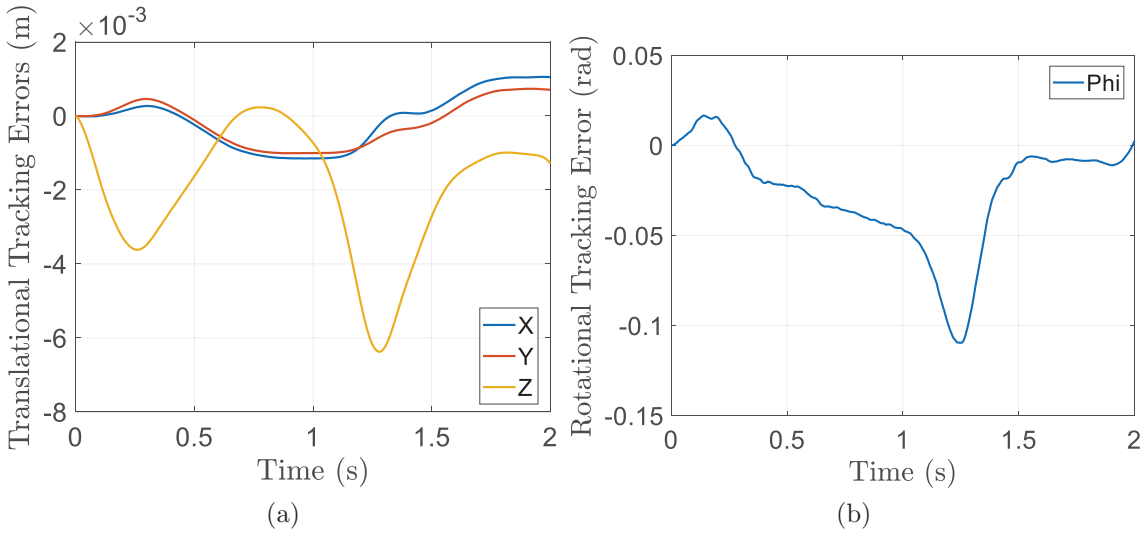

Fig. 5.15: The tracking errors of the sine-wave trajectory in Cartesian space of the feed-forward PD controller, based on the sliding-mode scheme: (a) translational tracking errors; (b) rotational tracking error

5.7 Discussion

The reason why a linear controller is capable of controlling a nonlinear system is discussed in this section. First of all, we want to find whether the feed-forward signal counteracts the

nonlinearity of the PMC so that the constant-gain controller is eligible to control the robot. The feed-forward signal is obtained through the dynamics model. However, there are some ignored factors, when the dynamics model is constructed, such as friction and parameter uncertainty. Therefore, the feed-forward signal is not reliable, i.e., it is not the exact input to produce the prescribed output. Based on this consideration, the feed-forward signal is cancelled in the control loop to test the robustness of the constant-gain controller at 10 cycles per second. The simulation result is shown in Fig. 5.16.

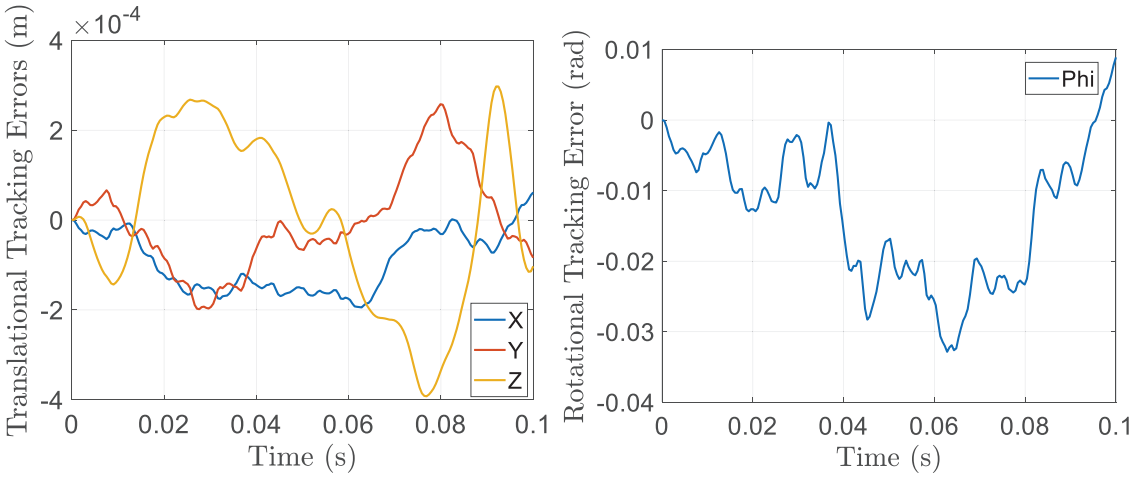

Fig. 5.16: The tracking errors at 10 cycles/s in Cartesian space of the constant-gain LQR combined with the constant-gain EKF controller and no feed-forward signal: (a) translational tracking errors; (b) rotational tracking error

From the above simulation result, the performance of the constant-gain controller without the feed-forward signal is still promising. Therefore, the reason why a linear controller can control a nonlinear system does not lie in the feed-forward signal.

According to the introduction of the constant-gain controller, we know that it is designed based on one specific operation point. Different operation points correspond to different controller gain matrices. During the process of designing the constant-gain controller, simulation results show that the choice of a specific operation point doesn't have a significant influence on the tracking errors, which motivates us to investigate the variation of the controller gain matrix $\mathbf{K}_i$ at the ith operation point along the Adept cycle. Since matrix $\mathbf{K}$ is a dimensionally inhomogeneous, it is partitioned into blocks $\mathbf{K}_1$ and $\mathbf{K}_2$,

carrying units Nm and Nms^{-1}, respectively:

$$\mathbf{K} = \begin{bmatrix} \mathbf{K}_1 & \mathbf{K}_2 \end{bmatrix} \tag{5.47}$$

The Frobenius norms of $\mathbf{K}_1$ and $\mathbf{K}_2$ are shown in Fig. 5.17, which indicates that $\mathbf{K}$ undergoes "small" variations along the Adept cycle. These results help explain the reason why the choice of a specific operation point does not have a significant influence on the tracking performance. No matter which operation point we choose, the controller gain matrix $\mathbf{K}$ changes a very small amount over time. In fact, for all intents and purposes, $\mathbf{K}$ is constant over time. Furthermore, matrix $\mathbf{K}$ is obtained as the solution of the algebraic Riccati equation that is related with matrices $\mathbf{Q}$, $\mathbf{R}$, $\mathbf{A}$, and $\mathbf{B}$, as per eq. (5.21). In our case, the weighting matrices $\mathbf{Q}$ and $\mathbf{R}$ are constant. Therefore, we focus on the variation of the matrices $\mathbf{A}$ and $\mathbf{B}$ in order to find the reason why matrix $\mathbf{K}$ is constant over time. The matrices $\mathbf{A}$ and $\mathbf{B}$ are dimensionally inhomogeneous. They are partitioned into blocks carrying the same units, as shown below:

$$\mathbf{A} = \begin{bmatrix} \mathbf{O} & \mathbf{1} \\ \mathbf{A}_1 & \mathbf{A}_2 \end{bmatrix}, \quad \mathbf{B} = \begin{bmatrix} \mathbf{0} \\ \mathbf{B}_1 \end{bmatrix} \tag{5.48}$$

where $\mathbf{A}_1$, $\mathbf{A}_2$, and $\mathbf{B}_1$ carry the units s^{-2}, s^{-1}, and $\mathrm{N}^{-1}\mathrm{m}^{-1}\mathrm{s}^{-2}$, respectively. The Frobenius norms of the various blocks are shown in Figs. 5.18 and 5.19. Given that the Forbenius norms of $\mathbf{A}_1$, $\mathbf{A}_2$, and $\mathbf{B}$ do not vary significantly over time, it is logical that $\mathbf{K}$ will not vary significantly over time, which is exactly what is seen in Fig. 5.17. This is the reason why the PMC can be controlled by a constant-gain controller.

In conclusion, two gain-scheduling control schemes and two linear control schemes are designed in this chapter. The linear controllers are the constant-gain LQR combined with the constant-gain EKF control scheme and the feed-forward PD controller, based on the sliding-mode scheme. It is found that the associated nonlinear system can be controlled by a linear controller. The effectiveness of the proposed control schemes was shown on the PMC when undergoing a high-speed Adept test cycle, higher than three times the record, while also tracking a more demanding sine-wave trajectory. Moreover, the constant-gain controller with no feed-forward signal was tested, which showed that the effectiveness of the constant-gain controller does not rely on the feed-forward signal. Simulations show that the performance of the linear control schemes is promising. Compared with their nonlinear

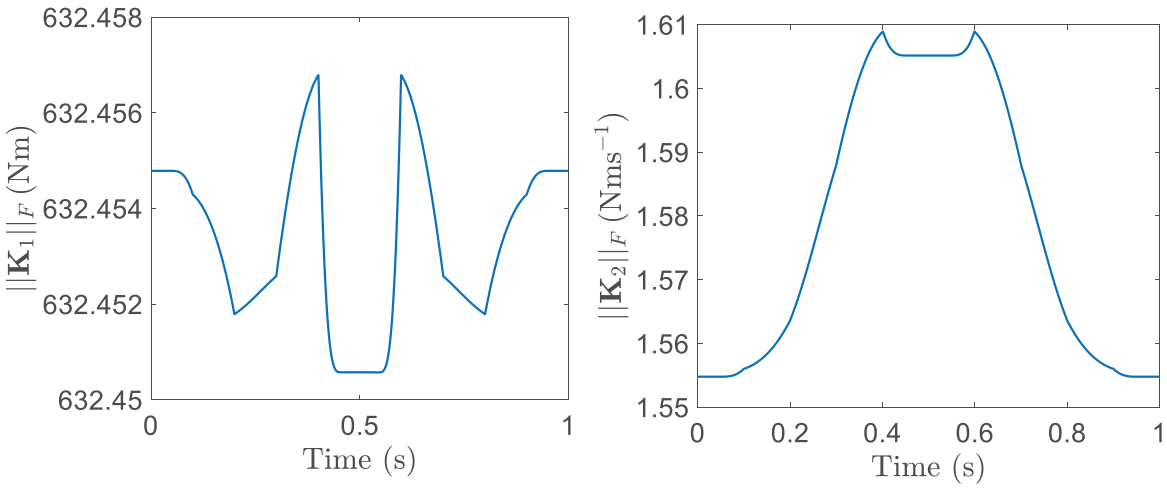

(a) (b)

Fig. 5.17: The Frobenius norms of (a) $\mathbf{K}_1$ and (b) $\mathbf{K}_2$ along the 1 cycle/s Adept trajectory

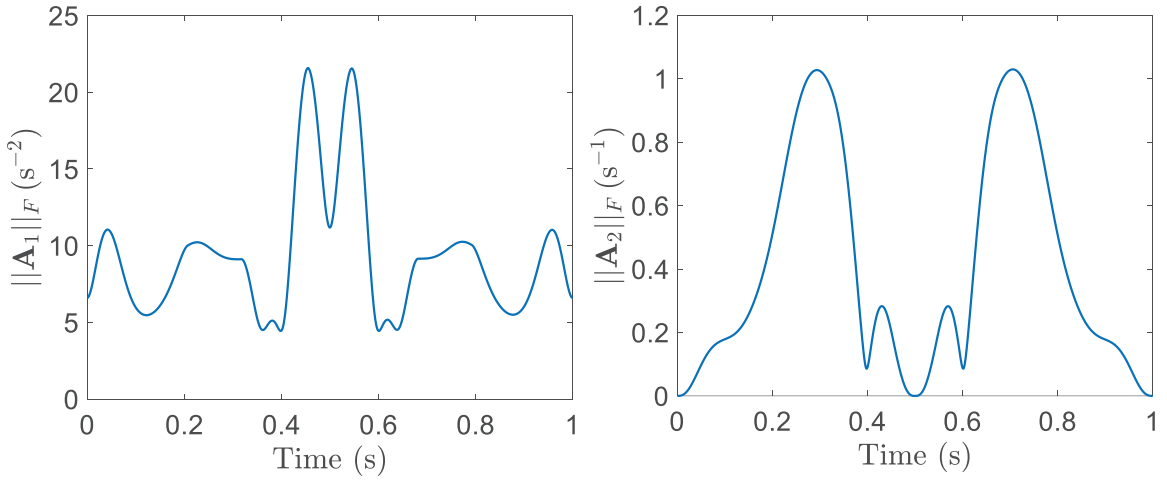

(a) (b)

Fig. 5.18: The Frobenius norms of (a) $\mathbf{A}_1$ and (b) $\mathbf{A}_2$ along the 1 cycle/s Adept trajectory

counterparts, linear controllers have a lower computational complexity. Therefore, they have better real-time performance in practice.

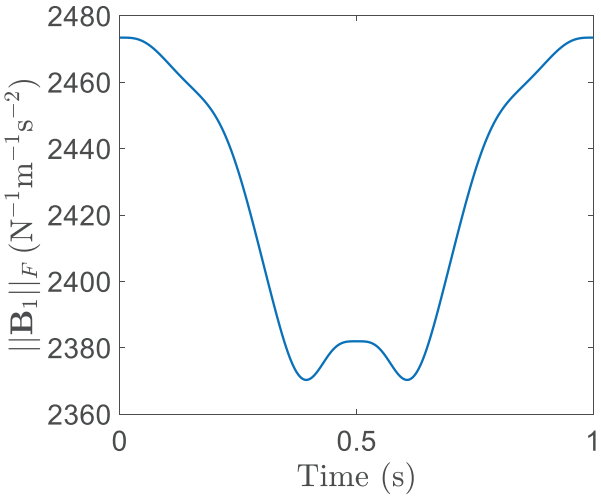

Fig. 5.19: The Frobenius norm of $\mathbf{B}_1$ along the 1 cycle/s Adept trajectory

Chapter 6

Conclusions and Recommendations for Future Work

6.1 Conclusions

The main motivation of this work was to increase the speed of a fast pick-and-place robot. In order to avoid the resonance caused by the high speeds, an elastodynamics analysis was conducted to verify that the frequency spectrum of the robot lies above that of the desired trajectory. The industry standard Adept test cycle was used to complete the analysis. The model and the analysis proposed in this thesis showed that an operation frequency under 3 cycles per second is not problematic. For higher operation frequencies, the robot structure needs to be optimized to have a higher frequency spectrum.

Issues related to vibrations having been settled, control scheme design must also be taken into account to be able to increase the velocitity of the robot. A conservative dynamics model of the robot was derived to design the control schemes while a complex dynamics model is obtained to test the control schemes. It was shown via simulation that the designed gain-scheduling LQR control schemes can achieve good trajectory tracking, while fighting against deviations from the motors and the encoders. Furthermore, the proposed linear controllers, a constant-gain controller and a feed-forward PD controller based on the sliding mode scheme, are found to be effective to track the trajectory with a high operation frequency, three times faster than the record, and a nonlinear sine-wave trajectory. Therefore, linear control schemes are eligible to control the nonlinear system.

Compared with their nonlinear counterparts, linear control schemes have the same tracking performance but are less complex. In the end, the eligibility of a linear controller for this nonlinear system is discussed.

6.2 Future Work

Recommendations for future work are listed below:

- According to the elastodynamics analysis of the current PMC version, the first natural frequency is not high enough to be away from the excitation frequency spectrum for speeds higher than 3 cycles/second. Therefore, the structural optimum design of the links is necessary to make them stiffer for a given mass than the current version.
- In order to improve the accuracy of the dynamics model of the PMC, a more accurate elastodynamics model should be built by means of the finite element analysis and the Lagrange equations. The deformation of the links will have a significant influence on the positioning accuracy in high-speed operations.
- In our case, the control scheme is designed in the joint space. However, the posture of the gripper obtained by the forward-kinematics model is biased because of the modelling error and the link flexibility. Therefore, it is better to use computer vision to obtain the posture of the gripper and design the control scheme in Cartesian space.

References

[1] K. Hunt, "Structural kinematics of in-parallel-actuated robot-arms," *Journal of Mechanisms, Transmissions, and Automation in Design*, vol. 105, no. 4, pp. 705–712, 1983.

[2] J.-P. Merlet, *Parallel Robots*, vol. 74. Springer Science & Business Media, 2012.

[3] J. M. Hervé, "The Lie group of rigid body displacements, a fundamental tool for mechanism design," *Mechanism and Machine theory*, vol. 34, no. 5, pp. 719–730, 1999.

[4] A. Schönflies, *La géométrie du mouvement: exposé synthétique*. Gauthier-Villars et fils, 1893.

[5] O. Bottema and B. Roth, *Theoretical kinematics, Volume 24 of North-Holland Series in Applied Mathematics and Mechanics*. North-Holland Publishing Co., Amsterdam, 1979.

[6] A. K. H. Makino and Y. Yamazaki, "Research and commercialization of scara robot-the case of industry-university joint research and development," *International Journal of Automation Technology*, vol. 1, pp. 61–67, 2007.

[7] J.-F. Gauthier, J. Angeles, S. B. Nokleby, and A. Morozov, "The kinetostatic conditioning of two-limb Schönflies motion generators," *Journal of Mechanisms and Robotics*, vol. 1, no. 1, p. 011010, 2009.

[8] J. Angeles, "Design Challenges in the Development of Fast Pick-and-place Robots," in *Romansy 19–Robot Design, Dynamics and Control*, pp. 61–68, Springer, 2013.

[9] K. Wohlhart, "Der homogene paralleltrieb-mechanismus," *Mathematica Pannonica*, vol. 2, no. 2, pp. 59–76, 1991.

[10] J. Hervé and F. Sparacino, "Star, a new concept in robotics," in *Proc. 3rd International Workshop on Advances in Robot Kinematics*, pp. 176–183, September 7–9, Ferrara, 1992.

[11] K. Wohlhart, "Displacement analysis of the general spatial parallelogram manipulator," in *Proc. 3rd International Workshop on Advances in Robot Kinematics*, pp. 104–111, 1992.

[12] P. Dietmaier, "Inverse kinematics of manipulators with 3 revolute and 3 parallelogram joints," in *Proc. ASME 22nd. Biennial Mechanisms Conference*, vol. 45, pp. 35–40, 1992.

[13] F. Pierrot and O. Company, "H4: A new family of 4-dof parallel robots," in *Proceedings of the 1999 IEEE/ASME International Conference on Advanced Intelligent Mechatronics*, pp. 508–513, IEEE, 1999.

[14] F. Pierrot, T. Shibukawa, K. Morita, *et al.*, "Four-degree-of-freedom parallel robot," Feb. 11 2003. US Patent 6,516,681.

[15] G. Gogu, "Structural synthesis of fully-isotropic parallel robots with Schönflies-motions via theory of linear transformations and evolutionary morphology," *European Journal of Mechanics-A/Solids*, vol. 26, no. 2, pp. 242–269, 2007.

[16] J. M. Hervé, "Design of parallel manipulators via the displacement group," in *Proceedings of the Ninth World Congress on the Theory of Machines and Mechanisms*, vol. 3, pp. 2079–2082, 1995.

[17] F. Sparacino and J. Hervé, "Synthesis of parallel manipulators using Lie-groups Y-star and H-robot," in *1993 IEEE/Tsukuba International Workshop on Advanced Robotics, 1993. Proceedings.*, pp. 75–80, IEEE, 1993.

[18] J. M. Hervé, "New translational parallel manipulators with extensible parallelogram," in *Proceedings of the 11th World Congress in Mechanism and Machine Science*, vol. 4, pp. 1599–1603, 2004.

[19] J. Angeles, "The qualitative synthesis of parallel manipulators," *Transctions-American Society of Mechanical Engineers Journal of Mechanical Design*, vol. 126, no. 4, pp. 617–624, 2004.

[20] Q. Li, Z. Huang, and J. M. Hervé, "Type synthesis of 3R2T 5-DOF parallel mechanisms using the Lie group of displacements," *IEEE Transactions on Robotics and Automation*, vol. 20, no. 2, pp. 173–180, 2004.

[21] A. Frisoli, D. Checcacci, F. Salsedo, and M. Bergamasco, "Synthesis by screw algebra of translating in-parallel actuated mechanisms," in *Advances in Robot Kinematics*, pp. 433–440, Springer, 2000.

[22] X. Kong and C. M. Gosselin, "Generation of parallel manipulators with three translational degrees of freedom based on screw theory," in *Proc. 2001 CCToMM Symposium on Mechanisms, Machines and Mechatronics, Saint-Hubert, Montreal*.

[23] K. Xianwen and C. M. Gosselin, "Type synthesis of 3T1R 4-DOF parallel manipulators based on screw theory," *IEEE Transactions on Robotics and Automation*, vol. 20, no. 2, pp. 181–190, 2004.

[24] X. Kong and C. M. Gosselin, "Type synthesis of 3-DOF translational parallel manipulators based on screw theory," *Journal of Mechanical Design*, vol. 126, no. 1, pp. 83–92, 2004.

[25] M. Carricato, "Fully isotropic four-degrees-of-freedom parallel mechanisms for Schönflies motion," *The International Journal of Robotics Research*, vol. 24, no. 5, pp. 397–414, 2005.

[26] G. Gogu, "Fully-isotropic T3R1-type parallel manipulators," in *On Advances in Robot Kinematics*, pp. 265–272, Springer, 2004.

[27] G. Gogu, "Singularity-free fully-isotropic parallel manipulators with Schönflies motions," in *12th International Conference on Advanced Robotics, 2005. ICAR'05. Proceedings*, pp. 194–201, IEEE, 2005.

[28] S. M. Kim, K. Shin, B.-J. Yi, and W. Kim, "Development of a novel two-limbed parallel mechanism having Schönflies motion," *Proceedings of the Institution of Mechanical Engineers, Part C: Journal of Mechanical Engineering Science*, vol. 229, no. 1, pp. 136–154, 2015.

[29] F. Pierrot, C. Reynaud, and A. Fournier, "DELTA: a simple and efficient parallel robot," *Robotica*, vol. 8, no. 02, pp. 105–109, 1990.

[30] R. Clavel, "Device for the movement and positioning of an element in space," Dec. 11 1990. US Patent 4,976,582.

[31] P. Vischer and R. Clavel, "Kinematic calibration of the parallel Delta robot," *Robotica*, vol. 16, no. 02, pp. 207–218, 1998.

[32] D. Carp-Ciocardia *et al.*, "Dynamic analysis of Clavel's Delta parallel robot," in *IEEE International Conference on Robotics and Automation, 2003. Proceedings. ICRA'03.*, vol. 3, pp. 4116–4121, IEEE, 2003.

[33] S. Krut, F. Pierrot, *et al.*, "Modelling of a 4-axis parallel machine for heavy parts handling," in *Parallel Kinematics Seminar*, no. 16, pp. 151–168, Verlag Scripten, 2002.

[34] S. Krut, V. Nabat, O. Company, and F. Pierrot, "A high-speed parallel robot for Scara motions," in *2004 IEEE International Conference on Robotics and Automation, 2004. Proceedings. ICRA'04.*, vol. 4, pp. 4109–4115, IEEE, 2004.

[35] S. Krut, O. Company, V. Nabat, and F. Pierrot, "Heli4: a parallel robot for SCARA motions with a very compact traveling plate and a symmetrical design," in *2006 IEEE/RSJ International Conference on Intelligent Robots and Systems*, pp. 1656–1661, IEEE, 2006.

[36] V. Nabat, M. Rodriguez, O. Company, S. Krut, and F. Pierrot, "Par4: Very high speed parallel robot for pick-and-place," in *2005 IEEE/RSJ International Conference on Intelligent Robots and Systems*, pp. 553–558, 2005.

[37] F. Pierrot, V. Nabat, S. Krut, *et al.*, "From Par4 to Adept Quattro," in *Robotic Systems for Handling and Assembly-3rd International Colloquium of the Collaborative Research Center SFB 562*, pp. 207–220, Shaker Verlag, 2008.

[38] F. Pierrot, V. Nabat, O. Company, S. Krut, and P. Poignet, "Optimal design of a 4-DOF parallel manipulator: From academia to industry," *IEEE Transactions on Robotics*, vol. 25, no. 2, pp. 213–224, 2009.

[39] C. Gosselin, M. Isaksson, K. Marlow, and T. Laliberté, "Workspace and sensitivity analysis of a novel nonredundant parallel SCARA robot featuring infinite tool rotation," *IEEE Robotics and Automation Letters*, vol. 1, no. 2, pp. 776–783, 2016.

[40] J. Angeles, A. Morozov, and O. Navarro, "A novel manipulator architecture for the production of SCARA motions," in *IEEE International Conference on Robotics and Automation, 2000. Proceedings. ICRA'00.*, vol. 3, pp. 2370–2375, IEEE, 2000.

[41] A. Morozov and J. Angeles, "The mechanical design of a novel Schönflies-motion generator," *Robotics and Computer-Integrated Manufacturing*, vol. 23, no. 1, pp. 82–93, 2007.

[42] J. Angeles, S. Caro, W. Khan, and A. Morozov, "Kinetostatic design of an innovative Schönflies-motion generator," *Proceedings of the Institution of Mechanical Engineers, Part C: Journal of Mechanical Engineering Science*, vol. 220, no. 7, pp. 935–943, 2006.

[43] J. Angeles and A. Morozov, "Four-degree-of-freedom parallel manipulator for producing Schönflies motions," Oct. 31 2006. US Patent 7,127,962.

[44] J. K. Salisbury and J. J. Craig, "Articulated hands: Force control and kinematic issues," *The International Journal of Robotics Research*, vol. 1, no. 1, pp. 4–17, 1982.

[45] A. Cammarata, J. Angeles, and R. Sinatra, "The dynamics of parallel Schönflies motion generators: the case of a two-limb system," *Proceedings of the Institution of Mechanical Engineers, Part I: Journal of Systems and Control Engineering*, vol. 223, no. 1, pp. 29–52, 2009.

[46] D. Alizadeh, J. Angeles, and S. Nokleby, "On the computation of the home posture of the McGill Schönflies-motion generator," in *Computational Kinematics*, pp. 149–158, Springer, 2009.

[47] A. Cammarata, J. Angeles, and R. Sinatra, "Kinetostatic and inertial conditioning of the McGill Schönflies-motion generator," *Advances in Mechanical Engineering*, Article no. 186203, 2010.

[48] P.-C. Lee and J.-J. Lee, "On the kinematics of a new parallel mechanism with Schönflies motion," *Robotica*, vol. 34, no. 09, pp. 2056–2070, 2016.

[49] K. Al-Widyan and J. Angeles, "The robust design of Schönflies-motion generators," in *On Advances in Robot Kinematics*, pp. 339–350, Springer, 2004.

[50] P.-C. Lee and J.-J. Lee, "Singularity and workspace analysis of three isoconstrained parallel manipulators with Schönflies motion," *Frontiers of Mechanical Engineering*, vol. 7, no. 2, pp. 163–187, 2012.

[51] P.-C. Lee, J.-J. Lee, and C.-C. Lee, "Four novel pick-and-place isoconstrained manipulators and their inverse kinematics," in *ASME 2010 International Design Engineering Technical Conferences and Computers and Information in Engineering Conference*, pp. 1079–1088, American Society of Mechanical Engineers, 2010.

[52] T. Harada and J. Angeles, "Kinematics and singularity analysis of a CRRHHRRC parallel Schönflies motion generator," *CSME Trans*, vol. 38, no. 2, pp. 173–183, 2014.

[53] T. Harada, T. Friedlaender, and J. Angeles, "The development of an innovative two-DOF cylindrical drive: Design, analysis and preliminary tests," in *2014 IEEE International Conference on Robotics and Automation (ICRA)*, pp. 6338–6344, 2014.

[54] P. K. Eskandary and J. Angeles, "The translating π-joint: design and applications," *Mechanism and Machine Theory*, vol. 122, pp. 361–370, 2018.

[55] P. K. Eskandary and J. Angeles, "The virtual screw: Concept, design and applications," *Mechanism and Machine Theory*, vol. 128, pp. 349–358, 2018.

[56] J.-F. Gauthier, J. Angeles, and S. Nokleby, "Optimization of a test trajectory for SCARA systems," in *Advances in Robot Kinematics: Analysis and Design*, pp. 225–234, Springer, 2008.

[57] V. Nabat, *Robots parallèles à nacelle articulée, du concept à la solution industrielle pour le pick-and-place*. PhD thesis, Université Montpellier II-Sciences et Techniques du Languedoc, 2007.

[58] F. Paccot, N. Andreff, and P. Martinet, "A review on the dynamic control of parallel kinematic machines: Theory and experiments," *The International Journal of Robotics Research*, vol. 28, no. 3, pp. 395–416, 2009.

[59] W. Khalil and E. Dombre, *Modeling, identification and control of robots*. Butterworth-Heinemann, 2004.

[60] P. R. Ouyang, W.-J. Zhang, and F.-X. Wu, "Nonlinear PD control for trajectory tracking with consideration of the design for control methodology," in *IEEE International Conference on Robotics and Automation, 2002. Proceedings. ICRA'02.*, vol. 4, pp. 4126–4131, IEEE, 2002.

[61] C. Brecher, T. Ostermann, and D. Friedrich, "Control concept for PKM considering the mechanical coupling between actors," *International Journal of Machine Tools and Manufacture*, vol. 48, no. 3, pp. 427–436, 2008.

[62] G. Barrette and C. M. Gosselin, "Determination of the dynamic workspace of cable-driven planar parallel mechanisms," *Transactions of the ASME-R-Journal of Mechanical Design*, vol. 127, no. 2, pp. 242–248, 2005.

[63] H. Abdellatif and B. Heimann, "Adapted time-optimal trajectory planning for parallel manipulators with full dynamic modelling," in *2005 IEEE International Conference on Robotics and Automation, 2005. ICRA 2005. Proceedings.*, pp. 411–416, IEEE, 2005.

[64] K.-T. Oen and L.-C. T. Wang, "Optimal dynamic trajectory planning for linearly actuated platform type parallel manipulators having task space redundant degree of freedom," *Mechanism and Machine Theory*, vol. 42, no. 6, pp. 727–750, 2007.

[65] K. Erkorkmaz and Y. Altintas, "High speed CNC system design. part I: jerk limited trajectory generation and quintic spline interpolation," *International Journal of Machine Tools and Manufacture*, vol. 41, no. 9, pp. 1323–1345, 2001.

[66] R. V. Fleisig and A. D. Spence, "A constant feed and reduced angular acceleration interpolation algorithm for multi-axis machining," *Computer-Aided Design*, vol. 33, no. 1, pp. 1–15, 2001.

[67] P. Lambrechts, M. Boerlage, and M. Steinbuch, "Trajectory planning and feedforward design for electromechanical motion systems," *Control Engineering Practice*, vol. 13, no. 2, pp. 145–157, 2005.

[68] Y. Zhiyong and H. Tian, "A new method for tuning PID parameters of a 3-DOF reconfigurable parallel kinematic machine," in *2004 IEEE International Conference on Robotics and Automation, 2004. Proceedings. ICRA'04.*, vol. 3, pp. 2249–2254, IEEE, 2004.

[69] J. Wu, J. Wang, and Z. You, "An overview of dynamic parameter identification of robots," *Robotics and Computer-integrated Manufacturing*, vol. 26, no. 5, pp. 414–419, 2010.

[70] S. Kock and W. Schumacher, "A mixed elastic and rigid-body dynamic model of an actuation redundant parallel robot with high-reduction gears," in *IEEE International Conference on Robotics and Automation, 2000. Proceedings. ICRA'00.*, vol. 2, pp. 1918–1923, IEEE, 2000.

[71] S. Kock and W. Schumacher, "Control of a fast parallel robot with a redundant chain and gearboxes: experimental results," in *IEEE International Conference on Robotics and Automation, 2000. Proceedings. ICRA'00.*, vol. 2, pp. 1924–1929, IEEE, 2000.

[72] F. Marquet, S. Krut, O. Company, and F. Pierrot, "Archi: a new redundant parallel mechanism-modeling, control and first results," in *2001 IEEE/RSJ International Conference on Intelligent Robots and Systems, 2001. Proceedings.*, vol. 1, pp. 183–188, IEEE, 2001.

[73] F. Caccavale, B. Siciliano, and L. Villani, "The tricept robot: dynamics and impedance control," *IEEE/ASME Transactions on Mechatronics*, vol. 8, no. 2, pp. 263–268, 2003.

[74] M. Callegari, M.-C. Palpacelli, and M. Principi, "Dynamics modelling and control of the 3-RCC translational platform," *Mechatronics*, vol. 16, no. 10, pp. 589–605, 2006.

[75] A. Vivas and P. Poignet, "Predictive functional control of a parallel robot," *Control Engineering Practice*, vol. 13, no. 7, pp. 863–874, 2005.

[76] B. Dasgupta and P. Choudhury, "A general strategy based on the Newton–Euler approach for the dynamic formulation of parallel manipulators," *Mechanism and Machine Theory*, vol. 34, no. 6, pp. 801–824, 1999.

[77] S.-H. Lee, J.-B. Song, W.-C. Choi, and D. Hong, "Position control of a Stewart platform using inverse dynamics control with approximate dynamics," *Mechatronics*, vol. 13, no. 6, pp. 605–619, 2003.

[78] J.-P. Merlet, *Parallel robots*, vol. 128. Springer Science & Business Media, 2006.

[79] J.-P. Merlet, "Solving the forward kinematics of a Gough-type parallel manipulator with interval analysis," *The International Journal of Robotics Research*, vol. 23, no. 3, pp. 221–235, 2004.

[80] L. Baron and J. Angeles, "The direct kinematics of parallel manipulators under joint-sensor redundancy," *IEEE Transactions on Robotics and Automation*, vol. 16, no. 1, pp. 12–19, 2000.

[81] F. Marquet, O. Company, S. Krut, and F. Pierrot, "Enhancing parallel robots accuracy with redundant sensors," in *IEEE International Conference on Robotics and Automation, 2002. Proceedings. ICRA'02.*, vol. 4, pp. 4114–4119, IEEE, 2002.

[82] W. S. Newman, C. E. Birkhimer, R. J. Horning, and A. T. Wilkey, "Calibration of a Motoman P8 robot based on laser tracking," in *IEEE International Conference on Robotics and Automation, 2000. Proceedings. ICRA'00.*, vol. 4, pp. 3597–3602, IEEE, 2000.

[83] H. Kino, S. Yabe, C. C. Cheah, S. Kawamura, and S. Arimoto, "A motion control scheme in task oriented coordinates and its robustness for parallel wire driven systems," *Journal of the Robotics Society of Japan*, vol. 18, no. 3, pp. 411–418, 2000.

[84] T. Dallej, N. Andreff, Y. Mezouar, and P. Martinet, "3D pose visual servoing relieves parallel robot control from joint sensing," in *2006 IEEE/RSJ International Conference on Intelligent Robots and Systems*, pp. 4291–4296, IEEE, 2006.

[85] R. Ginhoux, J. Gangloff, M. De Mathelin, L. Soler, M. M. A. Sanchez, and J. Marescaux, "Beating heart tracking in robotic surgery using 500 Hz visual servoing, model predictive control and an adaptive observer," in *2004 IEEE International Conference on Robotics and Automation, 2004. Proceedings. ICRA'04.*, vol. 1, pp. 274–279, IEEE, 2004.

[86] W. Shang and S. Cong, "Nonlinear computed torque control for a high-speed planar parallel manipulator," *Mechatronics*, vol. 19, no. 6, pp. 987–992, 2009.

[87] Q. Xu, Y. Li, and N. Xi, "Design, fabrication, and visual servo control of an XY parallel micromanipulator with piezo-actuation," *IEEE Transactions on Automation Science and Engineering*, vol. 6, no. 4, pp. 710–719, 2009.

[88] C. Yang, Q. Huang, H. Jiang, O. O. Peter, and J. Han, "PD control with gravity compensation for hydraulic 6-DOF parallel manipulator," *Mechanism and Machine Theory*, vol. 45, no. 4, pp. 666–677, 2010.

[89] A. Müller and T. Hufnagel, "Model-based control of redundantly actuated parallel manipulators in redundant coordinates," *Robotics and Autonomous Systems*, vol. 60, no. 4, pp. 563–571, 2012.

[90] P.-L. Yen and C.-C. Lai, "Dynamic modeling and control of a 3-DOF Cartesian parallel manipulator," *Mechatronics*, vol. 19, no. 3, pp. 390–398, 2009.

[91] H. Abdellatif and B. Heimann, "Advanced model-based control of a 6-DOF hexapod robot: A case study," *IEEE/ASME Transactions On Mechatronics*, vol. 15, no. 2, pp. 269–279, 2010.

[92] I. Davliakos and E. Papadopoulos, "Model-based control of a 6-DOF electrohydraulic Stewart–Gough platform," *Mechanism and Machine Theory*, vol. 43, no. 11, pp. 1385–1400, 2008.

[93] O. Linda and M. Manic, "Uncertainty-robust design of interval type-2 fuzzy logic controller for Delta parallel robot," *IEEE Transactions on Industrial Informatics*, vol. 7, no. 4, pp. 661–670, 2011.

[94] L. Vermeiren, A. Dequidt, M. Afroun, and T.-M. Guerra, "Motion control of planar parallel robot using the fuzzy descriptor system approach," *ISA Transactions*, vol. 51, no. 5, pp. 596–608, 2012.

[95] B. Zi, B. Duan, J. Du, and H. Bao, "Dynamic modeling and active control of a cable-suspended parallel robot," *Mechatronics*, vol. 18, no. 1, pp. 1–12, 2008.

[96] Y. Pi and X. Wang, "Observer-based cascade control of a 6-DOF parallel hydraulic manipulator in joint space coordinate," *Mechatronics*, vol. 20, no. 6, pp. 648–655, 2010.

[97] J. Wu, J. Wang, L. Wang, and T. Li, "Dynamics and control of a planar 3-DOF parallel manipulator with actuation redundancy," *Mechanism and Machine Theory*, vol. 44, no. 4, pp. 835–849, 2009.

[98] L. Wang, J. Wu, J. Wang, and Z. You, "An experimental study of a redundantly actuated parallel manipulator for a 5-DOF hybrid machine tool," *IEEE/ASME Transactions on Mechatronics*, vol. 14, no. 1, pp. 72–81, 2009.

[99] P. M. Aubin, M. S. Cowley, and W. R. Ledoux, "Gait simulation via a 6-dof parallel robot with iterative learning control," *IEEE Transactions on Biomedical Engineering*, vol. 55, no. 3, pp. 1237–1240, 2008.

[100] C. Yang, Q. Huang, and J. Han, "Decoupling control for spatial six-degree-of-freedom electro-hydraulic parallel robot," *Robotics and Computer-Integrated Manufacturing*, vol. 28, no. 1, pp. 14–23, 2012.

[101] Y. Pi and X. Wang, "Trajectory tracking control of a 6-DOF hydraulic parallel robot manipulator with uncertain load disturbances," *Control Engineering Practice*, vol. 19, no. 2, pp. 185–193, 2011.

[102] X. Zhang, J. K. Mills, and W. L. Cleghorn, "Experimental implementation on vibration mode control of a moving 3-PRR flexible parallel manipulator with multiple PZT transducers," *Journal of Vibration and Control*, vol. 16, no. 13, pp. 2035–2054, 2010.

[103] E. Özgür, N. Bouton, N. Andreff, and P. Martinet, "Dynamic control of the Quattro robot by the leg edges," in *2011 IEEE International Conference on Robotics and Automation (ICRA)*, pp. 2731–2736, IEEE, 2011.

[104] V. Rosenzveig, S. Briot, and P. Martinet, "Minimal representation for the control of the Adept Quattro with rigid platform via leg observation considering a hidden robot model," in *2013 IEEE/RSJ International Conference on Intelligent Robots and Systems (IROS)*, pp. 430–435, IEEE, 2013.

[105] E. Özgür, R. Dahmouche, N. Andreff, and P. Martinet, "A vision-based generic dynamic model of PKMs and its experimental validation on the Quattro parallel robot," in *2014 IEEE/ASME International Conference on Advanced Intelligent Mechatronics (AIM)*, pp. 937–942, IEEE, 2014.

[106] R. Kumar, P. Berkelman, P. Gupta, A. Barnes, P. S. Jensen, L. L. Whitcomb, and R. H. Taylor, "Preliminary experiments in cooperative human/robot force control for robot assisted microsurgical manipulation," in *IEEE International Conference on Robotics and Automation, 2000. Proceedings. ICRA'00.*, vol. 1, pp. 610–617, IEEE, 2000.

[107] M. Shaheed, H. Poerwanto, and M. Tokhi, "Adaptive inverse-dynamic and neuro-inverse-dynamic active vibration control of a single-link flexible manipulator," *Proceedings of the Institution of Mechanical Engineers, Part I: Journal of Systems and Control Engineering*, vol. 219, no. 6, pp. 431–448, 2005.

[108] M. A. Meggiolaro and S. Dubowsky, "Improving the positioning accuracy of powerful manipulators with application in nuclear maintenance," in *Proceedings of the 16th Brazilian Congress of Mechanical Engineering on Robotics and Control*, vol. 15, pp. 210–219, 2001.

[109] Q. Zhang, C. Li, J. Zhang, and J. Jin, "Active vibration control and coupled vibration analysis of a parallel manipulator with multiple flexible links," *Shock and Vibration*, Article ID: 7474085, 2016.

[110] M. Benosman and G. Le Vey, "Control of flexible manipulators: A survey," *Robotica*, vol. 22, no. 5, pp. 533–545, 2004.

[111] S. K. Dwivedy and P. Eberhard, "Dynamic analysis of flexible manipulators, a literature review," *Mechanism and Machine Theory*, vol. 41, no. 7, pp. 749–777, 2006.

[112] C. T. Kiang, A. Spowage, and C. K. Yoong, "Review of control and sensor system of flexible manipulator," *Journal of Intelligent & Robotic Systems*, vol. 77, no. 1, pp. 187–213, 2015.

[113] H. Rahimi and M. Nazemizadeh, "Dynamic analysis and intelligent control techniques for flexible manipulators: a review," *Advanced Robotics*, vol. 28, no. 2, pp. 63–76, 2014.

[114] Q. Zhang, J. K. Mills, W. L. Cleghorn, J. Jin, and Z. Sun, "Dynamic model and input shaping control of a flexible link parallel manipulator considering the exact boundary conditions," *Robotica*, vol. 33, no. 06, pp. 1201–1230, 2015.

[115] Q. Zhang, L. Zhou, J. Zhang, and J. Jin, "Efficient modal control for vibration suppression of a flexible parallel manipulator," in *2013 IEEE International Conference on Robotics and Biomimetics (ROBIO)*, pp. 13–18, IEEE, 2013.

[116] X. Zhang, J. K. Mills, and W. L. Cleghorn, "Active vibration control of a 3-PRR flexible parallel manipulator with PZT actuators and sensors," in *ASME 2008 International Design Engineering Technical Conferences and Computers and Information in Engineering Conference*, pp. 1095–1100, American Society of Mechanical Engineers, 2008.

[117] X. Zhang, X. Wang, J. K. Mills, and W. L. Cleghorn, "Dynamic modeling and active vibration control of a 3-PRR flexible parallel manipulator with PZT transducers," in *7th World Congress on Intelligent Control and Automation*, pp. 461–466, IEEE, 2008.

[118] X. Zhang, J. K. Mills, and W. L. Cleghorn, "Flexible linkage structural vibration control on a 3-PRR planar parallel manipulator: experimental results," *Proceedings of the Institution of Mechanical Engineers, Part I: Journal of Systems and Control Engineering*, vol. 223, no. 1, pp. 71–84, 2009.

[119] X. Zhang, J. K. Mills., and W. L. Cleghorn, "Vibration control of elastodynamic response of a 3-PRR flexible parallel manipulator using PZT transducers," *Robotica*, vol. 26, no. 05, pp. 655–665, 2008.

[120] X. Zhang, J. K. Mills, and W. L. Cleghorn, "Structural vibration control of a moving 3-PRR flexible parallel manipulator with multiple PZT actuators and sensors," in *ASME 2007 International Design Engineering Technical Conferences and Computers and Information in Engineering Conference*, pp. 265–271, American Society of Mechanical Engineers, 2007.

[121] Z. Chu and J. Cui, "Experiment on vibration control of a two-link flexible manipulator using an input shaper and adaptive positive position feedback," *Advances in Mechanical Engineering*, vol. 7, no. 10, pp. 1–13, 2015.

[122] K. Kozak, I. Ebert-Uphoff, and W. Singhose, "Locally linearized dynamic analysis of parallel manipulators and application of input shaping to reduce vibrations," *Transctions-American society of Mechanical Engineers Journal of Mechanical Design*, vol. 126, no. 1, pp. 156–168, 2004.

[123] M. Burkhardt, R. Seifried, and P. Eberhard, "Experimental studies of control concepts for a parallel manipulator with flexible links," *Journal of Mechanical Science and Technology*, vol. 29, no. 7, pp. 2685–2691, 2015.

[124] M. B. Morlock, M. Burkhardt, and R. Seifried, "Friction compensation, gain scheduling and curvature control for a flexible parallel kinematics robot," in *2015 IEEE/RSJ International Conference on Intelligent Robots and Systems (IROS)*, pp. 2354–2359, IEEE, 2015.

[125] J. Angeles, *Fundamentals of Robotic Mechanical Systems: Theory, Methods, and Algorithms*. Fourth Edition, Springer, New York, 2014.

[126] W. V. D. Hodge and D. Pedoe, *Methods of Algebraic Geometry*. Cambridge University Press, Cambridge, 1994.

[127] J. Lončarić, "Normal forms of stiffness and compliance matrices," *IEEE Journal on Robotics and Automation*, vol. 3, no. 6, pp. 567–572, 1987.

[128] A. Taghvaeipour, J. Angeles, and L. Lessard, "On the elastostatic analysis of mechanical systems," *Mechanism and Machine Theory*, vol. 58, pp. 202–216, 2012.

[129] T. Zou and J. Angeles, "The decoupling of the Cartesian stiffness matrix in the design of microaccelerometers," *Multibody System Dynamics*, vol. 34, no. 1, pp. 1–21, 2015.

[130] J. Kövecses and S. Ebrahimi, "Parameter analysis and normalization for the dynamics and design of multibody systems," *Journal of Computational and Nonlinear Dynamics*, vol. 4, no. 3, pp. 031008–1—031008–10, 2009.

[131] R. von Mises, "Motorrechnung, ein neues Hilfsmittel der Mechanik," *ZAMM-Journal of Applied Mathematics and Mechanics/Zeitschrift für Angewandte Mathematik und Mechanik*, vol. 4, no. 2, pp. 155–181, 1924.

[132] A. Taghvaeipour, J. Angeles, and L. Lessard, "Elastodynamics of a two-limb Schönflies motion generator," *Proceedings of the Institution of Mechanical Engineers, Part C: Journal of Mechanical Engineering Science*, vol. 229, no. 4, pp. 751–764, 2015.

[133] P. K. Eskandary and J. Angeles, "The dynamics of a parallel Schönflies-motion generator," *Mechanism and Machine Theory*, vol. 119, pp. 119–129, 2018.

[134] P. K. Eskandary, B. Belzile, and J. Angeles, "Trajectory-planning and normalized-variable control for parallel pick-and-place robots," *ASME Journal of Mechanisms and Robotics*, in press.

[135] J. Angeles, *Fundamentals of Robotic Mechanical Systems: theory, methods, and algorithms*, vol. 124. Springer Science & Business Media, 2013.

[136] E. Hendricks, O. Jannerup, and P. H. Sørensen, *Linear systems control: deterministic and stochastic methods*. Springer, Berlin, 2008.

[137] J. L. Crassidis and J. L. Junkins, *Optimal estimation of dynamic systems*. Chapman and Hall/CRC, Boca Raton, 2011.

[138] S. Takacs and C. J. Damaren, "Control strategies for stable orbits around phobos," in *Proceedings of 2005 IEEE Conference on Control Applications, 2005. Proceedings.*, pp. 553–558, IEEE, 2005.

[139] M. W. Spong, S. Hutchinson, and M. Vidyasagar, *Robot Modeling and Control*. John Wiley and Sons, Inc., New York, 2006.

[140] J.-J. E. Slotine and W. Li, "On the adaptive control of robot manipulators," *The International Journal of Robotics Research*, vol. 6, no. 3, pp. 49–59, 1987.